# MODIFICATION OF ALUMINIUM-SILICON ALLOYS BY RARE-EARTH ADDITIONS

by

**Mario De Giovanni**

A thesis submitted in partial fulfilment of the requirements for the degree of
Doctor of Philosophy in Engineering

University of Warwick, Warwick Manufacturing Group, WMG
November 2018

# Table of Contents

# List of Figures

# List of Tables

# Acknowledgments

First and foremost I would like to thank my supervisor Dr. Prakash Srirangam for all his help, guidance and support throughout the last four years. Furthermore, I would also like to thank my co-supervisors Prof. Barbara Shollock and Prof. Sridhar Seetharaman.

I would like to acknowledge the financial support provided by Prof. Richard Dashwood through Catapult HVM, which allowed me to purchase the materials used throughout this thesis.

In addition I would like to thank the following: the doctoral researchers and staff, former or present, of the Steels processing group at WMG, University of Warwick, who have all been very obliging and supportive throughout the years; Carl Slater, Geoff West, Sam Marks, Richard Keyte, Kateryna Hechu, Raul Chinchilla Adell and Hiren Kotadia; Dr. Jason Warnett and Prof. Mark Williams from the Metrology group at WMG, for allowing for and conducting the XCT analysis; the technicians in the workshop at WMG for their assistance with sample machining; Dr. Alam Talukder and Prof. Raj Banarjee from the University of North Texas for the APT experiment; and Dr. James Kaduk from Poly Crystallography, Inc. for the XRD analysis.

I would also like to thank my employer Bridgnorth Aluminium Ltd. for the support received through the write-up phase of my PhD especially Jeremy Brown, Glenn Smith and Filippos Patsiogiannis.

Furthermore, I would like to thank my family and my wife’s family for their continuous encouragement and support.

Last but certainly not least, I would like to thank my wife Sophie, for her assistance, encouragement, constant backing and advice throughout this project. These have been a great asset to me personally and to this work and are sincerely appreciated.

# Declarations

The work presented in this thesis is original and my own work, unless otherwise stated in the text. I confirm that this thesis has not been submitted for a degree at another university.

Experimental work acquiring x-ray diffraction patterns presented in chapters 2 and 3 was carried out by James A. Kaduk of Poly Crystallography, Inc.
Experimental work for the atom probe tomography presented in chapter 4 was carried out by Alam Talukder at the University of North Texas.
Experimental work for the x-ray computed tomography presented in chapters 5 and 6 was mostly carried out by Jason M. Warnett, from the Metrology group, WMG.

Chapter 2 was published as:
De Giovanni, M., Kaduk, J. A. & Srirangam, P. Modification of Al-Si Alloys by Ce or Ce with Sr. *JOM* 1–9 (2018). doi:10.1007/s11837-018-3192-6

Chapter 4 was published as:
De-Giovanni, M., Alam, T., Banerjee, R. & Srirangam, P. 3D Atom Probe Tomography Study on Segregation of Yttrium in Modified Al-Si Alloys. *JOM* **70,** 1765–1770 (2018). doi: 10.1007/s11837-018-2909-x

Chapter 5 was published as:
M. De Giovanni, J.M. Warnett, M.A. Williams, and P.Srirangam, 3D imaging and quantification of porosity and intermetallic particles in strontium modified Al-Si alloys, Journal of Alloys and Compounds 727 (2017) 353-361. doi: 10.1016/j.jallcom.2017.08.146.

# Abstract

Cast aluminium-silicon (Al-Si) alloys are used extensively in various industries due to their advantageous properties such as high strength-to-weight ratio, good corrosion resistance and high fluidity which allows for defect-free complex castings. Under normal casting conditions the microstructure is composed of silicon needles in an aluminium matrix. These provide propagation planes for defects and therefore deteriorate the mechanical properties. By adding certain elements, usually strontium (Sr), the Si needles change to fibres, however this is also known to increase porosity in castings. The mechanism that causes the change from needles to fibres has been extensively debated and a number of theories can be found in the literature, revolving around both the nucleation and growth stages of eutectic Si. In this thesis high purity materials were used to prepare hypoeutectic unmodified and Sr-modified Al-Si alloys to which cerium (Ce) or yttrium (Y) were added and differences between these alloys in the solidification progression and microstructure were investigated. The addition of 1% Ce or Y to unmodified Al-Si produced a partially modified eutectic Si, whilst full modification was retained when these were added to Sr-modified Al-Si. These additions also resulted in a significant decrease in the eutectic growth temperatures and in the formation of $Al_2Si_2Ce$ or $Al_2Si_2Y$ intermetallic phases. It is suggested that similar to the $Al_2Si_2Sr$ in Sr-modified Al-Si these intermetallic phases nucleate on aluminium phosphide (AlP) and thus do not allow for the nucleation of eutectic silicon on this phase. Three dimensional atom probe tomography (3D APT) of Y-partially-modified Al-Si showed a preferential segregation of yttrium within the eutectic Si. By means of optical microscopy and high resolution x-ray computed tomography (XCT), it was also demonstrated that the Sr modification significantly increases the porosity in cast Al-Si alloys which is reduced following the rare-earth additions.

# List of Abbreviations

| | |
|---|---|
| Al | Aluminium |
| AlP | Aluminium phosphide |
| APT | Atom probe tomography |
| Ce | Cerium |
| DSC | Differential scanning calorimetry |
| EBSD | Electron backscatter diffraction |
| EDS | Energy dispersive spectroscopy |
| EXAFS | Extended x-ray absorption fine structure spectroscopy |
| Eu | Europium |
| FCC | Face-centred cubic |
| Fe | Iron |
| ICP-OES | Inductively coupled plasma optical emission spectroscopy |
| IIT | Impurity induced twinning |
| Na | Sodium |
| ppm | Parts per million |
| Sb | Antimony |
| SEM | Scanning electron microscope |
| Si | Silicon |
| Sr | Strontium |
| TEM | Transmission electron microscope |
| TPRE | Twin plane re-entrant edge |
| XCT | X-ray computed tomography |
| XRD | X-ray diffraction |
| Y | Yttrium |

# Chapter 1:

# Introduction

## 1.1. Introduction

Aluminium alloys are widely used as light weight structural materials in automotive, aerospace and domestic casting applications. These alloys possess high strength to weight ratio and excellent mechanical and performance properties. These alloys also possess good corrosion resistance due to the formation of a surface oxide layer which prevents further corrosion of the alloy[1–5].

One of the most extensively employed aluminium alloy systems is aluminium-silicon, which is widely used in automotive and aerospace applications Aluminium-silicon alloys possess an intrinsic problem as the microstructure will form large flake-like silicon phases during solidification. These provide propagation planes for any defects within the alloy which deteriorate the mechanical properties of the alloy and could potentially result in catastrophic failure of any components. However, it was found that the addition of modifying elements in trace levels transform the morphology of eutectic silicon from plate-like to fibrous morphology resulting in a major improvement in the mechanical properties of such a system. Only few elements can cause this modification effect and since the 1970s strontium (Sr) has been the most widely used modification element in industry[1,4]. However, strontium also poses some problems such as increasing the porosity in the alloy castings. Since the discovery of the modification phenomenon in the 1920s, a large number of hypothesis were developed to try and explain the mechanism taking place in order to cause this modification. These have been reviewed in some depth in the literature review section of this thesis.

Rare-earth elements have also been researched, as potential modification elements. However, most of these have been shown to only refine the eutectic silicon phase. However, there is still no complete understanding of the mechanism taking place when refinement, following addition of these elements, takes place[6–12].

## 1.2. References

1. Bartley, R. *British and European Aluminium Casting Alloys*. (Association of Light Alloy Refiners, 1996).
2. Elliott, R. Aluminium-Silicon Alloys and Cast Irons: commercially important anomalous alloys. in *Eutectic Solidification Processing: Crystalline and Glassy Alloys* 157–231 (Butterworths, 1983).
3. Hatch, J. E. *Aluminium: Properties and Physical Metallurgy*. (American Society of Metals, 1984).
4. Polmear, I. J. Cast Aluminium Alloys. in *Light Alloys* 205–235 (Elsevier, 2005). doi:10.1016/B978-075066371-7/50008-6
5. Davis, J. R. *ASM Speciality Handbook: Aluminum and Aluminum Alloys*. (ASM International, 1993).
6. Vijeesh, V. & Prabhu, K. N. The Effect of Cooling Rate and Cerium Melt Treatment on Thermal Analysis Parameters and Microstructure of Hypoeutectic Al-Si Alloy. in *Light Metals 2015* 403–407 (John Wiley & Sons, Inc., 2015). doi:10.1002/9781119093435.ch67
7. Tsai, Y. C., Lee, S. L. & Lin, C. K. Effect of trace Ce addition on the microstructures and mechanical properties of A356 (Al–7SI–0.35 Mg) aluminum alloys. *J. Chinese Inst. Eng.* **34**, 609–616 (2011).
8. Nogita, K., Knuutinen, A., McDonald, S. D. & Dahle, A. K. Mechanisms of eutectic solidification in Al–Si alloys modified with Ba, Ca, Y and Yb. *J. Light Met.* **1**, 219–228 (2001).
9. Knuutinen, A., Nogita, K., McDonald, S. D. & Dahle, A. K. Porosity formation in aluminium alloy A356 modified with Ba, Ca, Y and Yb. *J. Light Met.* **1**, 241–249 (2001).
10. Nogita, K., McDonald, S. D. & Dahle, A. K. Eutectic Modification of Al-Si Alloys with Rare Earth Metals. *Mater. Trans.* **45**, 323–326 (2004).
11. Qiu, H., Yan, H. & Hu, Z. Effect of samarium (Sm) addition on the microstructures and mechanical properties of Al–7Si–0.7Mg alloys. *J. Alloys Compd.* **567**, 77–81 (2013).
12. Tsai, Y. C. *et al.* Effect of trace La addition on the microstructures and

mechanical properties of A356 (Al–7Si–0.35Mg) aluminum alloys. *J. Alloys Compd.* **487**, 157–162 (2009).

# Chapter 2:

# **Literature Review**

## 2.1. Properties and Applications of Aluminium-Silicon Alloys

Aluminium alloys are well-known for being light weight, their density being a third of that of steel, high strength, wear and corrosion resistant materials. They are also suitable for foundry applications and show high electrical and thermal conductivity. Aluminium alloys can be easily machined and welded[1–3].

Aluminium-Silicon (Al-Si) system is one of the most important alloy systems in automotive and casting industries. The large volume of Al-Si eutectic imparts high fluidity, low shrinkage, hot tear resistance and pressure tightness to the alloy, making these alloys especially important. Furthermore, the hard Si particles result in increased wear resistance of the alloy, although this decreases the machinability of the alloy. These properties make these alloys particularly ideal for casting, brazing and welding applications[1,3,4].

The Al-Si alloy system is a simple eutectic with a limited solid solubility at both ends. The eutectic occurs at 577 °C and 12.2% silicon[5]. At the eutectic temperature, the aluminium and silicon solid solution contain 1.65% Si and 0.5% Al, respectively. There are no other intermetallics in the binary system[3]. Figure 2.1 below presents the phase diagram and shows the microstructure at different compositions.

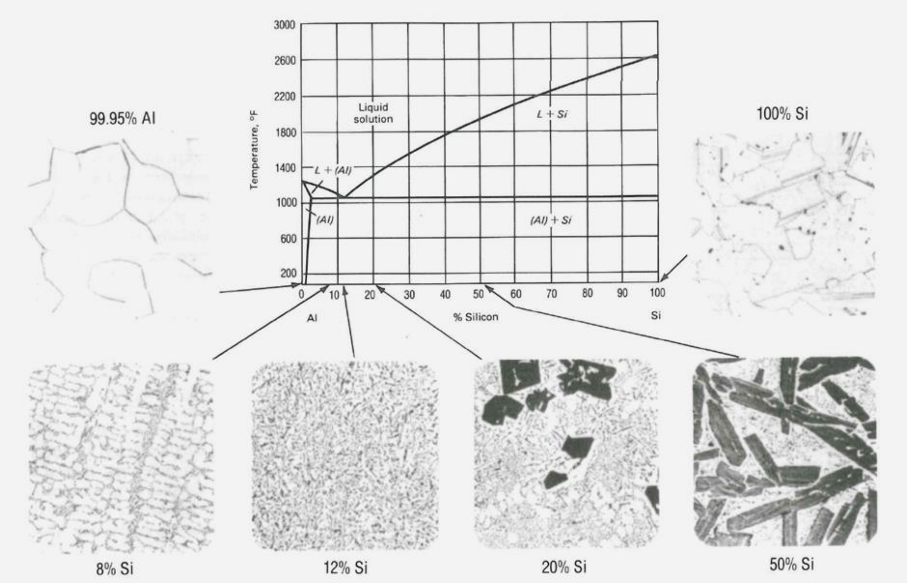

Figure 2.1: Aluminium-Silicon phase diagram showing the microstructure for different Si compositions[6].

Al-Si alloys are usually used in sand or permanent mould castings where strength is not a priority, however different casting processes are better suited for different Si contents. Typically, slow cooling rate processes, such as sand casting contain 5 to 7 % Si, permanent mould 7 to 9 % Si and die-casting 8 to 12 % Si[3,4,6].

### 2.1.1. Classification of Al-Si alloys

Other elements, such as copper and magnesium, are frequently added to Al-Si alloys in order to improve strength and machinability[3,4]. Table 2.1 presents a number of applications for various commonly used alloys whilst figure 2.2 shows a thin-walled automotive transmission casing constructed by employing an Al-Si alloy.

Table 2.1: Applications of various commercially available Al-Si alloys[6].

| **Alloy** | **Chemical Composition** | **Applications** |
|---|---|---|
| 413.0, A413.0 | 12Si | Miscellaneous thin-walled and complex design castings. |
| 443.0, A443.0, B443.0, C443.0 | 5.2Si | Cooking utensils, food handling equipment, marine fittings and various types of thin section castings |
| 356.0, A356.0 | 7Si, 0.3Mg | Aircraft structure, engine controls and pump parts, automotive transmission cases, water-cooled cylinder blocks. |
| 357.0, A357.0 | 7Si, 0.5 Mg | Critical aerospace applications. |
| 359.0 | 9Si, 0.6 Mg | Moderate strength applications with superior casting requirements. |
| 360.0, A360.0 | 9.5Si, 0.5Mg | Die castings requiring high corrosion resistance such as cover plates and instrument cases. |

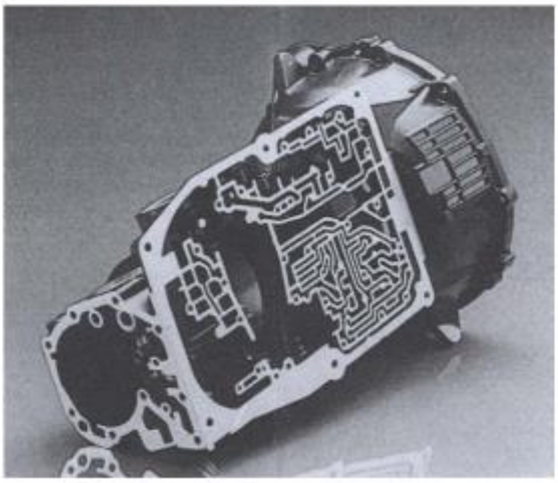

Figure 2.2: Thin-walled cast Al-Si alloy automotive transmission casing[4].

Binary Al-Si alloys show good ductility up to the eutectic composition, assuming that a low iron level is maintained. In this respect, manganese is normally added to the alloy as in its presence fine α-AlFeSi forms rather than large brittle flakes of β-AlFeSi[4]. A further issue with these alloys is their thermal stability as silicon will precipitate from solid solution upon heating. This issue is resolved by performing T5 or T7 tempers, in the temperature range of 200-500 °C on castings to be used at temperatures above 150 °C[4].

## 2.2. The Al-Si Modification

A slow solidification, such as that taking place in sand and permanent mould casts, produces a very coarse microstructure in which the eutectic is made up of large plates or needles of silicon in a continuous aluminium matrix. Alloys exhibiting this microstructure show low ductility due to the large and brittle silicon plates. Ductility, machinability and tensile strength can be improved by faster cooling such as permanent mould casting or by chemical modification. In the case of the latter, the Si phase will assume a fibrous form[1,4]. Figure 2.3 shows the microstructural change which takes place after modification.

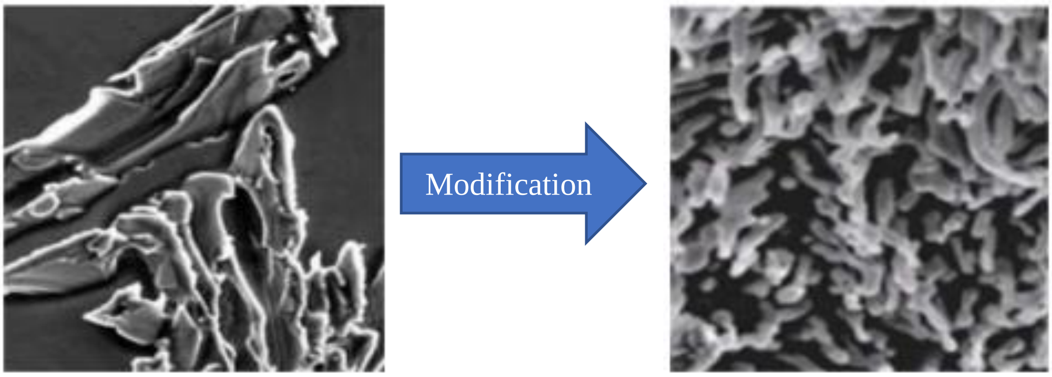

Figure 2.3: The change from plate-like to fibre-like morphology upon addition of modifier[7].

In 1921 Pacz[8] filed a patent (US 1387900 A) describing the modification of the Si morphology in Al-Si alloys by addition of certain alkali fluorides, mainly sodium fluoride, prior to pouring. The modification was achieved by addition of sodium salts or metallic sodium (0.005 - 0.015%) to the melt[4].

Section 2.4 presents the literature findings involving modification by the elements which are most widely used, sodium and strontium, and the elements which are being investigated in this research, cerium and yttrium. Information regarding further elements which have been explored in literature is also presented.

## 2.3. The modification mechanism theories

As previously mentioned the modification of Al-Si was discovered in 1921. Since then a number of theories regarding the mechanism taking place in this modification have been proposed. The theories are normally divided in two: those that focus around the nucleation and those relating to the growth of the Si phase.

### 2.3.1. Nucleation induced modification mechanisms

The initial theories, proposed in 1922, stated that the modification by addition of sodium fluoride (NaF) or potassium fluoride (KF) is due to the fluxing effect which removes oxides and impurities[9]. Later on it was noted that metallic sodium still performs the modification and therefore the removal of oxides was deemed to not be the cause[9]. It was then proposed that a ternary Al-Si-Na alloy forms. This hypothesised that the modified microstructure was the regular morphology of this ternary eutectic[9]. Later on cooling curves were analysed which showed a lower eutectic freezing temperature whilst the melting point remained the same, thus showing that a ternary alloy was not possible[10]. Eventually the dispersed colloidal phase theory was proposed. This states that the solidification takes place when the Al and Si go from a state of atomic dispersion to a crystalline form. The added Na, due to its low solid solubility in Al, deposits on the Si colloidal particles and hinders further crystallization[9]. Hume-Rothery dismissed this theory due to the implication that the formation of colloids means the presence of an electrical charge. The theory was further disproved by the observation that Na is preferentially located in the Al, though more recent studies have shown the presence of Al-Si-Na/Sr clusters within the silicon phase[9,11].

Rothery proposed that the atoms group together and form complexes which will act as nuclei. According to this theory these complexes are destroyed in the presence of modifiers[9]. More recently this phenomenon was confirmed by high temperature x-ray diffraction[12].

Al-Si system is a faceted-nonfaceted eutectic system with large eutectic interparticle spacing and considerable undercooling. With modification, undercooling increases and interparticle spacing decreases. This is contrary to that predicted by the eutectic theory. In an attempt to understand this difference Flood and Hunt[13] noted that, in the unmodified alloy, the eutectic forms on the primary aluminium dendrites ahead of the solidification front. On the other hand, in Na modified alloys, no nucleation took place ahead of the solidification front. Na therefore prevents nucleation on dendrites ahead of eutectic front, which changes the average growth velocity giving finer interparticle spacing. Furthermore, the undercooling is a result of the decreased nucleation. This research led to developing a relationship between the eutectic morphology to the undercooling and nucleation kinetics.

By means of thermal analysis Hanna et al.[14] showed that for modified hypoeutectic alloys 1-2 K supercooling[1] takes place, which is not the case for the unmodified alloys. They indicated that this is due to Na additions affecting the nucleation of Si in Al-Si alloys. Dahle et al.[15], investigated the phenomenon by electron backscatter diffraction (EBSD) and noted that the eutectic nucleation in unmodified alloys takes place on primary dendrites, whilst at low concentrations (100 ppm) of Sr addition, eutectic nucleation takes place in the interdendritic liquid. At higher concentration (500 ppm) nucleation reverts back to the primary dendrites.

More recently a number of researchers have again proposed mechanisms revolving around the eutectic nucleation. Bian et al.[12] performed high temperature x-ray diffraction (XRD) and showed how the presence of Sr reduces the Si-Si bonds thus destroying potential nucleation sites and increases the undercooling. By using the same method whilst in the presence of Sb[16], which is a known refiner, they showed how this element increases the Si-Si bonds, enhancing nucleation and producing a refined structure. Later on, Guthy and Makhlouf[17] showed that the wetting angle in Sr modified alloy is larger than for unmodified alloys indicating a change in the solid/liquid interface during solidification and thus possibly changing the Al-Si eutectic nucleation kinetics.

Srirangam et al. have used extended x-ray absorption fine structure spectroscopy (EXAFS) and atom probe tomography (APT) to map the local structure around Sr atoms in the master alloy and in a modified Al-Si alloy. The EXAFS showed that in the master alloy the Sr forms $Al_4Sr$ intermetallics, whereas in the modified alloy they are preferentially bonded to Si to form $Al_2Si_2Sr$ clusters. The authors hypothesize that Sr in Al-Si forms $Al_2Si_2Sr$ intermetallics which could potentially poison the nucleation site, thus delaying the eutectic nucleation and eventually cause the modification[18].

---

[1] Supercooling is the difference between nucleation temperature and eutectic growth temperature.

### 2.3.2. Growth induced modification mechanisms

Following the initial nucleation based theories the focus shifted to growth induced theories. Thall and Chalmers focused around the growth dynamics of Al and Si during solidification. They explained how, at high cooling rates, the Al leads the front in such a way that it encases the growing Si. In chemical modification they proposed that the modifier increase the interface angle and supresses the growth of Si, thus causing a similar encasement as in the cooling rate modification[19]. However, it was eventually noted that the Si actually leads the Al-Si solid interface[13].

Additionally the low solubility of Na in solid Al and Si was recognised, resulting in segregation at the growing interface. This restricted the diffusion of Si, and by doing so, was responsible for causing the modification[20]. However Davies and West showed that even though Na does actually reduce the diffusion rate of Si in molten Al, the modification also takes place when it is carried out in a Na vapour atmosphere instead of at the time of the direct addition of Na to the melt. This suggested that the reduced diffusion rate is not responsible for the modification[21]. Davies and West went on to show that Na poisoned the Si growth sites and reduced the surface energy. However, they did not believe that this was causing the chemical modification as there was no change in the dihedral angle[22]. Guthy however mentioned that the dihedral angle readings conducted by Davies and West may have been erroneous due to fading of the sodium[17].

The growth-temperature/phase-shape theory was then applied to the Al-Si system. In this theory a plate-like morphology forms when the solidification temperature is high whilst, when the solidification temperature is below 580 °C, the fibrous morphology forms. When applying this theory, the modification elements are responsible for the lowering of the solidification temperature. It was also noted that in modified alloys the growth is from the surface towards the centre, whilst the growth takes place randomly in unmodified alloys[23]. However, the applicability of the growth-temperature/phase-shape theory to Al-Si alloys was discredited and contradicting results were observed for the growth method[24,25].

In the early 1960s Mondolfo presented a series of articles which concluded that surface energies control the heterogeneous nucleation of the eutectic[26–28]. They also established that nucleation between two eutectic phases will occur only in one direction. Thus if a β phase nucleated on an α phase, the nucleation of the α phase cannot take place on the β phase. These studies also showed the importance of AlP as a nucleant for primary and eutectic Si. They demonstrated that in hypoeutectic Al-Si alloys the eutectic Si will start to nucleate on the AlP and above a certain temperature point eutectic Si nucleates on primary Al. However, by adding in a modifier, the AlP sites become poisoned and the nucleation is forced to take place on the primary Al[26]. Even though these articles discuss the nucleation of AlP, they attribute the modification to a change in the leading solidifying phase which is in turn attributed to a change in surface tension and reduction of Si diffusion in the presence of a modifier. They also propose that the Si re-nucleates once it has been completely encased by the Al in modified alloys[28]. However, it was later found that both unmodified and modified alloys are continuous and thus no re-nucleation occurs[29–31].

A number of mechanisms are based on a diversion from the twin plane re-entrant edge (TPRE) mechanism. The flake-like morphology is believed to grow by a mechanism known as the twin plane re-entrant edge (TPRE). This mechanism was first proposed to explain the growth of germanium dendrites and was later on expanded to include Si. In this mechanism, the re-entrant corners are preferred sites for nucleation, thus resulting in a rapid growth in the [211] direction. This growth comes to a halt when a trigonal solid which is surrounded by ridges forms. When two twins occur next to each other, a new edge is formed which provides a further nucleation site[32]. Ge twins were found to occur at least in pairs and thus blockage never occurs[9]. The mechanism is shown pictorially in figure 2.4.

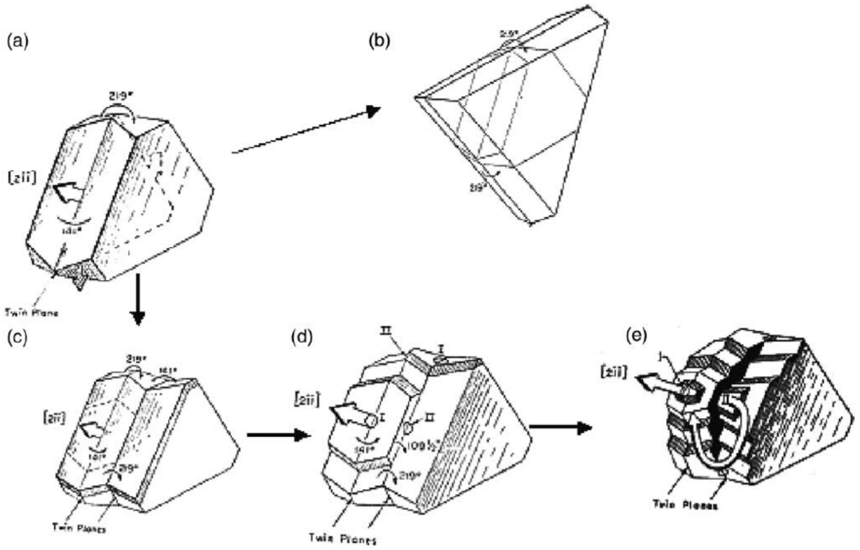

Figure 2.4: The TPRE mechanism (a) single twin crystal, (b) trigonal solid surrounded by ridges, (c) double twin crystal, (d) extra re-entrant corners I and II are created, (e) crystal propagation[9].

Jenkinson and Hogan[33] showed the importance of twins in the growth of fibrous Si. They noted the twinning occurs in chemically modified samples but not in quench modification samples[34,35]. They also confirmed that in unmodified alloys solidification is led by the Si phase which forces the Al to nucleate between Si plates thus forming equiaxed grains[17,36]. In modified eutectics the modifier deposits on the re-entrant twin grooves and reduces the rate at which Si atoms become attached[37]. They proposed that in modified alloys the Al growth catches up with the slowly growing Si and form a common front during growth which causes the fibre-like morphology.

Kobayashi and Hogan[38] suggested that the nucleation for plate-like Si takes place when two tetrahedron structures, made up of Si atoms, combine together to form an octahedron cluster. This leads to Si atoms attaching to this structure to form a critical size nucleus. The growing nucleus minimizes surface energy by forming {111} planes at the corners. The formation of two (or more) {111} planes lead to the TPRE mechanism giving a plate-like structure. Displacement (low growth velocities) and multiple twinning (high growth velocities) may take place and this will cause a change in the direction of plate growth[39]. In displacement twinning the flake will grow at an arbitrary angle to the main flake. In multiple twinning the angle is a multiple of 70.5°, thus sustaining the twin angle. In this case the inter-flake spacing increases and Si atoms are made readily available for the ongoing growth of the Si particle. The orientation relationships between eutectic Si and eutectic Al were determined for different growth velocities[40]. A common relationship is the fact that $(102)_{Al}$ lies parallel to the {111} twin plane of Si. In this arrangement the interplanar spacing at the interface between Al and Si is reduced to a minimum.

Transmission electron microscope (TEM) studies identified that the growth of Si fibres proceeds in a zigzag fashion similar to that taking place in the flake Si[34,41]. It was noted that abundant twinning was present in the unmodified and chemically modified Si but not in the quench modified Si. Furthermore, the chemically modified Si presented much more frequent twinning compared to the unmodified Si. Based on these results Lu and Hellawell [34] concluded that the growth of modified eutectic Si is based on a layer mechanism which they called impurity induced twinning (IIT), rather than by TPRE. This theory stipulated that the chemical modifier was adsorbed on kinks and steps of already growing Si crystals thus preventing further attachment of Si atoms at that site. The adsorbed modifier will also cause a change in how the atomic layers are added on as these are forced to grow around the impurity atoms. By assuming a face-centred cubic (FCC) structure they calculated that the impurity atomic radius must be 1.6457 times greater than the matrix atomic radius[34,42]. However, this theory seems to have a number of shortcomings. It primarily relies on the layer growth mechanism being responsible for flake-like Si, however the plate-like Si morphology cannot be explained by layer growth and it has been shown that the TPRE mechanism plays an important role in unmodified Si[9]. The theory suggests that the twins in flake Si occur due to the difference stresses caused by the much larger thermal expansion of Al as compared to that of Si. The fact that single twins are very rare seems to suggest that these stresses are not responsible for the twinning. Furthermore, the radius ratio calculated does not relate to the fact that Na[2] modifies the morphology much better than ytterbium[3] and calcium[4] do.

---

[2] $r_{Na}/r_{Si}=1.58$
[3] $r_{Yb}/r_{Si}=1.65$
[4] $r_{Ca}/r_{Si}=1.68$

More recently a number of authors combined studies of TEM with APT to visualise the segregation of the modifier elements within the eutectic Si. Timpel et al.[43] noted two types of Al-Si-Sr co-segregations in Sr-modified Al-Si, nanometre-thin rod-like segregations and more extended structures. The authors attributed formation of multiple twins in a Si crystal and its growth in different crystallographic directions to the rod-like segregations, whilst the extended structures were responsible for the growth and control of the branching of a Si crystal. The authors argue that these co-segregations enable IIT and growth restriction mechanisms. In a similar study Barrirero et al.[44] identify three different types of Al-Sr segregations within the eutectic Si of Sr-modified Al-Si alloys: rod-like segregations which promote the smoothening of the Al-Si eutectic boundaries, planar segregations which favour the formation of twin boundaries and particle-like segregations which are a result of the accumulation of Al and Sr at the solidification front. The authors propose that the formation of these nanoclusters helps in the formation and pinning of defects. They also note that Sr segregates preferentially within the Si eutectic phase indicating its importance in the eutectic growth modification. Li et al.[45] performed a similar study looking at Na-modified Al-Si alloys. The authors noticed that Na segregates at the eutectic Al-Si interface and therefore restricts further growth of eutectic Si. In this study the authors also noticed rod-like and particle-like Al-Na segregations. Furthermore they propose that the adsorption of Na occurs at the intersection of multiple Si twins and along the $<112>_{Si}$ growth direction, which they argue provides experimental support for the IIT and poisoning of TPRE growth mechanisms.

Li et al.[46,47] investigated the modification mechanism by looking at europium (Eu) modified Al-Si alloys, Eu being another well-known modification element. In these studies the authors noted Eu-rich clusters along the $<112>_{Si}$ growth direction of Si and at the intersection of two $\{111\}_{Si}$ twins within eutectic Si. They deem these to be strong experimental support for IIT and poisoning of the TPRE growth mechanisms. They also noted small Eu-rich particles which they believe to be $Al_2Si_2Eu$ and coarse $Al_2Si_2Eu$ particles. They suggest that the small particles are segregated out of the Si eutectic during growth, whilst the coarse particles are pre-eutectic formations and have no influence on the modification.

## 2.4. Modification elements

### 2.4.1. Modification by Sodium

Sodium was the first industrially applied element used for modification. However, its application is deemed not highly reliable due to reduced fluidity and rapid loss of sodium by evaporation or oxidation. Excess amounts of Na are therefore required in order to counteract these losses. Such a situation can easily result in over- or under-modification of the castings. Furthermore, the modification effect is lost upon re-melting the alloy. Over-modification leads to coarse silicon plates and intermetallic phases, resulting in deteriorated mechanical properties[1,4,6].

### 2.4.2. Modification by Strontium

The industrially employed substitute to sodium is strontium (Sr), and this has been the preferred modifier since the 1970s. Addition of 0.03 wt% - 0.05 wt% of Sr as an Al-Sr or Al-Si-Sr master alloy produces a casting with comparable properties to those produced by sodium modification. Loss of strontium by evaporation is much less, modification is maintained even after re-melting and excess addition does not cause over-modification issues[4]. The modification using strontium also allows for degassing to be performed, however an excess amount must be added to account for any losses[1,4]. Moreover, the higher the level of silicon in the alloy, the more modifying element needs to be used to ensure that a change in the microstructure is performed. Conversely, the higher the cooling rate, the lower the amount of Sr required for the modification[1]. This modification improves mechanical properties, pressure tightness, machinability, reduces hot tear resistance and significantly raises fracture toughness[1,3,4].

### 2.4.3. Modification by other elements

A number of elements have been researched as alternatives to Na and Sr. A summary of these findings can be found in table 2.2. A more detailed approach to the findings relating to the application of cerium and yttrium, the elements being used in this research, can be found in sections 2.4.3.1 and 2.4.3.2 respectively.

#### *2.4.3.1. Modification by Cerium*

Nogita et al.[48] conducted a series of tests in which they tested various rare earth metals, amongst which was cerium. In this study they noted that the addition of Ce, similar to most other rare earth metals, causes a decrease in the nucleation and growth temperature. The maximum modification for Ce was achieved at 19,700 ppm but the modification was limited to a refinement of the plate-like morphology rather than a complete change to fibre-like structures.

Similarly, Tsai et al.[49] added varying amounts of Ce to A356 aluminium alloy, up to 1% addition. They reported that the microstructure is well-refined at 1% Ce and a decrease in nucleation and growth temperature with addition of Ce was also reported. Ce addition above 0.6% showed a progressive improvement in the elongation properties of the alloy.

In a recent publication, by Vijeesh and Prabhu[50] significant discrepancies to the above were reported. It was similarly reported that the casting will produce a refined structure, however this caused an increase in both the nucleation and growth temperature. In this article, it was also reported that a full modification was achieved by the combined effect of chill-casting and Ce addition. In this case a decrease in the growth and nucleation temperatures was noted, though the authors did not suggest an explanation to this observation.

#### *2.4.3.2. Modification by Yttrium*

Nogita et al. published a series of articles describing the modification of Al-Si alloys by means of various chemical additions[51–53] including the effect of yttrium (Y) on A356 alloy. They noted that Y produces a plate-like refined structure from 700 ppm up to 5200 ppm, which was the maximum concentration they tested for[52,53]. They also noted that upon adding Y the eutectic nucleation temperature drops significantly and remains constant with further additions. A similar behaviour was reported for the eutectic undercooling as a large increase in the undercooling was noted which then remained constant with increasing Y content[52]. They found that, whereas in unmodified Al-Si the nucleation of the eutectic occurs on the dendrites, in Y modified alloy the growth of the eutectic commences from the walls opposite a thermal gradient and independent of the dendrites. A similar solidification behaviour was recorded for calcium and ytterbium, whereas for barium solidification was seen both on the dendrites and independently in the interdendritic liquid[52]. They also recorded how Y modified alloys show porosity mainly in the hot spot, as the growing eutectic from the surface pushes any gases to a central hot spot[51].

Li et al.[54] further investigated the effect of yttrium on the modification of an Al-7.5Si-0.5Mg alloy, its heat treatment and mechanical properties. They noted that: at 0.1% addition, a refined morphology is observed, at 0.3% the microstructure is finely branched and also some fibrous structures can be observed, whilst at 0.5% the structure reverts back to a coarse one. However, these results contrasted with those obtained by Nogita et al. and they attributed this to the difference in cooling rates used. They also noted that spherodization due to T6 heat treatment was optimized by 0.3% Y addition. Following the Y addition there was also a slight improvement in the tensile properties and the fracture mode changed to dimple-mode from quasi-cleavage.

Li and Schumacher[55] added a trace amount (200 ppm) of  Y to Al-5wt% Si. In conventional sand casting this trace amount caused a refined plate-like eutectic Si microstructure whilst under melt spinning conditions a much finer eutectic Si with multiple Si twinning was noted.

Y was also noted to reduce porosity when added to cast 6061 aluminium alloys. This reduction in porosity was attributed to the hydrogen binding energies and the diffusion activation energies of hydrogen in Y containing phases[56].

Table 2.2: Literature highlights of elements tested for application in modification of eutectic Si in Al-Si alloys

| **Element** | **Amount added (ppm)** | **Amount in melt (ppm)** | **Method of addition** | **Alloy** | **Results** | **Ref** |
|---|---|---|---|---|---|---|
| Barium | 1000-6000 | 200-1010 | Metal in foil | A356 | Modification achieved between 890 and 1010 ppm (increasing level of modification at higher concentrations) | 53 |
| Calcium | 100-800 | 36-210 | Metal in foil | A356 | Modification achieved at low levels (36 ppm) and increased with increasing concentration, best at 210 ppm but predicted to increase at higher concentrations. | 53 |
|  | - | 0-400 | Master alloy (Al-10%Ca) | A357 | Partial modification at slow cooling rates (sand casting), full modification at high cooling rates (steel mould) | 57 |
|  | 20-2000 | - | Master alloy (Al-75%Ca) | Al-7Si-3Cu-Fe, Al-7Si-3Cu-Fe-0.5Mn, A319, A380, | Above 40 ppm refinement of eutectic Si and coarsening of Fe intermetallics | 58 |

| | | | | | | |
|---|---|---|---|---|---|---|
| | | | | Al-12Si-Mg-Ni-Cu | | |
| Ytterbium | 1000-6000 | 940-6400 | Metal in foil | A356 | At 2900 ppm refinement is noticeable, increases with increasing concentration | 53 |
| | - | highest modification at 13900 | - | Comercial purity Al + 10%Si | Refined microstructure | 48 |
| Antimony | not specified | not specified | Pure element | - | Refined microstructure | 12 |
| Mischmetal | Up to 20000 | - | Mischmetal plunged into melt using graphite rod | 356 | In graphite mould some modification is observed at 7500 ppm and is complete at 2%, in sand mould (2 cm diameter) some modification is observed at 10000 ppm and substantial at 20000 ppm | 59 |
| Lanthanum | - | highest modification at 17300 | not specified | Comercial purity Al + 10%Si | Refined microstructure | 48 |
| | - | 2000 – 10000 | Pure element | A356 | Refined microstructure | 60 |

|  |  |  |  |  |  |  |
|---|---|---|---|---|---|---|
| Praseodymium | - | highest modification at 17200 | not specified | Comercial purity Al + 10%Si | Refined microstructure | 48 |
| Neodymium | - | highest modification at 14800 | not specified | Comercial purity Al + 10%Si | Refined microstructure | 48 |
| Samarium | - | highest modification at 19700 | not specified | Comercial purity Al + 10%Si | Refined microstructure | 48 |
|  | - | 3000 – 9000 | Master alloy in foil (Al-15%Sm) | A357 | Modified fibrous microstructure at 6000 ppm, refined at 3000 ppm and 9000 ppm | 61 |
| Europium | - | highest modification at 600 | not specified | Comercial purity Al + 10%Si | Fully modified fibrous microstructure | 48 |
|  | - | 500 | Master alloy (Al-5%Si-2%Eu) | High purity designed alloy | Fully modified fibrous microstructure | 47 |

| | | | | | | |
|---|---|---|---|---|---|---|
| Gadolinium | - | highest modification at 30300 | not specified | Comercial purity Al + 10%Si | Refined microstructure | 48 |
| | - | 1000 – 4000 | Master alloy (Al-10%Gd) | A356 | Refined microstructure (optimum at 2000 ppm and T6 treatment) | 62 |
| Terbium | - | highest modification at 25300 | not specified | Comercial purity Al + 10%Si | Refined microstructure | 48 |
| Dysprosium | - | highest modification at 14300 | not specified | Comercial purity Al + 10%Si | Refined microstructure | 48 |
| Holmium | - | highest modification at 18700 | not specified | Comercial purity Al + 10%Si | Refined microstructure | 48 |
| Erbium | - | highest modification at 17900 | not specified | Comercial purity Al + 10%Si | Refined microstructure | 48 |
| | - | 1000 – 4000 | Master alloy (Al-10Er) | A356 | Refined microstructure (optimum at 3000 ppm and T6 treatment) | 63 |

| | | | | | | |
|---|---|---|---|---|---|---|
| Thulium | - | highest modification at 12900 | not specified | Comercial purity Al + 10%Si | Refined microstructure | 48 |
| Lutetium | - | highest modification at 12700 | not specified | Comercial purity Al + 10%Si | Refined microstructure | 48 |

## 2.5. The effect of modification on porosity

The main issue with Sr modification is the introduction of porosity within the final cast alloy and the adverse effects that porosity has on the mechanical properties of the alloy, with some users stating that the increase in porosity negates the beneficial effects coming from the modification[64–68].

Porosity in castings can be generated as a result of differences in solubilities for the solid and liquid phases, density differences between the liquid and solid phases leading to shrinkage, and poor feeding properties of the liquid phase[69]. Emadi et al.[69] listed the factors which could cause the increase in porosity upon addition of strontium. A number of possibilities focus on the role of hydrogen as an increase in the hydrogen content of the melt, the absorption of hydrogen into the oxides and a reduction of hydrogen solubility in the solid state or increase in the liquid state are all possible contributors to the increase in porosity. Depression in the solidification temperature also allows more time for hydrogen diffusion and porosity growth. Other possible causes listed are the increase in the inclusion content of the melt, a reduction in the surface tension of the molten metal and increased volumetric shrinkage. Reduction in the interdendritic feeding, by changing the solid-liquid interface shape, increasing the length of mushy zone and an increase in liquid's viscosity, could also be responsible for the increase in porosity.

Denton and Spittle[70] noted that the hydrogen content in the melt increases upon addition of the master alloy and this increase is not dependent on the quantity of Sr added. They suggested that the Sr affects the properties of the oxide film at the melt surface, as oxidised Sr causes this surface layer to become more permeable to hydrogen. It has also been shown that the addition of Sr to the melt causes a thicker but non-homogeneous surface oxide layer[71]. Atwood et al.[65] developed a model that related the pore nucleation rate as a function of temperature. They noted that, as the undercooling increases, the sites for potential pore nucleation increase and once the pores nucleate, the hydrogen starts to diffuse into them leading to a decrease of available hydrogen. Emadi et al.[69] showed that 0.01 wt% Sr addition to super-purity Al causes a reduction in surface tension of about 2%. Furthermore, 0.01 wt% Sr addition to A356 alloy decreases surface tension by 19% and increases volumetric shrinkage by 12%. However, they argue that these factors do not fully account for the increase in porosity. The modification also promotes the early formation of pores during solidification thus allowing for a longer period of growth resulting in larger pores[69,72]. During the eutectic solidification the dendrites are fixed in place but the eutectic phase is still mostly a liquid. Fuoco et al.[73–75] noted that whereas in the unmodified alloy the eutectic liquid seemed to flow between the dendrites, for the Sr modified alloy no mobility of this liquid was observed. Dahle et al.[15] indicated that this could be resulting from the eutectic phase growing as an equiaxed grain which could inhibit interdendritic flow and encourage shrinkage porosity. Campbell and Tiryakioğlu[72] argue that the lack of interdendritic flow is due to oxide bifilms. In the unmodified alloy Si nucleates on the bifilms and grows around them preventing them from blocking the flow of the liquid. However, in the Sr modified alloy the bifilms remain in the suspension, allowing them to block the interdendtitic flow. Furthermore, these bifilms will open up to fill the voids left by lack of interdendritic flow, thus becoming pores. The links of oxides to porosity have been shown in a number of studies showing that: the fluidity of the melt is reduced by increasing oxide content[76,77], the amount of porosity is dependent on the level of SrO in the solidified casting in the melt rather than Sr[78], and that there is no increase in porosity if the oxides were removed by fluxing prior to Sr addition and vacuum degassed after addition[79]. Liao et al.[64] show that after addition of Sr to the melt diffusion of the oxide inclusions occurs, enhancing the effectiveness of the oxide in the liquid alloy as pore nucleation sites. This also results in a significant rise in the nucleation temperature which allows for a longer pore growth period.  The formation of these oxides is thermodynamically favoured and the stoichiometric composition was found to be $Al_2SrO_3$[80].

A significant amount of research has been carried out with respect to the effect of porosity on the mechanical properties, mainly fatigue, of Al alloys. A number of microstructures and defects can be sites for fatigue crack initiation. These include oxide films, micro-cells which consist of Al-matrix and associated Si-particles, and porosity[81]. It is well known that porosity is a potent initiator for fatigue cracks[82]. Wang et al.[83] studied the effect of oxides and porosity on the fatigue life and noted that porosity is more detrimental, indicating that a critical pore size of half the critical oxide film size initiates a pore in Sr-modified A356-T6 alloy at the tested conditions. It has been shown that large pores at the surface of the specimen are mainly responsible for initiating cracks in A356-T6 castings, whilst smaller pores within micro-cells consisting of Al matrix and associated Si particles can significantly reduce the fatigue lifetime[81,82,84]. A number of researchers have devised relationships between the pore properties and the resultant fatigue life, mainly focusing on pore size, pore density (or nearest neighbour distance) standard deviation of pore size, and also dendrite cell size in order to predict fatigue life in the casting alloy[82,85]. The Si flake particles also show great influence on the fatigue-crack propagation[84].

## 2.6. Aims and Objectives

In the literature extensive studies have been undertaken looking into the modification mechanism that takes place following the addition of elements that fully modify the eutectic Si, however, studies looking into the mechanism taking place following refinement are minimal and often only assess the degree of modification. Furthermore, though previous research has demonstrated that rare earth additions can reduce the porosity in Al alloys, no studies have investigated the possibility of reducing the effect of Sr addition on porosity specifically, by adding rare earth elements.

Therefore this thesis has the following objectives:

- To provide an understanding of the modification of the eutectic Si in hypoeutectic Al-Si alloys by comparing the differences between full modification, as obtained by Sr and partial modification or refinement as obtained by Ce and Y. The synergistic effect of combining Ce or Y with Sr will also be investigated.
- To investigate whether rare earth additions such as Ce or Y have the potential to reduce the porosity within Sr-modified cast Al-Si alloys.

## 2.7. Thesis Overview

Chapters 2-4 address the first objective of this thesis, i.e. to provide an understanding for the modification mechanism of Al-Si. Chapter 2 studies the effect of adding 1% Ce to unmodified Al-Si and Sr-modified Al-Si. The microstructure is characterised and quantified by optical microscopy and scanning electron microscopy (SEM). The solidification of the alloys is characterised by thermal analysis and differential scanning calorimetry (DSC). The intermetallics are characterised by x-ray diffraction (XRD) and SEM-energy dispersive spectroscopy (EDS). The relationship between primary Al and eutectic Al is also explored by SEM-electron backscattered diffraction (EBSD). Similarly, in chapter 3 1% Y is added to Al-Si alloys instead of 1% Ce and a similar analysis is performed. In chapter 4 APT is used to understand the segregation of Y between the eutectic Al and eutectic Si.

Chapters 5 and 6 investigate the second objective of this thesis. In chapter 5 lab-based submicron resolution XCT was used to visualise, quantify and compare porosity in Al-Si and Sr-modified Al-Si alloys. Furthermore, the formation of Al-Si-Sr intermetallics in Sr modified Al-Si alloys were studied by XCT and SEM analysis. Chapter 6 presents a study using 2D and 3D imaging techniques to quantify the porosity in unmodified Al-Si and compare this to Al-Si alloys to which Ce or Y or Sr or a combination of Ce or Y with Sr has been added. The presence of the intermetallics in these alloys is also investigated.

## 2.8. References

1. Bartley, R. *British and European Aluminium Casting Alloys*. (Association of Light Alloy Refiners, 1996).
2. Elliott, R. Aluminium-Silicon Alloys and Cast Irons: commercially important anomalous alloys. in *Eutectic Solidification Processing: Crystalline and Glassy Alloys* 157–231 (Butterworths, 1983).
3. Hatch, J. E. *Aluminium: Properties and Physical Metallurgy*. (American Society of Metals, 1984).
4. Polmear, I. J. Cast Aluminium Alloys. in *Light Alloys* 205–235 (Elsevier,

2005). doi:10.1016/B978-075066371-7/50008-6

5. Murray, J. L. & McAlister, A. J. The Al-Si (Aluminum-Silicon) system. *Bull. Alloy Phase Diagrams* **5**, 74–84 (1984).
6. Davis, J. R. *ASM Speciality Handbook: Aluminum and Aluminum Alloys*. (ASM International, 1993).
7. Srirangam, V. S. P. *et al.* XAFS studies on a modified Al-Si hypoeutectic alloy. *J. Phys. Conf. Ser.* **190**, 012068 (2009).
8. Pacz, A. Alloy. (1921).
9. Makhlouf, M. M. & Guthy, H. V. The aluminum–silicon eutectic reaction: mechanisms and crystallography. *J. Light Met.* **1**, 199–218 (2001).
10. Schulz, E. Mikroskopische Untersuchungen bei der Veredelung von Silumin. *Zeitschrift für Met.* **39**, 123–125 (1949).
11. Barrirero, J. *et al.* Cluster formation at the Si/liquid interface in Sr and Na modified Al–Si alloys. *Scr. Mater.* **117**, 16–19 (2016).
12. Bian, X. F., Wang, W. M. & Qin, J. Y. Structures of Liquid Al-Si Alloy Modified by Sr. *Mater. Sci. Forum* **331**–**337**, 349–354 (2000).
13. Flood, S. C. & Hunt, J. D. Modification of Al-Si eutectic alloys with Na. *Met. Sci.* **15**, 287–294 (1981).
14. Hanna, M. D., Lu, S. & Hellawell, A. Modification in the aluminum silicon system. *Metall. Trans. A* **15**, 459–469 (1984).
15. Dahle, A. K., Nogita, K., McDonald, S. D., Zindel, J. W. & Hogan, L. M. Eutectic nucleation and growth in hypoeutectic Al-Si alloys at different strontium levels. *Metall. Mater. Trans. A* **32**, 949–960 (2001).
16. Xiufang, B., Weimin, W. & Jingyu, Q. Liquid structure of Al–12.5% Si alloy modified by antimony. *Mater. Charact.* **46**, 25–29 (2001).
17. Guthy, H. V. Evolution of the Eutectic Microstructure in Chemically Modified and Unmodified Aluminum Silicon Alloys. (Worcester Polytechnic Institute, 2002).
18. Srirangam, P. *et al.* Probing the local atomic structure of Sr-modified Al–Si alloys. *Acta Mater.* **65**, 185–193 (2014).
19. Thall, B. M. & Chalmers, B. Modification in aluminum-silicon alloys. *J. Inst. Met.* **78**, 79 (1949).
20. Tsumura, Y. On the Theory of Modification of Aluminium-Silicon Alloys. *J. Japan Inst. Met.* **21**, 69–83 (1957).

21. Davies, V. L. & West, J. M. Factors affecting the modification of Al-Si eutectic. *J. Inst. Met.* **92**, 175–180 (1964).

22. Davies, V. L. & West, J. M. Influence of small additions of sodium on the surface tension of Al and Al-Si alloys. *J. Inst. Met.* **92**, 208–210 (1964).

23. Kim, C. B. & Heine, R. W. Fundamentals of modification in the aluminium-silicon system. *J. Inst. Met.* **92**, 367–376

24. Gigliotti, M. F. X. & Colligan, G. A. The effects of sodium on the growth velocity and growth morphology of silicon in Al-Si alloys. *Metall. Trans.* **3**, 933–940 (1972).

25. Dahle, A. K. & Arnberg, L. Investigation of the dendrite coherency point in solidifying Al-Si foundry alloys. in *Proceedings 4th international conference on aluminum alloys* 91–98 (1994).

26. Mondolfo, L. F. Nucleation in eutectic alloys. *J. Aust. Inst. Met.* **10**, 169–177 (1965).

27. Sundquist, B. E., Bruscato, R. & Mondolfo, L. F. The surface energy of solid metals. *J. Inst. Met.* **91**, 204–208 (1963).

28. Crosley, P. B. & Mondolfo, L. F. The modification of aluminum-silicon alloys. *Trans. Am. foundrymen's Soc.* **74**, 53–64 (1966).

29. Day, M. G. & Hellawell, A. The structure of modified aluminium-silicon eutectic alloy. *J. Inst. Met.* **95**, 377 (1967).

30. Day, M. G. & Hellawell, A. The Microstructure and Crystallography of Aluminium-Silicon Eutectic Alloys. *Proc. R. Soc. London A Math. Phys. Eng. Sci.* **305**, 473–491 (1968).

31. Bell, J. A. E. & Winegard, W. C. Interconnexion of Silicon in Modified Aluminium-Silicon Eutectic. *Nature* **208**, 177 (1965).

32. Hamilton, D. . & Seidensticker, R. G. Propagation Mechanism of Germanium Dendrites. *J. Appl. Phys.* **31**, 1165–1168 (1960).

33. Jenkinson, D. C. & Hogan, L. M. The modification of aluminium-silicon alloys with strontium. *J. Cryst. Growth* **28**, 171–187 (1975).

34. Lu, S. & Hellawell, A. Growth mechanisms of silicon in Al-Si alloys. *J. Cryst. Growth* **73**, 316–328 (1985).

35. Atasoy, O. A., Yilmaz, F. & Elliott, R. Growth structures in aluminium-silicon alloys I. The coupled zone. *J. Cryst. Growth* **66**, 137–146 (1984).

36. McLeod, A. J., Hogan, L. M., Adam, C. M. & Jenkinson, D. C. Growth mode

of the aluminum phase in Al-Si and Al-Al3Fe eutectics. *J. Cryst. Growth* **19**, 301–309 (1973).

37. Steen, H. A. . & Hellawell, A. The growth of eutectic silicon—contributions to undercooling. *Acta Metall.* **23**, 529–535 (1975).
38. Kobayashi, K. F. & Hogan, L. M. The crystal growth of silicon in Al-Si alloys. *J. Mater. Sci.* **20**, 1961–1975 (1985).
39. Shamsuzzoha, M. & Hogan, L. M. Twinning in fibrous eutectic silicon in modified Al-Si Alloys. *J. Cryst. Growth* **72**, 735–737 (1985).
40. Shamsuzzoha, M. & Hogan, L. M. Crystal morphology of unmodified aluminium-silicon eutectic microstructures. *J. Cryst. Growth* **76**, 429–439 (1986).
41. Shamsuzzoha, M. & Hogan, L. M. The crystal morphology of fibrous silicon in strontium-modified Al-Si eutectic. *Philos. Mag. A* **54**, 459–477 (1986).
42. Lu, S.-Z. S. & Hellawell, A. The mechanism of silicon modification in aluminum-silicon alloys: Impurity induced twinning. *Metall. Trans. A* **18**, 1721–1733 (1987).
43. Timpel, M. *et al.* The role of strontium in modifying aluminium–silicon alloys. *Acta Mater.* **60**, 3920–3928 (2012).
44. Barrirero, J. *et al.* Comparison of segregations formed in unmodified and Sr-modified Al–Si alloys studied by atom probe tomography and transmission electron microscopy. *J. Alloys Compd.* **611**, 410–421 (2014).
45. Li, J. H. *et al.* Nucleation and Growth of Eutectic Si in Al-Si Alloys with Na Addition. *Metall. Mater. Trans. A* **46**, 1300–1311 (2015).
46. Li, J. H. *et al.* Modification of eutectic Si in Al–Si alloys with Eu addition. *Acta Mater.* **84**, 153–163 (2015).
47. Li, J. *et al.* The roles of Eu during the growth of eutectic Si in Al-Si alloys. *Sci. Rep.* **5**, 13802 (2015).
48. Nogita, K., McDonald, S. D. & Dahle, A. K. Eutectic Modification of Al-Si Alloys with Rare Earth Metals. *Mater. Trans.* **45**, 323–326 (2004).
49. Tsai, Y. C., Lee, S. L. & Lin, C. K. Effect of trace Ce addition on the microstructures and mechanical properties of A356 (AL–7SI–0.35 Mg) aluminum alloys. *J. Chinese Inst. Eng.* **34**, 609–616 (2011).
50. Vijeesh, V. & Prabhu, K. N. The Effect of Cooling Rate and Cerium Melt Treatment on Thermal Analysis Parameters and Microstructure of

Hypoeutectic Al-Si Alloy. in *Light Metals 2015* 403–407 (John Wiley & Sons, Inc., 2015). doi:10.1002/9781119093435.ch67

51. Knuutinen, A., Nogita, K., McDonald, S. D. & Dahle, A. K. Porosity formation in aluminium alloy A356 modified with Ba, Ca, Y and Yb. *J. Light Met.* **1**, 241–249 (2001).
52. Nogita, K., Knuutinen, A., McDonald, S. D. & Dahle, A. K. Mechanisms of eutectic solidification in Al–Si alloys modified with Ba, Ca, Y and Yb. *J. Light Met.* **1**, 219–228 (2001).
53. Knuutinen, A., Nogita, K., McDonald, S. D. & Dahle, A. K. Modification of Al–Si alloys with Ba, Ca, Y and Yb. *J. Light Met.* **1**, 229–240 (2001).
54. Li, B., Wang, H., Jie, J. & Wei, Z. Effects of yttrium and heat treatment on the microstructure and tensile properties of Al–7.5Si–0.5Mg alloy. *Mater. Des.* **32**, 1617–1622 (2011).
55. Li, J. H. & Schumacher, P. Effect of Y addition and cooling rate on refinement of eutectic Si in Al–5 wt-%Si alloys. *Int. J. Cast Met. Res.* **25**, 347–357 (2012).
56. Hua, G., Ahmadi, H., Nouri, M. & Li, D. Positive effect of yttrium on the reduction of pores in cast Al alloy. *Mater. Chem. Phys.* **149**–**150**, 140–144 (2015).
57. Abdollahi, A. & Gruzleski, J. E. An evaluation of calcium as a eutectic modifier in A357 alloy. *Int. J. Cast Met. Res.* **11**, 145–155 (1998).
58. Zaldívar-Cadena, A. A. & Flores-Valdés, A. Prediction and identification of calcium-rich phases in Al–Si alloys by electron backscatter diffraction EBSD/SEM. *Mater. Charact.* **58**, 834–841 (2007).
59. Ye, B. J. An assessment of the role of rare earth in the eutectic modification of cast Al-Si. *Trans. Am. Foundrymen's Soc.* **93**, 533–544 (1985).
60. Tsai, Y. C. *et al.* Effect of trace La addition on the microstructures and mechanical properties of A356 (Al–7Si–0.35Mg) aluminum alloys. *J. Alloys Compd.* **487**, 157–162 (2009).
61. Qiu, H., Yan, H. & Hu, Z. Effect of samarium (Sm) addition on the microstructures and mechanical properties of Al–7Si–0.7Mg alloys. *J. Alloys Compd.* **567**, 77–81 (2013).
62. Shi, Z., Wang, Q., Shi, Y., Zhao, G. & Zhang, R. Microstructure and mechanical properties of Gd-modified A356 aluminum alloys. *J. Rare Earths*

**33**, 1004–1009 (2015).

63. Shi, Z. M., Wang, Q., Zhao, G. & Zhang, R. Y. Effects of erbium modification on the microstructure and mechanical properties of A356 aluminum alloys. *Mater. Sci. Eng. A* **626**, 102–107 (2015).
64. Liao, H. C. *et al.* Effect of Sr addition on porosity formation in directionally solidified A356 alloy. *Int. J. Cast Met. Res.* **26**, 201–208 (2013).
65. Atwood, R. C., Sridhar, S. & Lee, P. D. Equations for nucleation of hydrogen gas pores during solidification of aluminium seven weight percent silicon alloy. *Scr. Mater.* **41**, 1255–1259 (1999).
66. Byczynski, G. E. & Cusinato, D. A. The effects of strontium and grain refiner additions on the fatigue and tensile properties of industrial Al-Si-Cu-Mg alloy castings produced using the Ford Motor Company - Cosworth precision sand process. *Int. J. Cast Met. Res.* **15**, 315–324 (2002).
67. Hetke, A. & Grundlach, R. B. Aluminum casting quality in alloy 356 engine components. *AFS Trans.* **102**, 367–380 (1994).
68. Brosnan, M. & Shivkumar, S. Elevated Temperature Tensile Properties and Fracture Behavior of A356 Castings. *AFS Trans.* **103**, 727–737 (1995).
69. Emadi, D., Gruzleski, J. E. & Toguri, J. M. The effect of Na and Sr modification on surface tension and volumetric shrinkage of A356 alloy and their influence on porosity formation. *Metall. Trans. B* **24**, 1055–1063 (1993).
70. Denton, J. R. & Spittle, J. A. Solidification and susceptibility to hydrogen absorption of AL–Si alloys containing strontium. *Mater. Sci. Technol.* **1**, 305–311 (1985).
71. Jacob, M. *et al.* État Actuel de l'Utilisation du Sodium, du Strontium et de l'Antimonie dans les Alliages Aluminium-Silicium Moulés. *Hommes et Fonderie* **258**, 45–54 (1995).
72. Campbell, J. & Tiryakioğlu, M. Review of effect of P and Sr on modification and porosity development in Al–Si alloys. *Mater. Sci. Technol.* **26**, 262–268 (2010).
73. Fuoco, R., Correa, E. R. & Correa, A. V. O. Effect of modification treatment on microporosity formation in 356 Al alloy. *AFS Trans.* **103**, 379–387 (1995).
74. Fuoco, R., Correa, E. R. & Goldenstein, H. The effect of modification treatment on microporosity formation in 356 Al Alloy, part I: Interdendritic Feeding Evaluation. *AFS Trans.* **104**, 1151–1158 (1996).

75. Fuoco, R., Correa, E. R. & Bastos, M. de A. Effects of Grain Refinement on Feeding mechanisms in A356 Aluminum Alloy. *AFS Trans.* **106**, 401–409 (1998).

76. Groteke, D. E. Influence of SNIF Treatment on Characteristics of Aluminium Foundry Alloys. *AFS Trans.* **93**, 953–960 (1985).

77. Di Sabatino, M., Rørvik, S. & Prestmo, A. The influence of oxide inclusions on the fluidity of Al–7wt.%Si alloy. *Mater. Sci. Eng. A* **413**, 272–276 (2005).

78. Liu, L., Samuel, M., Samuel, F. H., Doty, H. W. & Valtierra, S. The role of Sr oxide on porosity. *AFS Trans.* **110**, 449–462 (2002).

79. Iwahori, H., Yonekura, K., Yamamoto, Y. & Nakamura, M. Occurring Behavior of Porosity and Feeding Capability of Sodium- and Strontium-Modified Al-Si Alloys. *AFS Trans.* **98**, 167–173 (1990).

80. Liu, L., Samuel, A. M., Samuel, F. H., Doty, H. W. & Valtierra, S. Influence of oxides on porosity formation in Sr-treated Al-Si casting alloys. *J. Mater. Sci.* **38**, 1255–1267 (2003).

81. Yi, J. Z., Lee, P. D., Lindley, T. C. & Fukui, T. Statistical modeling of microstructure and defect population effects on the fatigue performance of cast A356-T6 automotive components. *Mater. Sci. Eng. A* **432**, 59–68 (2006).

82. Yi, J. Z., Gao, Y. X., Lee, P. D., Flower, H. M. & Lindley, T. C. Scatter in fatigue life due to effects of porosity in cast A356-T6 aluminum-silicon alloys. *Metall. Mater. Trans. A* **34**, 1879–1890 (2003).

83. Wang, Q. ., Apelian, D. & Lados, D. . Fatigue behavior of A356-T6 aluminum cast alloys. Part I. Effect of casting defects. *J. Light Met.* **1**, 73–84 (2001).

84. Mo, D.-F., He, G.-Q., Hu, Z.-F., Liu, X.-S. & Zhang, W.-H. Effect of microstructural features on fatigue behavior in A319-T6 aluminum alloy. *Mater. Sci. Eng. A* **527**, 3420–3426 (2010).

85. Jordon, J. B. *et al.* Microstructural Inclusion Influence on Fatigue of a Cast A356 Aluminum Alloy. *Metall. Mater. Trans. A* **41**, 356–363 (2010).

# Chapter 3:

# Modification of Al-Si alloys by Ce or Ce with Sr

## Summary

This chapter seeks to address the first objective of this thesis, that is understanding the modification mechanism of hypoeutectic Al-Si alloys by comparing full modification and partial modification. The partial modification was carried out by adding 1% Ce to hypoeutectic Al-Si alloys, whilst full modification was obtained by the addition of 0.04% Sr. Samples modified by both Ce and Sr were also investigated in order to understand the synergistic effect of the two elements in the same alloy. The various solidification and microstructural studies carried out on these samples will be presented herein whilst carrying out a comparison of the different modifications achieved.

This is published work as indicated below and three authors have contributed, the author (M. De Giovanni), the author’s thesis supervisor (P. Srirangam) and Dr. Kaduk who is the president and principal scientist at Poly Crystallography, Inc. The author’s contribution to this publication was sample preparation, carrying out most of the experimental work (microstructural examination by means of optical microscopy, SEM-EDS/EBSD and solidification analysis by means of thermal analysis and DSC), analysis of results and the writing up of the publication. Dr. Kaduk carried out the XRD experimental work, whilst Dr. Srirangam contributed intellectually.

*Results in this chapter published as:*

*De Giovanni, M., Kaduk, J. A. & Srirangam, P. Modification of Al-Si Alloys by Ce or Ce with Sr. JOM 1–9 (2018). doi:10.1007/s11837-018-3192-6*

## 3.1. Abstract

Al-Si alloys were modified by addition of cerium (Ce) or Ce plus strontium (Sr) to study the effect on the eutectic silicon (Si) morphology. The modified alloys were characterised using scanning electron microscopy (SEM), x-ray diffraction (XRD) analysis, and thermal analysis to understand the effect of Ce and Sr on their microstructure. The results showed that addition of 1% Ce resulted in only partial modification of the Si phase, whereas addition of Ce with 0.04% Sr resulted in complete modification of the alloy. Addition of 1% Ce decreased the eutectic arrest temperature by about 10 °C compared with a 5 °C drop with Sr addition only. SEM-energy dispersive spectroscopy (EDS) and XRD results revealed formation of $Al_2Si_2Ce$ intermetallic in the Ce-modified Al-Si alloys. Differential scanning calorimetry (DSC) shows that the intermetallic forms just before the eutectic phase.

**Keywords:** Al-Si alloys, modification, cerium, strontium.

## 3.2. Introduction

Aluminium-Silicon (Al-Si) alloys are widely used in the automotive and aerospace industries due to their high strength-to-weight ratio, good castability and excellent mechanical and performance properties[1]. Slow solidification of such alloys produces a very coarse microstructure where the eutectic is composed of large plates or needles of Si in a continuous aluminium matrix. Alloys exhibiting this microstructure show low ductility due to the large and brittle Si plates. However, this coarse Si morphology can be modified into a fine and fibrous one by increasing the cooling rate or via chemical modification, improving the ductility and tensile strength of the alloy[1,2]. The first chemical modifier used industrially was sodium (Na). However, since the 1970s the preferred modification element has been strontium (Sr), mainly due to its higher retention in the cast alloy and the lack of significant overmodification issues. Such microstructural modification can improve the mechanical properties, pressure tightness, and machinability, reduce the hot tear resistance and significantly increases fracture toughness of the alloy[1–3].

Significant research has been carried out into the effect of various chemical elements, such as rare earths, for modification of Al-Si alloys[4–9]. One such example is cerium (Ce). Previous research has shown that addition of 1% Ce to Al-Si alloys results in only partial modification of the Si morphology and an improvement in the mechanical properties of the alloy[10]. The Si morphology can be further refined by increasing the amount of Ce added to the alloy, whilst a fine fibrous structure can be obtained by combining Ce and chill casting[9].

The mechanism by which the modification carried out by Sr and Na occurs has been greatly debated. Most theories focus on either growth-restriction-based-theories, mainly impurity-induced- twinning (IIT)[11,12] or restricted growth[13] or nucleation-based effects focusing on the formation of $Al_2Si_2Sr$ (or similar) particles that deactivate eutectic Si nucleation sites[14–16].

The aim of this work is to provide a basis to study the mechanistic differences between full modification, as achieved by using Sr, and the partial modification achieved by Ce. This is done by quantifying the modification achieved, characterising the solidification of the alloys by thermal analysis, and identifying any intermetallics formed. The synergistic effect of combining Ce with Sr on the modification of the eutectic Si morphology in Al-Si hypoeutectic alloys is also investigated.

## 3.3. Methodology

### 3.3.1. Alloy Preparation

Al-Si hypoeutectic alloy was prepared by melting 99.999% purity Al (NewMet, UK) and 99.999% Si (Alfa Aeser, UK) in a clay graphite crucible using a Carbolite RHF1500 high-temperature furnace. Once the alloy was molten at 750 °C, the metal was stirred using a graphite rod, poured into a preheated clay graphite crucible, and left to solidify. The cast Al-Si alloy was then used to prepare the modified alloys. The Al-Si alloy was remelted to allow for addition of Ce and Sr metals in the form of Al-10Ce (wt%) and Al-10Sr (wt%) master alloys respectively. These alloys were poured into a preheated cylindrical graphite mould. The master alloys were produced similarly using the same 99.999% purity Al and 99% purity Sr (Alfa Aeser, UK) and 99.8% purity Ce (Alfa Aeser, UK), respectively. Four alloys were prepared with the following approximate compositions: Al-8 wt.%Si, Al-8 wt.%Si-0.04 wt.%Sr, Al-8 wt.%Si-1 wt.%Ce and Al-8 wt.%Si-1 wt.%Ce-0.04 wt.%Sr. The chemical composition of each alloy was analysed using inductively couple plasma optical emission spectroscopy (ICP-OES) and are presented in table 3.1. These concentrations of Ce and Sr in the alloys were chosen based on previous research and industrial practices[2,9,10].

Table 3.1: ICP-OES chemical composition analysis performed on the four alloys in weight percentage (wt%).

| | **Al** | **Si** | **Ce** | **Sr** | **Fe** | **Cu** | **Mn** |
|---|---|---|---|---|---|---|---|
| **Al-Si** | Balance | 8.82 | - | <0.01 | <0.01 | <0.01 | <0.01 |
| **Al-Si-Sr** | Balance | 8.78 | - | 0.02 | <0.01 | <0.01 | <0.01 |
| **Al-Si-Ce** | Balance | 7.62 | 1.17 | <0.01 | <0.01 | <0.01 | <0.01 |
| **Al-Si-Ce-Sr** | Balance | 7.4 | 1.07 | 0.03 | <0.01 | <0.01 | <0.01 |

### 3.3.2. X-Ray Diffraction (XRD)

The unmodified and modified Al-Si alloys and master alloys were analysed by XRD at Poly Crystallography Inc. (Naperville, USA) using a Bruker D2 Phaser diffractometer equipped with a LynxEye position-sensitive detector. The metal samples were mounted in a deep sample holder using modelling clay. The x-ray powder patterns were measured from 5° to 130° in steps of 0.0202144° at scan speed of 0.5 s per step, using a 0.6-mm divergence slit with 2.5° Soller slits and a 3-mm scatter screen height.

### 3.3.3. Microstructural Analysis

Metallographic samples for microstructural analysis were prepared from the cast cylinders by grinding and mechanical polishing. Etching was performed using a mixture of 20% hydrochloric acid (conc. 37%) and 80% isopropyl alcohol to reveal the fibrous or lamellar structure of the Si eutectic. The analysis was carried out by means of optical microscopy and on a Zeiss-Sigma field emission gun-scanning electron microscope (FEG-SEM). Quantitative dimensional analysis of the Si phase was performed by analysing five images, acquired by SEM at x5k, using ImageJ 1.50i software. Chemical analysis was performed using energy-dispersive spectroscopy (EDS). The electron backscatter diffraction (EBSD) capability of the same SEM was also used to elucidate the grain misorientations in primary and eutectic Al.

### 3.3.4. Thermal Analysis

The progress of solidification in the four samples was analysed by examining their respective cooling curves. Approximately 15 g of each sample were placed in a clay graphite crucible and melted at 750 °C in an electrical resistance furnace. Once molten, the crucible was taken out and a K-type thermocouple was immediately inserted below the surface of the melt. The cooling curve was collected using a data logger recording at 10 Hz. Under these conditions, a cooling rate of 1.2 ± 0.2 °C/s was observed. The measurement was repeated to ensure repeatability.

### 3.3.5. Differential Scanning Calorimetry (DSC)

Thermal analysis by means of DSC was conducted on the prepared alloys, using a Netzsch STA 449 F3 Jupiter to determine the phase changes taking place. These experiments were conducted in inert argon (Ar) atmosphere at heating and cooling rate of 10 K/min repeating the melting-solidification cycle for three times. Due to the overlapping peaks of the eutectic and primary Al, the peaks were plotted using OriginPro® 2016 (64-bit) b9.3.226 and bi-Guassian multiple peak fit analysis was carried out to obtain the eutectic onset temperature.

## 3.4. Results and Discussion

### 3.4.1. X-Ray Diffraction Analysis

Figure 3.1 presents the XRD spectra of the four alloys under investigation and the master alloys from which they were produced. The peaks of interest in each spectrum are indicated with an asterisk, except in Al-Si where the Al and Si peaks are differentiated using an asterisk and a circle, respectively. Figure 3.1a, b and c shows the spectra for Al-Si, Al-Sr and Al-Si-Sr. The spectrum for Al-Si-Sr is identical to that for Al-Si, thus yielding no information with respect to whether $Al_4Sr$ is still present in the alloy or whether a ternary intermetallic phase formed. However, previously published research demonstrated that Al-Si-Sr ternary intermetallic particles form in this specific alloy and constitute 0.03 % by volume of the alloy[17]. The lack of a peak for this component in figure 3.1c is due to the extremely small amount of Sr added in this alloy.

Figure 3.1d, e, and f presents the XRD spectra for Al-Ce, Al-Si-Ce and Al-Si-Ce-Sr. The dominant phase in Al-Ce was $Al_{11}Ce_3$, changing to $Al_2Si_2Ce$ when Al-Ce was added to Al-Si. Previous research has indicated that $Al_2Si_2Ce$ is a metastable phase and that the thermodynamically favoured phase at similar compositions would be $AlSi_2Ce$[18]. However, the XRD results seem to indicate that under these casting conditions the metastable $Al_2Si_2Ce$ forms.

When compared with the Sr addition in Al-Si-Sr, the amount of Ce addition in Al-Si-Ce and Al-Si-Ce-Sr is much greater, thus the amount of intermetallics formed is also significantly increased. The spectra for Al-Si-Ce and Al-Si-Ce-Sr are identical, indicating that XRD is unable to identify the presence of any new particles formed or changes to the $Al_2Si_2Ce$ due to the Sr addition.

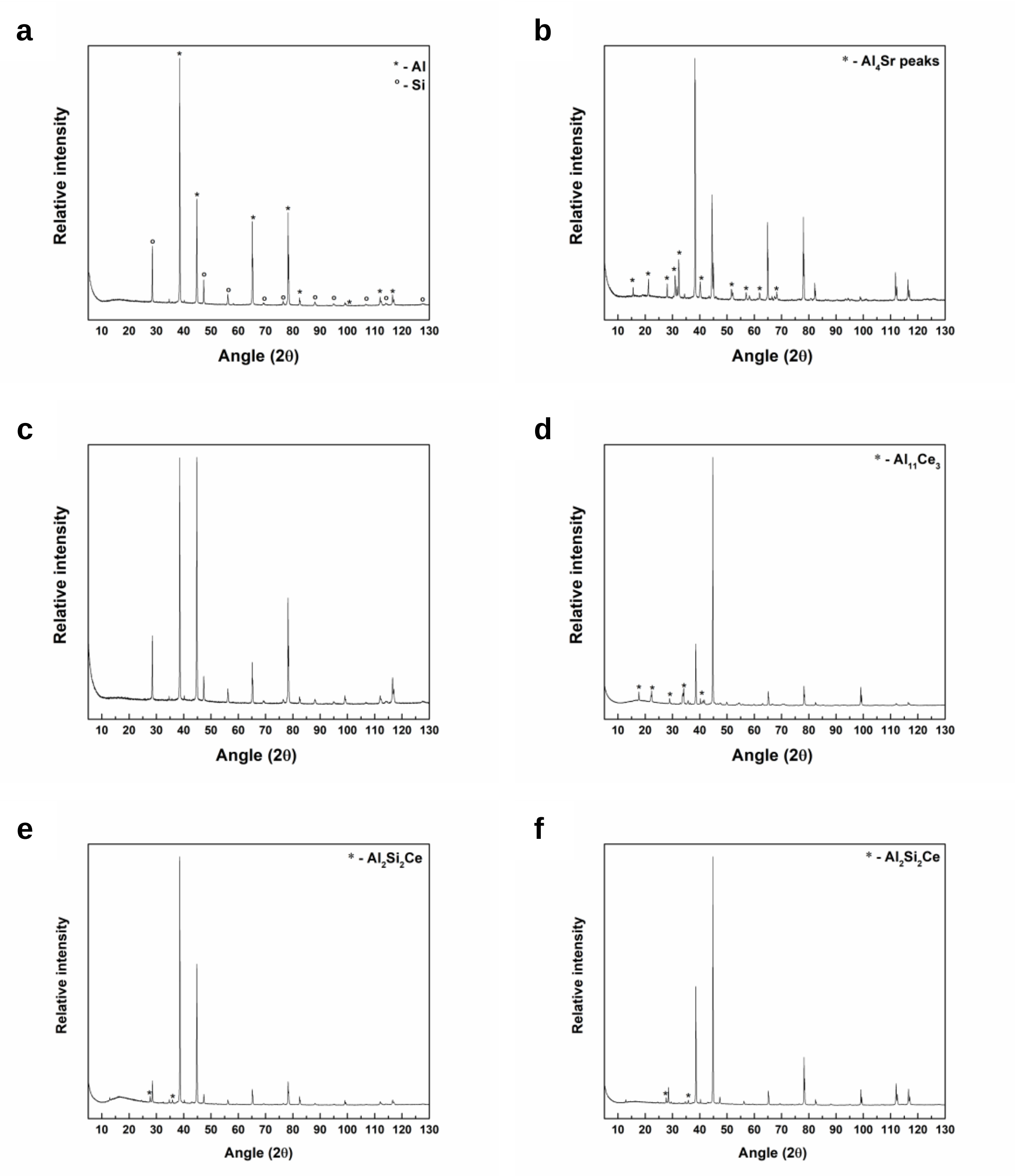

Figure 3.1: XRD spectra of (a) Al-Si, (b) Al-Sr, (c) Al-Si-Sr, (d) Al-Ce, (e) Al-Si-Ce, and (f) Al-Si-Ce-Sr.

### 3.4.2. Microstructural Characterisation

Figure 3.2a, d, g, and j shows the optical microscopy images of the unmodified and modified alloys. In figure 3.2a, the unmodified alloy shows primary Al and eutectic Si in the form of elongated plates, whilst figure 3.2d shows the Sr modified alloy where addition of Sr resulted in modification of the eutectic Si to a fine fibrous structure. Figure 3.2g shows that addition of 1% Ce caused refinement of the eutectic Si compared with the unmodified condition. The combined effect of Ce and Sr is shown in figure 3.2j, where the eutectic Si closely approaches full modification to a fine fibrous structure, though some longer Si features can be observed. In the alloys containing Ce, large block-like features, indicated by an arrow, can also be noted. These are Ce-containing intermetallics which form in the alloy.

Figure 3.2 also shows SEM images of the polished (b, e, h, k) and etched (c, f, i, l) alloy samples. The images obtained from the polished samples can be considered as a high magnification version of the optical images. Note that the Si in the Al-Si (b) alloy is present in a flake-like structure, whilst the Al-Si-Sr (e) and Al-Si-Ce-Sr (k) show very similar microstructures, i.e. a fine fibrous one. On the other hand, the Al-Si-Ce (h) sample shows a partially modified microstructure, as both flake-like and fibre-like Si can be observed. The etched samples provide further understanding on the microstructural modification by imaging the Si at subsurface level. The Si flake-like structure of Al-Si is confirmed in figure 3.2c. The fine fibrous Si microstructure in Al-Si-Sr and Al-Si-Ce-Sr can also be seen in figure 3.2f and l respectively. These images indicate an almost identical Si morphology in both of these alloys. Further insight is provided for Al-Si-Ce in figure 3.2l which shows a central flake-like feature in the shape of an "X" surrounded by fibres. This confirms that 1% Ce only partially modified the Si phase, as observed in previous studies[4,9,10].

The modification effect in the different alloys was analysed quantitatively, in terms of the Feret diameter and circularity by analysing five SEM images. It must be clarified that this quantitative analysis was performed on a two-dimensional (2D) cross-section and thus yields information regarding the apparent size and shape of the Si eutectic in this plane. The Feret diameter is defined as the longest distance between any two points along the selection boundary[19]. The circularity is defined as $4\pi * \frac{Area}{Perimeter^2}$, where a value of 1 indicates a perfect circle, with decreasing values indicating less circular features[19]. Alloys presenting shorter and more circular Si features, can be considered to have achieved a higher degree of modification. The results of this analysis are presented as histograms in figure 3.3. Figure 3.3a shows the Feret diameter distribution of the Si features across the whole range, while the inset zooms in on the region from 0 µm to 2 µm region. Figure 3.3b shows the circularity distribution of the Si phase. Tabulated data are also shown as insets to these figures.

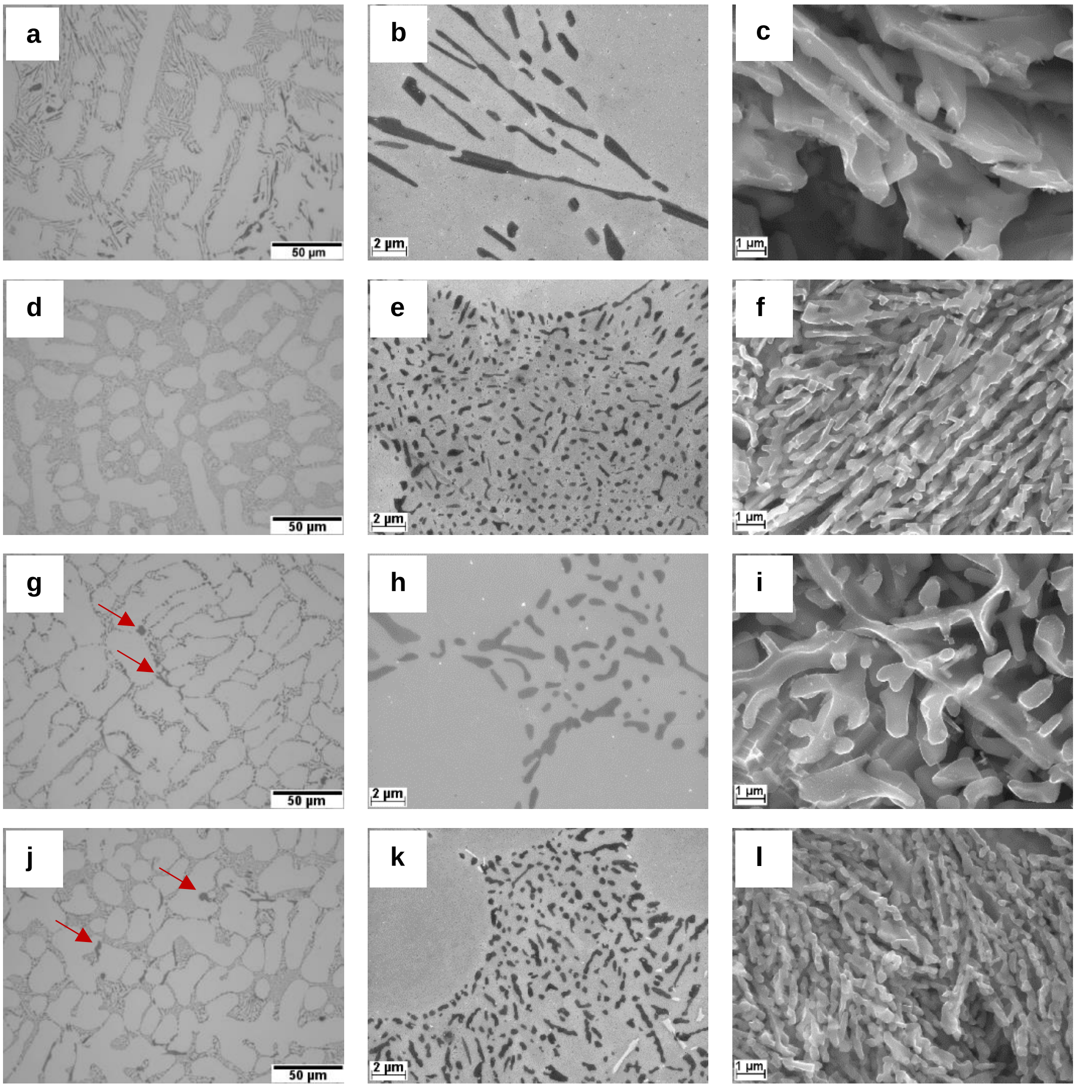

Figure 3.2: Optical microscopy images (a, d, g, j) and scanning electron microscopy images on unetched (b, e, h, k) and etched (c, f, i, l) samples of Al-Si (a, b, c), Al-Si-Sr (d, e, f), Al-Si-Ce (g, h, i) and Al-Si-Ce-Sr (j, k ,l).

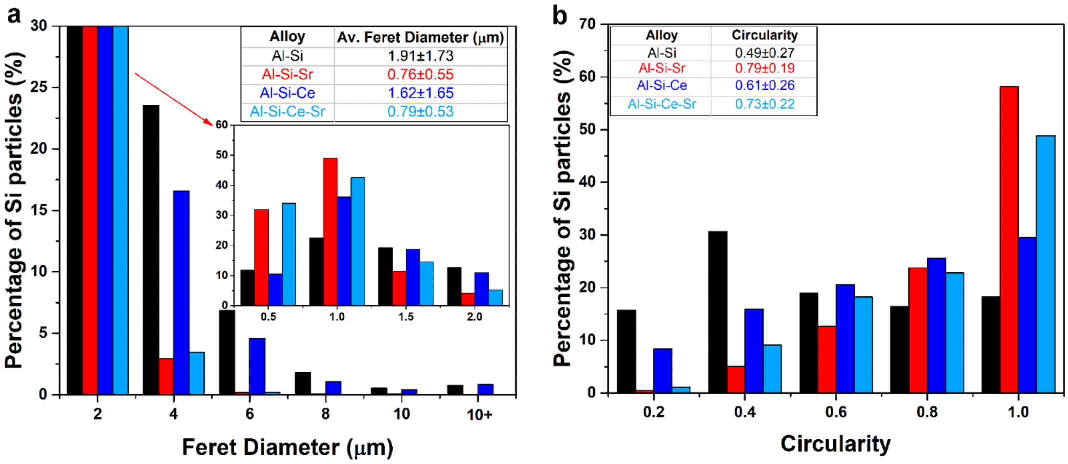

| Alloy | Av. Feret Diameter (μm) |
|---|---|
| Al-Si | 1.91±1.73 |
| Al-Si-Sr | 0.76±0.55 |
| Al-Si-Ce | 1.62±1.65 |
| Al-Si-Ce-Sr | 0.79±0.53 |

| Alloy | Circularity |
|---|---|
| Al-Si | 0.49±0.27 |
| Al-Si-Sr | 0.79±0.19 |
| Al-Si-Ce | 0.61±0.26 |
| Al-Si-Ce-Sr | 0.73±0.22 |

Figure 3.3: (a) Size distribution analysis of the Si phase comparing Al-Si, Al-Si-Sr, Al-Si-Ce and Al-Si-Ce-Sr, (b) shape distribution analysis for the same alloys. The table inserts show average values and standard deviation for the alloys.

Figure 3.3, shows a distinct trend between the two alloys that contain Sr and the two alloys that do not. Al-Si-Sr and Al-Si-Ce-Sr both present Si features with markedly smaller average Feret diameter and higher average circularity, indicating that a significantly higher degree of modification was achieved. Al-Si showed slightly longer and significantly less circular Si features compared with Al-Si-Ce, indicating that addition of 1% Ce partially modified the Si within the microstructure. On the other hand, the two Sr-containing alloys presented similarly sized and shaped Si. A slight difference in the circularity of these alloys can be observed in figure 3.3b. Al-Si-Ce-Sr seemed to show a slightly higher percentage of features with lower circularity (<0.8), compared with Al-Si-Sr. Though only marginal, this could be further confirmation of the observations made based on the optical microstructures, i.e., the presence of longer features in Al-Si-Ce-Sr compared with Al-Si-Sr.

### 3.4.3. Thermal Analysis

Figure 3.4b shows the eutectic region of the cooling curves, for each of the four different alloy compositions. The complete cooling curves are provided in figure 3.4a. The nucleation temperature ($T_N$), minimum temperature ($T_{MIN}$), growth temperature ($T_G$), and recalescence ($T_G$ - $T_{MIN}$) were measured. The eutectic $T_N$ is the point at which Si crystals start to nucleate. It can be extracted from the cooling curves by plotting the derivative of the curve and reading out where the tangents of the two slopes meet. Figure 3.4c shows how the data was extracted from the cooling curves. $T_{MIN}$ is the point where the eutectic Si and Al have grown to a stage where the latent heat evolved during the growth process balances the heat flow out of the system. $T_{MIN}$ leads to recalescence which takes place when the release of latent heat exceeds the heat extraction from the system. This results in a new heat balance which is denoted as $T_G$[20]. These results show that addition of 1% Ce extended the mushy zone as the primary growth temperature increased whilst the eutectic arrest temperature decreased. This allows for further growth of primary Al.

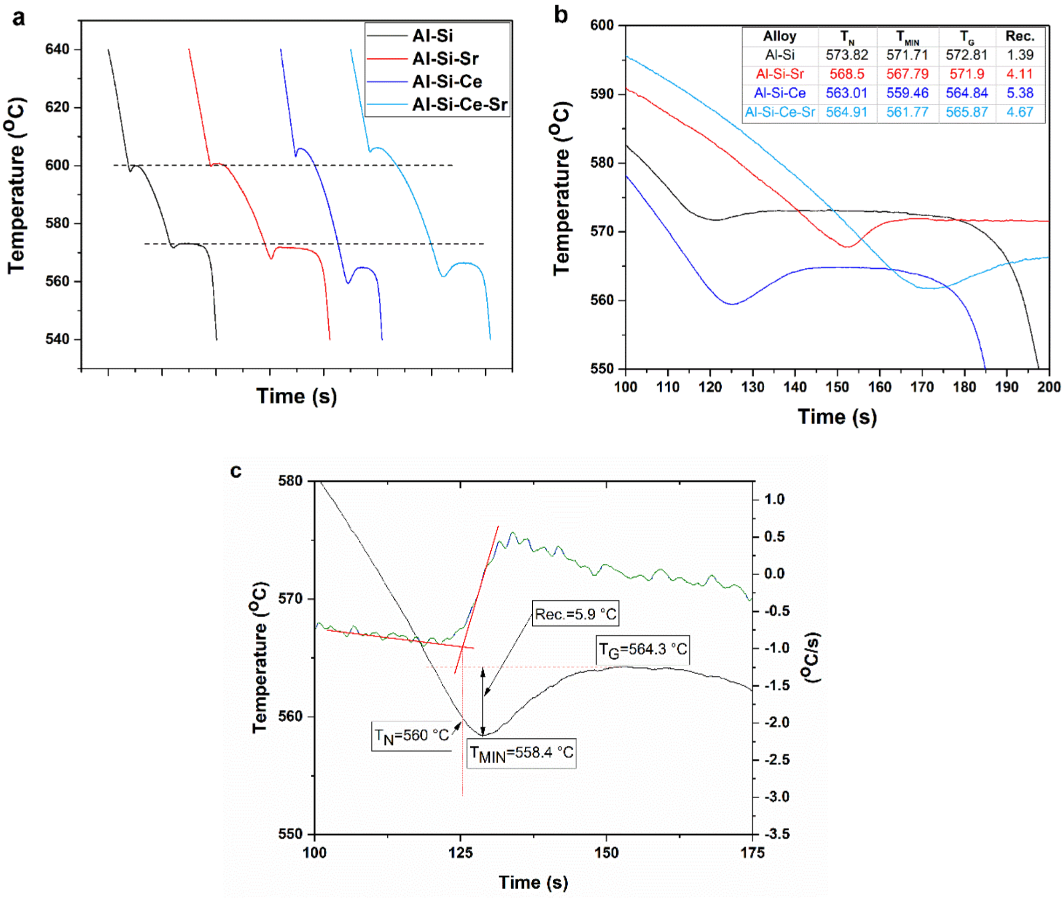

| Alloy | $T_N$ | $T_{MIN}$ | $T_G$ | Rec. |
|---|---|---|---|---|
| Al-Si | 573.82 | 571.71 | 572.81 | 1.39 |
| Al-Si-Sr | 568.5 | 567.79 | 571.9 | 4.11 |
| Al-Si-Ce | 563.01 | 559.46 | 564.84 | 5.38 |
| Al-Si-Ce-Sr | 564.91 | 561.77 | 565.87 | 4.67 |

Figure 3.4: (a, b) Comparison of cooling curves of Al-Si, Al-Si-Sr, Al-Si-Ce and Al-Si-Ce-Sr. (a) shows the entire cooling curve whilst (b) zooms in on the eutectic transition. (c) Method used to extract data from cooling curves.

The primary growth temperature is increased by approximately 5 °C upon adding 1% Ce. The master alloy addition resulted in a decrease in silicon content from 8.8 wt% to 7.5 wt%. An Al-Si binary phase diagram shows that such a decrease in Si content yields results in an increase of the liquidus temperature of approximately 8°C.

Furthermore, the addition of 1% Ce to an Al-8wt%Si reduces the liquidus temperature by approximately 3℃., as shown in the phase diagram in figure 3.5 These compositional differences explain the increase in the primary growth temperature.

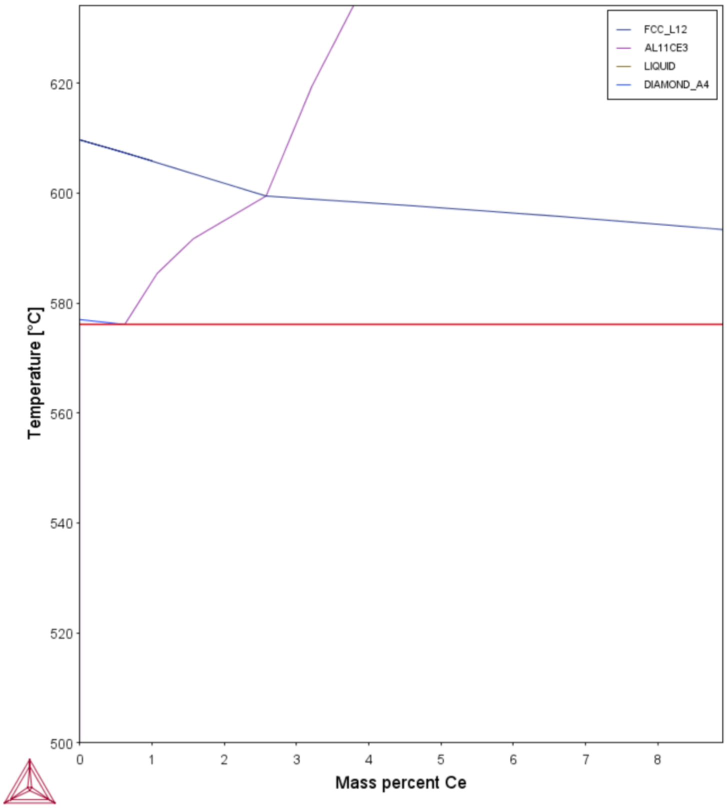

Figure 3.5: Al-8wt%Si phase diagram showing reduction in liquidus temperature with increased Ce addition

The eutectic nucleation decreased by 5 °C upon adding 400 ppm Sr. Upon adding 1% Ce, the nucleation temperature was depressed by a further 5 °C whereas upon addition of both Ce and Sr, the nucleation temperature increased by about 2 °C in comparison with addition of 1% Ce only. The depression of the eutectic growth temperature is frequently regarded as an indication of the microstructural modification obtained. This is normally attributed to the aluminium phosphide (AlP) nucleation sites becoming poisoned by the modifying element, causing eutectic nucleation to occur at a lower temperature. However, in this case, note that the depression of the eutectic growth temperature does not reflect the microstructural modification obtained. This has also been observed by other authors when adding rare-earth elements to Al-Si alloys[10,20,21]. There is also a marked difference in the eutectic recalescence, which increased from 1.4 °C for unmodified Al-Si to approximately 5 °C in presence of Ce, in both Al-Si-Ce and Al-Si-Ce-Sr. The depression in the eutectic growth temperature, for all three modified alloys, seems to indicate that $Al_2Si_2X$ compounds, where X could be either Ce or Sr, deactivates any AlP from acting as nucleating sites for the eutectic. The greater extent to which the eutectic growth temperature is affected in the Ce-containing alloys may be related to their higher Ce content. The lack of nucleation sites and therefore more homogenous nucleation is shown by the smaller but nevertheless flake-like Si structure. Therefore, the decrease in eutectic growth can be related to the removal of nucleation sites and more homogenous nucleation, but not to the morphological transition to fibre-like eutectic observed in the presence of Sr. Furthermore it can be noted that supercooling ($T_G$ - $T_N$) was observed in all alloys, except the unmodified alloy. Hanna et al. showed that supercooling occurs in hypoeutectic Na-modified Al-Si alloy but not in unmodified alloy indicating that the modification affects the nucleation of eutectic Si[22]. The fact that the same effect can be seen in Al-Si alloys containing both Sr or Ce indicates that both of these elements affect the nucleation of eutectic Si.

### 3.4.4. Differential Scanning Calorimetry

DSC was primarily used to identify the temperature of formation of any intermetallic phases, since no indication of these was observed in the cooling curves. DSC was also used as a cross-check for the trends observed in the cooling curves. Figure 3.6 shows the second cooling cycle during the DSC analysis of the different samples. The inset table presents the average and standard deviation of the primary and eutectic onsets for the three cooling cycles. Note from the DSC curves that, for all the modified alloys, the primary onset occurred much earlier. This is similar to what was observed in the cooling curves, though it is more evident now, due to the slower cooling rates. The interpretation of the eutectic onset is more difficult as it overlaps with the primary onset. Bi-Guassian curve fitting was performed, and the first deviation from the baseline of the eutectic curve was extracted as the eutectic onset.

One of the first observations is that the eutectic onset for the unmodified Al-Si occurred at 587 °C rather than the well-known equilibrium eutectic temperature of

577 °C. This indicates that the curve fitting used here can only be used to correlate trends between the alloys being analysed rather than comparison with more general absolute values. Nonetheless, for all the modified samples, the eutectic onset occurred at a much lower temperature than for the unmodified sample. The Sr-modified sample exhibited a eutectic onset temperature similar to the Ce-containing samples. This contrasts with the cooling curve data, where the eutectic nucleation temperature was significantly higher for Al-Si-Sr compared with Al-Si-Ce or Al-Si-Ce-Sr. For the Ce-containing samples, an inflection occurred at the beginning of the eutectic formation, being more evident for Al-Si-Ce. This difference between the results of the two techniques can be attributed to the inflection in the curve. In fact, a comparison of the peak position shows that for the Ce-containing samples, the peak occurs at a much later stage than for Al-Si-Sr. This inflection is attributed to the formation of intermetallics in the alloy.

It was also generally observed that samples containing Sr showed lower standard deviation than the other alloys. During this analysis it was noted that minimal oxidation occurred on the Sr-containing samples which retained their shiny appearance, indicating that under these conditions a thick oxide layer did not form. On the other hand, the alloys that did not contain Sr, turned dull, indicating formation of an oxide layer. This oxide formation explains the drift from the first to third cycle and the higher standard deviation for the alloys that did not contain Sr.

A number of authors previously employed DSC to measure the undercooling in Al-Si, using melt-spun alloys. In such cases two distinct peaks formed for the eutectic formation, the first representing the solidification of eutectic Si along grain boundaries, and the second representing solidification of entrained eutectic Si within the Al matrix[23,24]. In some cases, when exploring the effect of addition of trace amounts of modification elements such as strontium and europium, detection of intermetallic compound formation was also achieved, appearing as a small peak just after the first eutectic peak[25,26]. In this study, intermetallic formation was detected just at the start of the eutectic formation. The addition of Sr to Al-Si-Ce also seems to bring the intermetallic formation forward slightly.

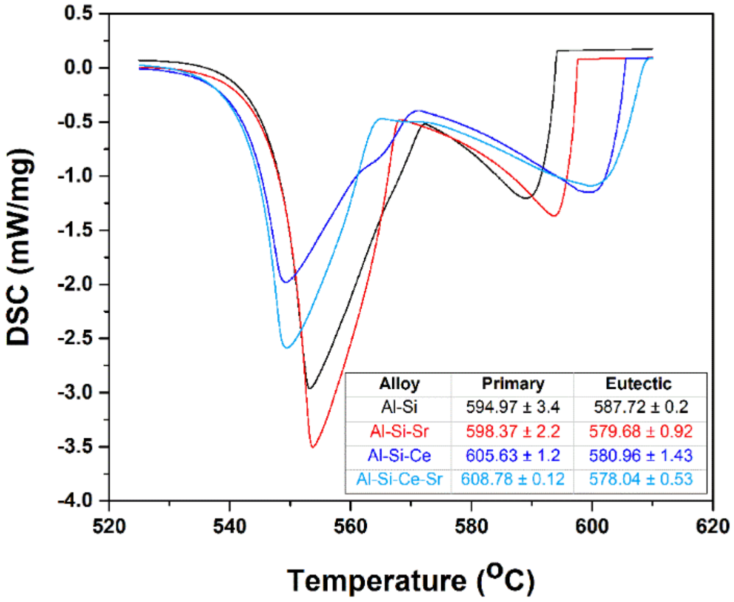

| Alloy | Primary | Eutectic |
|---|---|---|
| Al-Si | 594.97 ± 3.4 | 587.72 ± 0.2 |
| Al-Si-Sr | 598.37 ± 2.2 | 579.68 ± 0.92 |
| Al-Si-Ce | 605.63 ± 1.2 | 580.96 ± 1.43 |
| Al-Si-Ce-Sr | 608.78 ± 0.12 | 578.04 ± 0.53 |

Figure 3.6: Comparison of the second cooling cycle in DSC analysis of Al-Si, Al-Si-Sr, Al-Si-Ce and Al-Si-Ce-Sr.

### 3.4.5. Energy Dispersive Spectroscopy

EDS chemical composition maps for the Al-Si and Al-Si modified alloys were acquired and are presented in figure 3.7, clearly showing the segregation of the Al and Si in their respective phases. Furthermore, they show that, in the presence of Ce, intermetallic phases made up of all three elements formed. For Al-Si-Sr and Al-Si-Ce-Sr, the Sr map is also presented, although, its concentration within these areas was too low to be detected. The presence of $Al_2Si_2Sr$ intermetallics in Al-Si-Sr has been previously shown by EDS and quantified by x-ray computed tomography (XCT)[17].

These results show that, in such systems, ternary intermetallic compounds, in the form of $Al_2Si_2X$ form as an intrinsic part of the solidification process. Previous research has debated the formation of $Al_2Si_2Sr$ as a crucial aspect of the nucleation and subsequent modification of the eutectic Si[16,27]. The formation of $Al_2Si_2Ce$, the presence of which has been shown in section 3.3.2, and the lack of full modification in the Al-Si-Ce alloy indicate that the formation of such compounds is not a crucial factor in predicting the modification potential of an element. Some authors debated whether the formation of nanoclusters, with different shapes, of $Al_2Si_2Sr$ within eutectic Si is the contributing factor for the modification potential of Sr[28,29]. Therefore, further work, by means of transmission electron microscopy and atom probe tomography, is required to fully characterise the eutectic Si partially modified by Ce, and to explore whether such nanoclusters also form after addition of Ce.

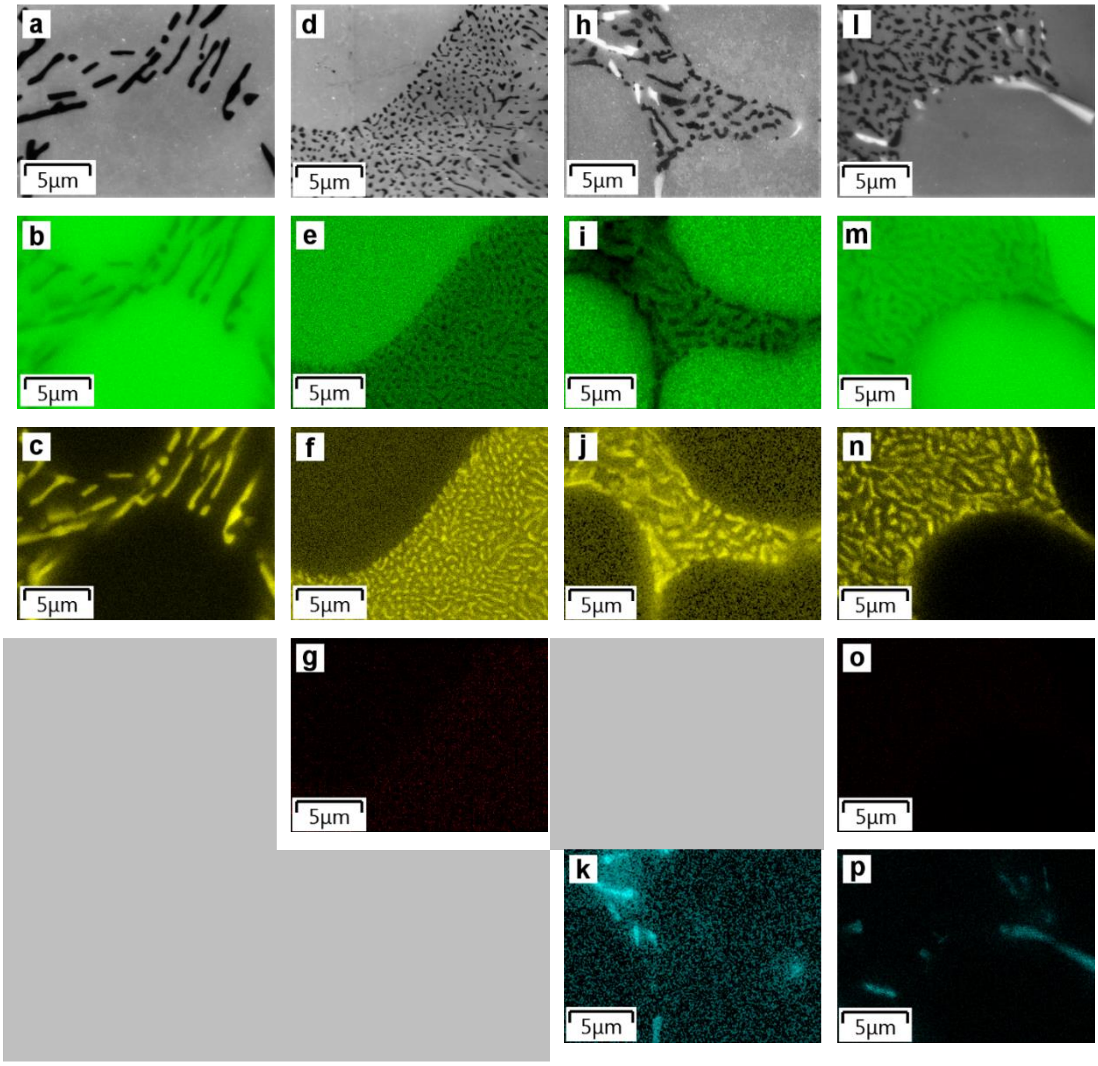

Figure 3.7: SEM images representing the (a) unmodified Al-Si, (d) Al-Si-Sr, (h) Al-Si-Ce, (l) Al-Si-Ce-Sr alloys, and the corresponding EDS elemental maps for Al (b, e, i, m), Si (c, f, j, n), Sr (g, o) and Ce (k, p).

### 3.4.6. Electron Backscatter Diffraction

Large-area EBSD misorientation maps were acquired on the four alloys and are presented in figure 3.8a, d, g and j. Different grain colours indicate misorienation greater than 5°. From these maps it can be noted that in unmodified Al-Si, the primary Al dendrite orientation extends within the eutectic Al. This indicates that the solidification of the eutectic Al occurred mainly on primary Al dendrites. There are also some areas in the Al-Si map that seem to have nucleated separately from the primary dendrite, but when comparing the Al-Si EBSD map with the Al-Si-Sr one, a stark contrast can be noted immediately. The latter shows complete separation between the primary and eutectic Al, as individual areas within the eutectic have different orientations relative to each other and relative to the primary. In the Al-Si-Ce and Al-Si-Ce-Sr alloys, though not as evident primarily due to the smaller eutectic region, a similar observation can be made.

Magnified images from different regions of each EBSD map are also provided in figure 3.8, as these provide more detailed information. Images from the Al-Si map are shown in figure 3.8b and c. Note that most of the eutectic Al region has the same orientation as the primary Al in proximity (dark green in b, bright green in c). However, there are also grains which show a misorientation from the primary Al.

EBSD has been previously employed to shed light on the solidification behaviour of Sr-modified and unmodified Al-Si alloys[14,30–33]. Most of this research explored the Al solidification. Nogita and Dahle[30] argue that if the eutectic Al nucleates on the primary Al dendrite, the orientation of the eutectic Al would be the same as that of the primary dendrite, whereas if the eutectic Al nucleates in the interdendritic liquid the orientation would be different from that of the primary Al dendrite. Their results indicated a transition from the former to latter mechanism upon modifying alloy 319 with 70 ppm Sr. Dahle et al.[14] agreed with this observation, but noted that at higher levels of Sr, the eutectic Al growth reverted back to growth in the same orientation as the primary Al dendrite whilst still achieving complete modification of the Si phase. Heiberg and Arnberg[32] noted the same mechanism when using high purity alloys modified with 150 ppm Sr. The results presented herein indicate a general trend which shows that in the presence of Ce and/or Sr the solidification of the eutectic Al occurs independently from the primary Al dendrite, as individual eutectic Al regions have different orientations with respect to the primary Al.

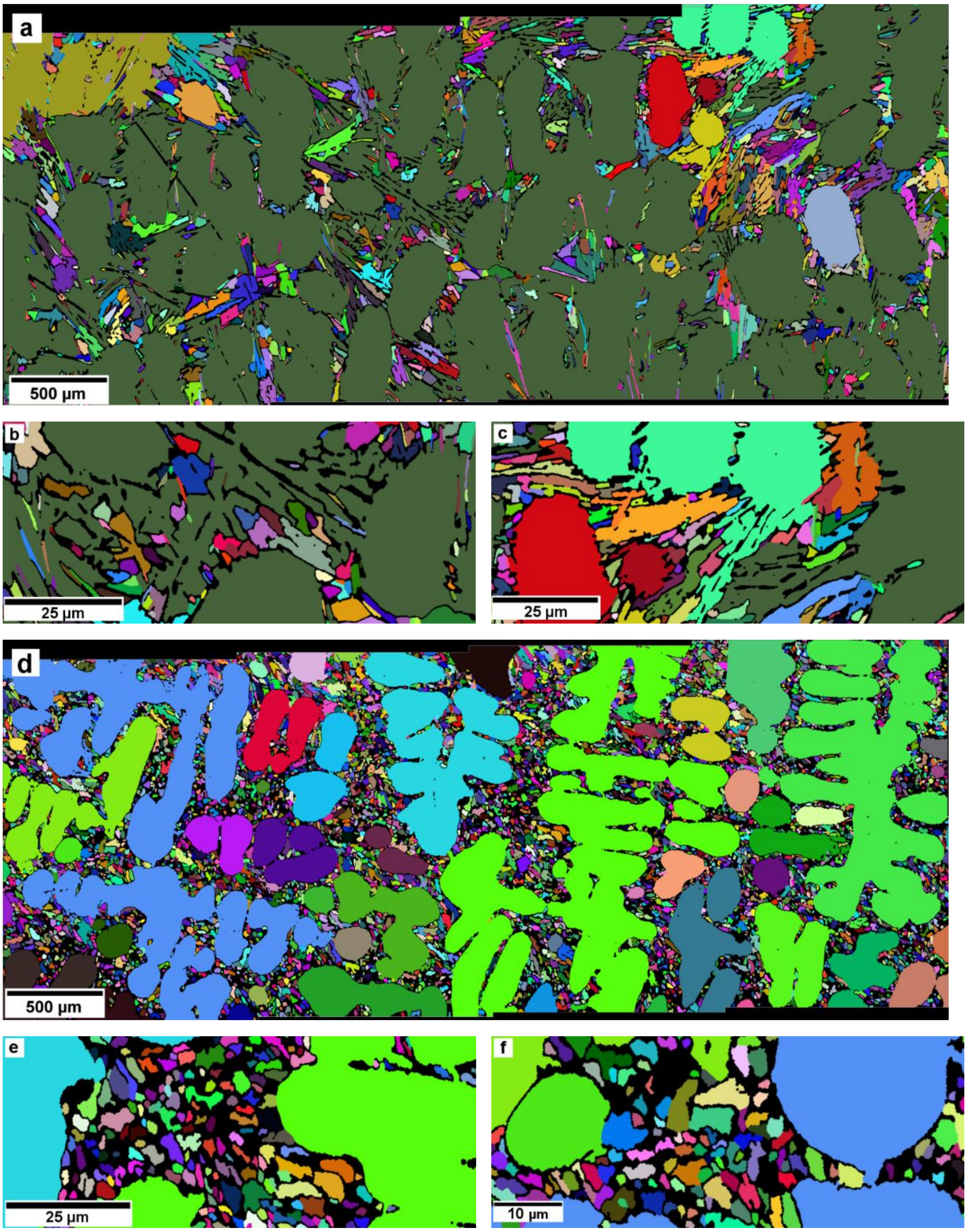
a
500 µm
b
25 µm
c
25 µm
d
500 µm
e
25 µm
f
10 µm

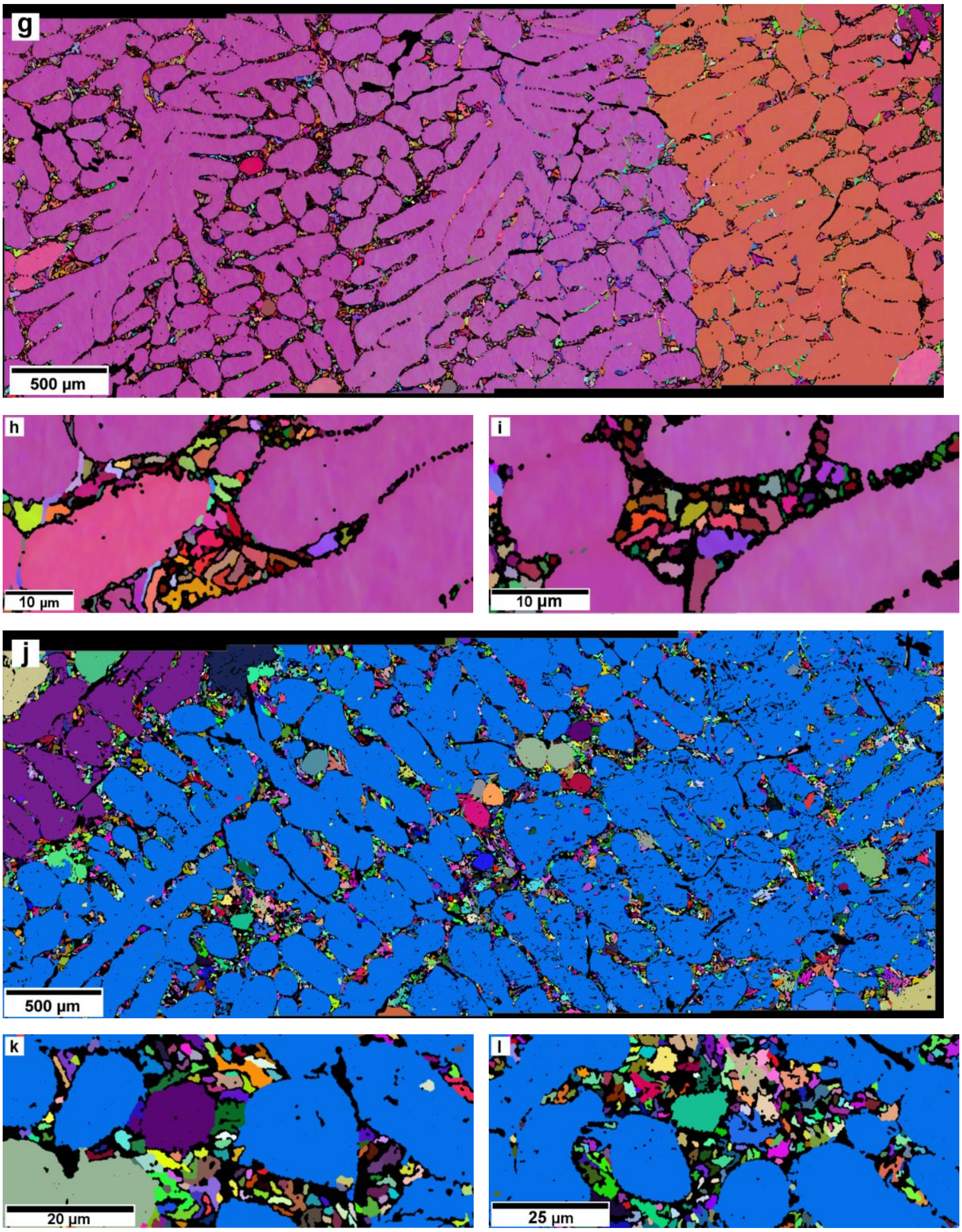

Figure 3.8: EBSD maps for (a-c) Al-Si, (d-f) Al-Si-Sr, (g-i) Al-Si-Ce and (j-l) Al-Si-Ce-Sr.

## 3.5. Conclusions

- Addition of 1% Ce caused partial modification of Al-Si. Upon addition of 0.04% Sr to Al-Si-Ce, full modification was obtained being comparable to the Sr modification employed industrially.

- Cooling curves and DSC results showed that the primary Al growth temperatures were increased in the presence of 1% Ce.
- Cooling curves and DSC results showed that the eutectic nucleation and growth temperatures were reduced. It is also noted that, in the presence of 1% Ce, the eutectic growth temperature was significantly lower than in the unmodified or Sr-modified Al-Si. Although this is normally regarded as an indication of the modification effect, microstructural examination of the Al-Si-Ce alloy showed otherwise.
- Addition of Ce caused formation of an intermetallic phase, identified as $Al_2Si_2Ce$ by means of XRD and EDS.
- EBSD indicated that in the presence of Ce and/or Sr, the solidification of the eutectic Al was completely independent of the primary Al. The fact that Ce and Sr, a partial and full modifier respectively, showed the same behaviour indicates that the solidification of the eutectic Al in relation to the primary Al is not a contributing factor to the modification of the Si eutectic phase.

## 3.6. References

1. Polmear, I. J. in *Light Alloys* 205–235 (Elsevier, 2005). doi:10.1016/B978-075066371-7/50008-6
2. Bartley, R. *British and European Aluminium Casting Alloys*. (Association of Light Alloy Refiners, 1996).
3. Hatch, J. E. *Aluminium: Properties and Physical Metallurgy*. (American Society of Metals, 1984).
4. Nogita, K., McDonald, S. D. & Dahle, A. K. Eutectic Modification of Al-Si Alloys with Rare Earth Metals. *Mater. Trans.* **45,** 323–326 (2004).
5. Ye, B. J. An assessment of the role of rare earth in the eutectic modification of cast Al-Si. *Trans. Am. Foundrymen's Soc.* **93,** 533–544 (1985).
6. Shi, Z., Wang, Q., Shi, Y., Zhao, G. & Zhang, R. Microstructure and mechanical properties of Gd-modified A356 aluminum alloys. *J. Rare Earths* **33,** 1004–1009 (2015).
7. Qiu, H., Yan, H. & Hu, Z. Effect of samarium (Sm) addition on the microstructures and mechanical properties of Al–7Si–0.7Mg alloys. *J. Alloys*

*Compd.* **567,** 77–81 (2013).

8. Tsai, Y. C. *et al.* Effect of trace La addition on the microstructures and mechanical properties of A356 (Al–7Si–0.35Mg) aluminum alloys. *J. Alloys Compd.* **487,** 157–162 (2009).
9. Vijeesh, V. & Prabhu, K. N. in *Light Metals 2015* 403–407 (John Wiley & Sons, Inc., 2015). doi:10.1002/9781119093435.ch67
10. Tsai, Y. C., Lee, S. L. & Lin, C. K. Effect of trace Ce addition on the microstructures and mechanical properties of A356 (Al–7SI–0.35 Mg) aluminum alloys. *J. Chinese Inst. Eng.* **34,** 609–616 (2011).
11. Lu, S. & Hellawell, A. Growth mechanisms of silicon in Al-Si alloys. *J. Cryst. Growth* **73,** 316–328 (1985).
12. Lu, S.-Z. S. & Hellawell, A. The mechanism of silicon modification in aluminum-silicon alloys: Impurity induced twinning. *Metall. Trans. A* **18,** 1721–1733 (1987).
13. Kobayashi, K. F. & Hogan, L. M. The crystal growth of silicon in Al-Si alloys. *J. Mater. Sci.* **20,** 1961–1975 (1985).
14. Dahle, A. K., Nogita, K., McDonald, S. D., Zindel, J. W. & Hogan, L. M. Eutectic nucleation and growth in hypoeutectic Al-Si alloys at different strontium levels. *Metall. Mater. Trans. A* **32,** 949–960 (2001).
15. Cho, Y. H., Lee, H.-C., Oh, K. H. & Dahle, A. K. Effect of Strontium and Phosphorus on Eutectic Al-Si Nucleation and Formation of β-Al5FeSi in Hypoeutectic Al-Si Foundry Alloys. *Metall. Mater. Trans. A* **39,** 2435–2448 (2008).
16. Srirangam, P. *et al.* Probing the local atomic structure of Sr-modified Al–Si alloys. *Acta Mater.* **65,** 185–193 (2014).
17. De Giovanni, M., Warnett, J. M., Williams, M. A. & Srirangam, P. 3D imaging and quantification of porosity and intermetallic particles in strontium modified Al-Si alloys. *J. Alloys Compd.* **727,** 353–361 (2017).
18. Gröbner, J., Mirković, D. & Schmid-Fetzer, R. Thermodynamic aspects of the constitution, grain refining, and solidification enthalpies of Al-Ce-Si alloys. *Metall. Mater. Trans. A* **35,** 3349–3362 (2004).
19. Ferreira, T. & Rasband, W. *ImageJ User Guide IJ 1.46r. IJ 1.46r* (2012). doi:10.1038/nmeth.2019
20. Li, J. H. & Schumacher, P. Effect of Y addition and cooling rate on

refinement of eutectic Si in Al–5 wt-%Si alloys. *Int. J. Cast Met. Res.* **25,** 347–357 (2012).

21. Mahmoud, M. G., Elgallad, E. M., Ibrahim, M. F. & Samuel, F. H. Effect of Rare Earth Metals on Porosity Formation in A356 Alloy. *Int. J. Met.* **12,** 251–265 (2018).
22. Hanna, M. D., Lu, S. & Hellawell, A. Modification in the aluminum silicon system. *Metall. Trans. A* **15,** 459–469 (1984).
23. Ho, C. R. & Cantor, B. Modification of hypoeutectic Al-Si alloys. *J. Mater. Sci.* **30,** 1912–1920 (1995).
24. Liao, C., Chen, J., Li, Y., Tu, R. & Pan, C. Morphologies of Al4Sr Intermetallic Phase and Its Modification Property upon A356 Alloys. *J. Mater. Sci. Technol.* **28,** 524–530 (2012).
25. Zarif, M., Mckay, B. & Schumacher, P. Study of Heterogeneous Nucleation of Eutectic Si in High-Purity Al-Si Alloys with Sr Addition. *Metall. Mater. Trans. A* **42,** 1684–1691 (2010).
26. Li, J. H. *et al.* Modification of eutectic Si in Al–Si alloys with Eu addition. *Acta Mater.* **84,** 153–163 (2015).
27. Barrirero, J. *et al.* Comparison of segregations formed in unmodified and Sr-modified Al–Si alloys studied by atom probe tomography and transmission electron microscopy. *J. Alloys Compd.* **611,** 410–421 (2014).
28. Barrirero, J. *et al.* Cluster formation at the Si/liquid interface in Sr and Na modified Al–Si alloys. *Scr. Mater.* **117,** 16–19 (2016).
29. Timpel, M. *et al.* Sr–Al–Si co-segregated regions in eutectic Si phase of Sr-modified Al–10Si alloy. *Ultramicroscopy* **132,** 216–221 (2013).
30. Nogita, K. & Dahle, A. . Eutectic solidification in hypoeutectic Al–Si alloys: electron backscatter diffraction analysis. *Mater. Charact.* **46,** 305–310 (2001).
31. Nogita, K., Knuutinen, A., McDonald, S. D. & Dahle, A. K. Mechanisms of eutectic solidification in Al–Si alloys modified with Ba, Ca, Y and Yb. *J. Light Met.* **1,** 219–228 (2001).
32. Heiberg, G. & Arnberg, L. Investigation of the microstructure of the Al–Si eutectic in binary aluminium–7 wt% silicon alloys by electron backscatter diffraction (EBSD). *J. Light Met.* **1,** 43–49 (2001).
33. Dahle, A. K., Nogita, K., McDonald, S. D., Dinnis, C. & Lu, L. Eutectic modification and microstructure development in Al–Si Alloys. *Mater. Sci.*

*Eng. A* **413–414,** 243–248 (2005).

# Chapter 4:

# Modification of Al-Si alloys by Y or Y with Sr

## Summary

This chapter seeks to address the first objective of this thesis, that is understanding the modification mechanism of hypoeutectic Al-Si alloys by comparing full modification and partial modification. An identical analysis to that carried out in chapter 3 was performed here but using Y to perform the partial modification instead of Ce. This is confirmatory work for the findings in chapter 3, that is there are no differences in the partial modification obtained by two different elements. Samples modified by both Y and Sr were also investigated in order to understand the synergistic effect of the two elements in the same alloy. The various solidification and microstructural studies carried out on these samples will be presented herein whilst carrying out a comparison of the different modifications achieved.

This work is currently in preparation to be submitted for publication. The same people who contributed to the publication presented in chapter 3 have contributed to the work presented in this chapter in the same roles.

*Publication in preparation:*

*Modification of Al-Si alloys by Y or Y with Sr*

## 4.1. Abstract

In this study Al-Si alloys were modified with the addition of yttrium (Y) and yttrium plus strontium (Sr) to investigate their effect on eutectic silicon morphology. To understand the effect of yttrium and strontium on the microstructure of Aluminium-Silicon (Al-Si) alloys the modified alloys were characterised using SEM microscopy, XRD, and thermal analysis. Results show that the addition of 1% Y resulted in only partial modification of the Si phase, and it was observed that addition of yttrium with 0.04% Sr resulted in complete modification of the alloy. The addition of 1% Y dropped the eutectic nucleation temperature by about 10 °C as compared to the 5 °C drop by Sr addition only. SEM-EDS and XRD results show the formation of $Al_2Si_2Y$ intermetallics when Y is added to Al-Si alloys, which is demonstrated to form just before the eutectic phase.

**Keywords:** Al-Si alloys; modification; yttrium; strontium

## 4.2. Introduction

Aluminium-Silicon (Al-Si) alloys are widely used in the automotive and aerospace industries due to their high strength to weight ratio, good castability, excellent mechanical and performance properties[1]. Typically these alloys form a coarse microstructure which is composed of large silicon flakes in a continuous aluminium matrix. These silicon flakes act as propagation planes for defects and therefore the alloys show low ductility. However, chemical modification or fast cooling can modify the coarse silicon morphology into a fine and fibrous one, thus improving the ductility and tensile strength of the alloy[1,2]. In the 1920s Pacz[3] observed the chemical modification after treating the casting with sodium fluoride and chemical modification was applied industrially using Sodium (Na). More recently, strontium has been used as the preferred chemical modifier mainly due to its higher retention in the cast alloy and no significant over-modification issues. This microstructural modification improves mechanical properties, pressure tightness, and machinability, reduces hot tear resistance and significantly raises fracture toughness[1,2,4].

Significant research has been carried out looking into the effect of various chemical elements, such as rare earths, on the modification of Al-Si alloys[5–10]. However, their addition normally only results in a refinement, or partial modification of the microstructure of Al-Si alloys. One such example is yttrium. Previous research has shown that the addition of 200 ppm Y to Al-Si alloys does not result in any modification effect[11]. However, the addition of larger amounts of Y has been shown to refine the Si microstructure and improve mechanical properties, thus obtaining increased refinement with increasing Y content[12,13].

The mechanism by which chemical modification happens has been controversial since its discovery. Theories can be split into two categories: either growth restriction-based theories, mainly impurity induced twinning (IIT)[14,15] and restricted growth theory[16] or nucleation-based theories, that focus on the formation of $Al_2Si_2Sr$ (or similar) particles that deactivate the eutectic silicon nucleation sites[17–19].

The aim of this publication is to provide a basis to study the mechanistic differences between full modification, as achieved by using Sr, as described in literature[20] and the refinement achieved by Y. This is done by quantifying the modification achieved, characterising the solidification of the alloys by thermal analysis and identifying any intermetallics formed. The synergistic effect of combining Y with Sr on the modification of eutectic silicon morphology in Al-Si hypoeutectic alloys, is also investigated.

## 4.3. Methodology

### 4.3.1. Alloy preparation

The Al-Si hypoeutectic alloy was prepared by melting 99.999% purity aluminium (NewMet, UK) and 99.999% silicon (Alfa Aeser, UK) in a clay graphite crucible using a Carbolite RHF1500 high temperature furnace. Once the alloy was molten at 750 °C the metal was stirred with a graphite rod, poured into a pre-heated clay graphite crucible and left to solidify. The cast Al-Si alloy was then used to prepare the modified alloys. The Al-Si alloy was re-melted to allow for the additions of Y and Sr metals in the form of Al-10Y (wt%) and Al-10Sr (wt%) master alloys respectively. These alloys were poured into a pre-heated cylindrical graphite mould. The master alloys were produced using a similar procedure using the same 99.999% purity aluminium with 99% purity strontium (Alfa Aeser, UK) and with 99.9% purity yttrium (Alfa Aeser, UK), respectively. The chemical compositions of the two alloys were analysed by inductively coupled plasma optical emission spectroscopy (ICP-OES) and are presented in table 4.1. The concentration of Y and Sr in the alloys was based on previous research and industrial practices[2,12,21].

Table 4.1: ICP-OES chemical composition analysis performed on the two alloys in weight percentage (wt%).

| | **Al** | **Si** | **Y** | **Sr** | **Fe** | **Cu** | **Mn** |
|---|---|---|---|---|---|---|---|
| **Al-Si-Y** | Balance | 7.75 | 1.09 | <0.01 | <0.01 | <0.01 | <0.01 |
| **Al-Si-Y-Sr** | Balance | 7.39 | 0.83 | 0.03 | <0.01 | <0.01 | <0.01 |

### 4.3.2. Microstructural analysis

Metallographic samples were prepared from the cast cylinders for microstructural analysis by grinding and mechanical polishing. Etching was performed using a 20% hydrochloric acid (conc. 37%) and 80% isopropyl alcohol mixture, in order to reveal the fibrous or lamellar structure of the Si eutectic. The analysis was carried out by means of optical microscopy and on a Zeiss-Sigma field emission gun-scanning electron microscope (FEG-SEM). A quantitative dimensional analysis of the Si phase was performed by analysing five images, acquired by means of SEM at x5k, in ImageJ 1.50i. Chemical analysis was performed using energy dispersive spectroscopy (EDS). The electron backscatter diffraction (EBSD) capability on the same SEM was also used to elucidate the grain misorientations between primary and eutectic Al.

### 4.3.3. X-Ray Diffraction (XRD)

The two modified Al-Si alloys and master alloys have been analysed by XRD at Poly Crystallography Inc. (Naperville, USA). The equipment used was a Bruker D2

Phaser diffractometer equipped with a LynxEye position-sensitive detector. The metal samples were mounted in a deep sample holder with modelling clay. The x-ray powder patterns were measured from 5° to 130° at 0.0202144° steps, scanning for 0.5 seconds at each step. A 0.6 mm divergence slit with 2.5° Soller slits and a 3 mm scatter screen height was used.

### 4.3.4. Thermal Analysis

The progression of solidification of the two samples was analysed by examining their respective cooling curves. Approximately 15 g of each sample were placed in a clay graphite crucible and melted at 750 °C in an electrical resistance furnace. Once molten the crucible was taken out and immediately a K-type thermocouple was inserted below the surface of the melt. The cooling curve was collected using a data logger recording at 10 Hz. Under these conditions a cooling rate of 1.2 ± 0.2 °C/s was observed. The measurement was repeated to ensure repeatability.

### 4.3.5. Differential scanning calorimetry (DSC)

Thermal analysis by means of a DSC was conducted on the alloys prepared, using a Netzsch STA 449 F3 Jupiter, in order to determine the phase changes taking place in these alloys. The experiments were conducted in an inert Argon (Ar) atmosphere. A heating and cooling rate of 10 K/min was used and the melting – solidification cycle was repeated three times. Due to the overlapping peaks of the eutectic and primary the peaks were plotted in OriginPro® 2016 (64-bit) b9.3.226 and a biguassian multiple peak fit analysis was carried out to obtain the eutectic onset temperature.

## 4.4. Results and Discussion

### 4.4.1. Microstructural Characterisation

Optical microscopy images of the two alloys are shown in figure 4.1. It can be noted that Al-Si-Y (figure 4.1 a) presents significantly coarser silicon in comparison to Al-

Si-Y-Sr (figure 4.1 b). These images also show the presence of large intermetallic features (marked with arrows).

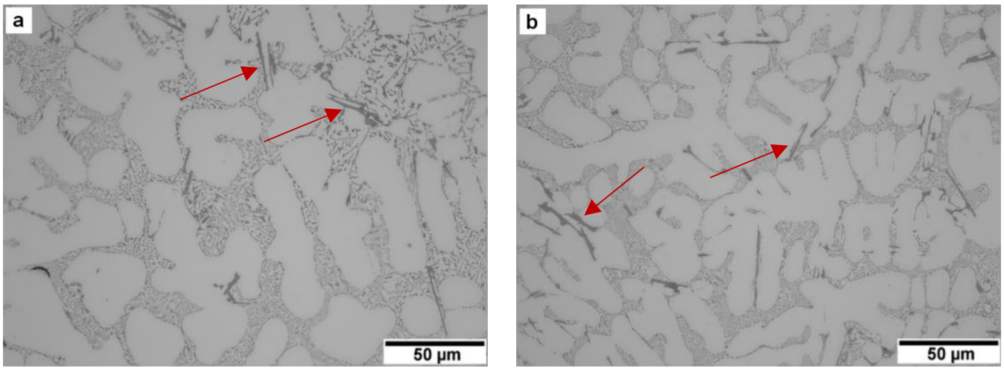

Figure 4.1: Optical microscopy images of (a) Al-Si-Y and (b) Al-Si-Y-Sr

Figure 4.2 shows SEM images of the polished (a, c) and etched (b, d) alloy samples. The images obtained from the polished samples can be considered as a high magnification image of the optical images. It can be noted that the Si in the Al-Si-Y (figure 4.2 a) alloy is present mostly in a flake-like structure, which is considered partially modified when compared to the known Al-Si microstructure[20]. The alloy also presents some circular features which could potentially be modified. On the other hand, the Al-Si-Y-Sr (figure 4.2 c) presents a fine fibrous structure which approaches the morphology obtained by full modification[20], though some flake-like features can still be observed. The etched samples further help to understand the microstructural modification by imaging the Si at sub-surface level. In the Al-Si-Y alloy, the silicon flake-like structure is confirmed in figure 4.2 (b). This confirms that 1% Y only partially modified the Si phase, as observed in previous studies[12,13]. A fine fibrous microstructure can be observed in most of the Al-Si-Y-Sr alloy (figure 4.2 d), though some flake-like features can once again be noted, confirming that the modification approaches full modification. These flake-like features are marked with arrows in figure 4.2 (d).

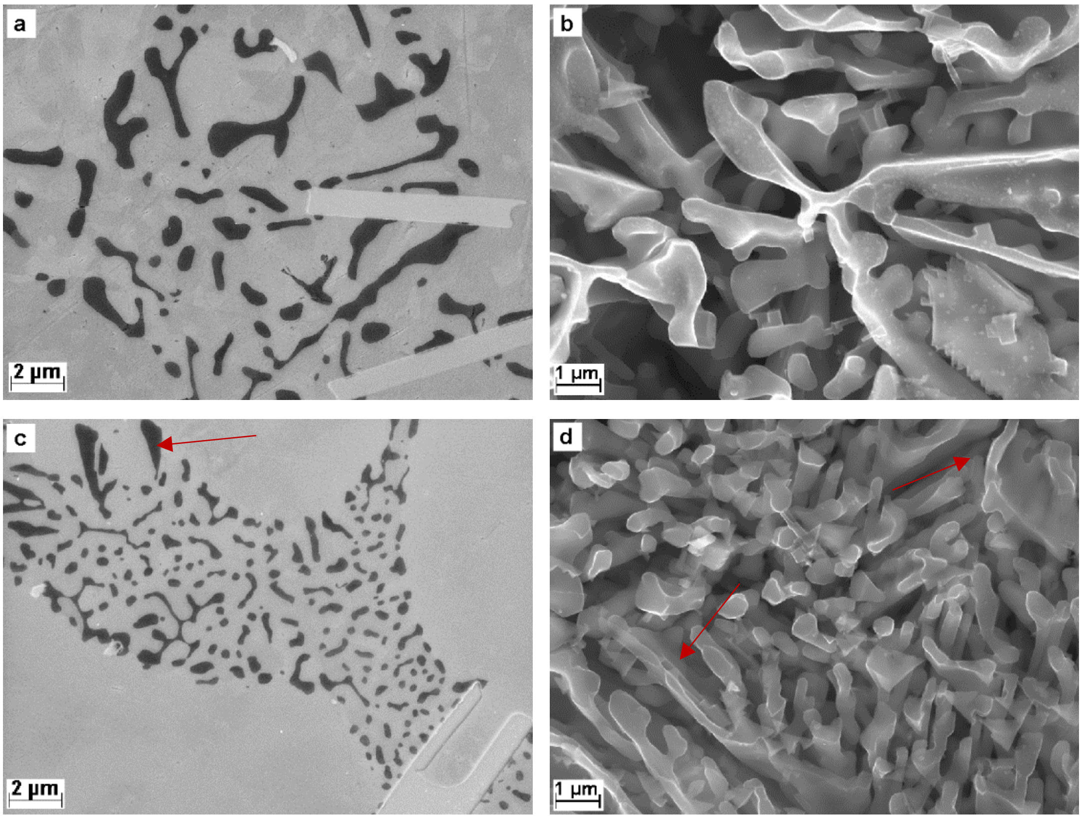

Figure 4.2: scanning electron microscopy images on unetched (a, c) and etched (b, d) samples of Al-Si-Y (a, b) and Al-Si-Y-Sr (c, d).

The modification effect within the different alloys was analysed quantitatively, in terms of Feret diameter and circularity, by analysing five SEM images. It must be clarified that the quantitative analysis performed is on a 2D cross-section and thus yields information regarding the apparent size and shape of the Si eutectic in this plane. Feret diameter is defined as the longest distance between any two points along the selection boundary[22]. Circularity is defined by $4\pi * \frac{Area}{Perimeter^2}$, where a value of 1 indicates a perfect circle, with decreasing values indicating a less circular feature[22]. Alloys presenting shorter and more circular Si features, can be considered to have achieved a higher degree of modification. Histograms presenting this analysis are shown in figure 4.3. Figure 4.3 (a) shows the Feret diameter distribution of the Si features across the whole range, and the insert zooms in on the 0 – 2 µm region. Figure 4.3 (b) shows the circularity distribution of the Si phase. Tabulated data is also shown as inserts in these figures.

Figure 4.3 shows a size analysis comparison for a standard Al-Si alloy, a conventionally Sr-modified Al-Si alloy (both presented in chapter 3), Al-Si-Y and Al-Si-Y-Sr. A progression can be observed where the Si phase becomes smaller and more circular in the following order: Al-Si → Al-Si-Y → Al-Si-Y-Sr → Al-Si-Sr. Al-Si shows slightly longer and significantly less circular Si features when compared to Al-Si-Y, indicating that the presence of 1% Y partially modifies the Si within the microstructure. The Al-Si-Y-Sr has significantly smaller and more circular Si features when compared to Al-Si-Y. Finally, Al-Si-Sr presents the smallest and most circular Si features in the microstructure. Difference between the two Sr-containing alloys can be observed as Al-Si-Y-Sr shows a significant amount of Si feature with a Feret diameter up to 6 µm and a circularity of 0.2. These results seem to indicate that, contrary to what was observed for Ce, the presence of Y might have a detrimental effect on the modification efficiency of Sr[20].

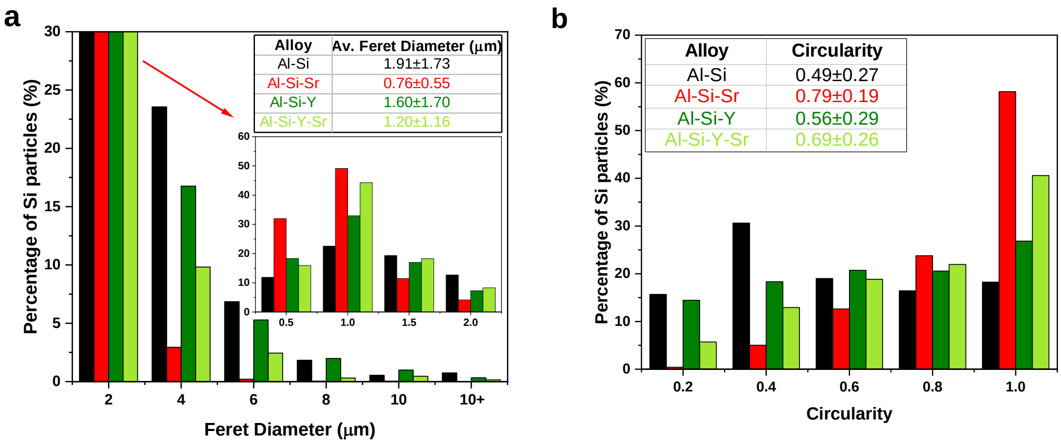

Figure 4.3: (a) Size distribution analysis of the Si phase comparing Al-Si, Al-Si-Sr, Al-Si-Y and Al-Si-Y-Sr, (b) shape distribution analysis for the same alloys. The table inserts show average values and standard deviation for the alloys.

### 4.4.2. X-Ray Diffraction (XRD)

Figure 4.4 presents the XRD spectra of the two alloys under investigation and the master alloy from which they were produced. Figure 4.4 (a) shows the Al-Y master alloy spectrum. $Al_3Y$ was identified in this alloy in the form of two phases, rhombohedral and hexagonal. These are differentiated with a * and $^o$ respectively in the spectrum.

In Al-Si-Y and Al-Si-Y-Sr, a third phase, $Al_2Si_2Y$ was identified, indicating that $Al_3Y$ changes to $Al_2Si_2Y$ when Al-Y is added to Al-Si. The $Al_2Si_2Y$ phase peaks are identified with a *. The Al-Si-Y and Al-Si-Y-Sr spectra are identical, showing that XRD is unable to identify the presence of any new particles formed or changes to the $Al_2Si_2Y$ due to the Sr addition. It is known that at such low Sr additions, it can be very challenging to identify Al-Si-Sr in Al-Si[20]. Therefore, the result here indicates that the XRD is unable to detect any new particles formed or changes to the Al-Si-Y intermetallics and that the bulk of the intermetallics formed are still $Al_2Si_2Y$. A similar observation was made on Al-Si-Ce and Al-Si-Ce-Sr[20].

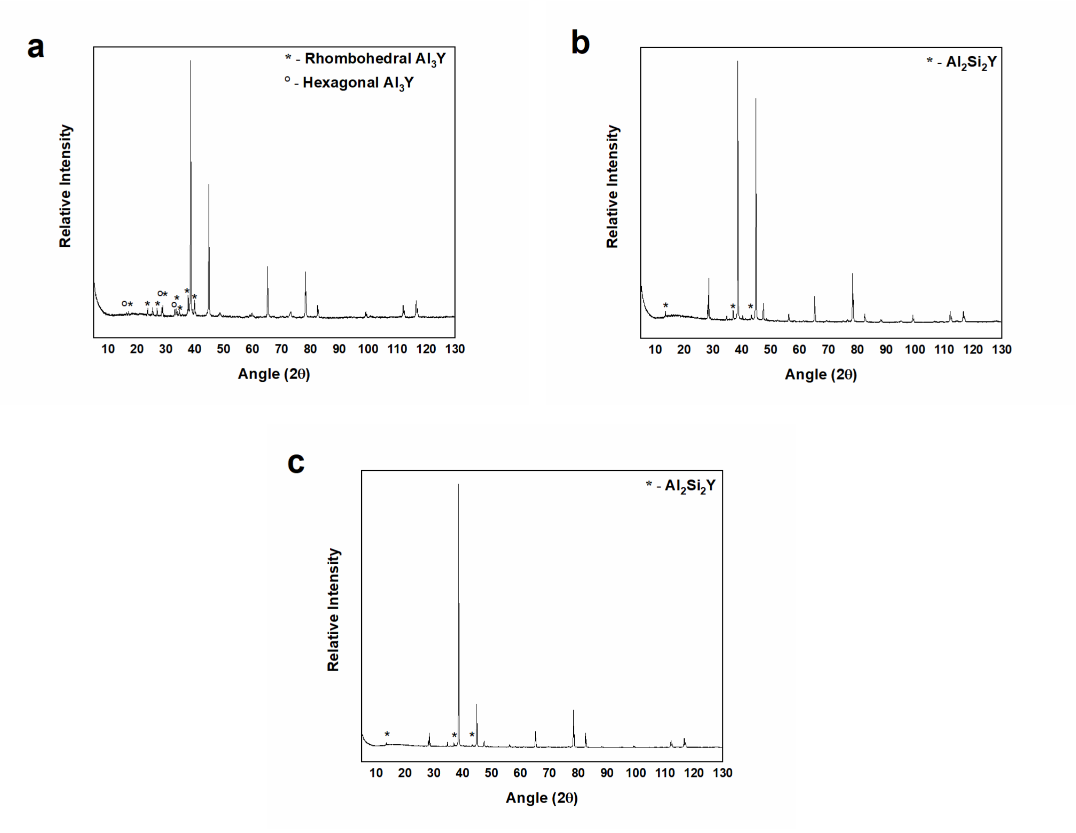

Figure 4.4: XRD spectra of (a) Al-Y, (b) Al-Si-Y and (c) Al-Si-Y-Sr.

The formation of $Al_2Si_2Y$ contrasts with Li and Schumacher who identified $Al_2SiY$ in an Al-Si-Y alloy, by means of transmission electron microscopy-energy dispersive spectroscopy (TEM-EDS)[11]. However, the addition in this alloy was limited to a trace amount (200 ppm) which could explain the different intermetallic formation.

### 4.4.3. Energy Dispersive Spectroscopy (EDS)

Figure 4.5 presents the EDS chemical composition maps for Al-Si-Y and Al-Si-Y-Sr alloys. As expected, these maps clearly show the segregation of the Al and Si in their respective phases whilst the Y appears to segregate in a ternary intermetallic phase, as indicated from XRD results. Previous atom probe tomography (APT) work showed that Y also deposits within the Si phase and forms a boundary layer around eutectic Si, however EDS is unable to detect the low concentrations at which this was detected[23]. For the Al-Si-Y-Sr alloy, the map showing presence of Sr has also been presented, however, the concentration of Sr within this area is too low to be detected by EDS, as also previously demonstrated in Al-Si-Sr and Al-Si-Ce-Sr[20]. The presence of $Al_2Si_2Sr$ intermetallics in Al-Si-Sr has been previously shown by EDS and quantified by x-ray computed tomography (XCT)[24].

These results show that in such systems ternary intermetallic compounds, in the form of $Al_2Si_2X$, form as an intrinsic part of the solidification process. Previous research has debated the formation of $Al_2Si_2Sr$ as a crucial aspect of the nucleation and subsequent modification of the eutectic Si[19,25]. The formation of $Al_2Si_2Y$ and the lack of full modification in the Al-Si-Y alloy indicate that the formation of such compounds is not a crucial factor in predicting the modification potential of an element. Some authors have debated that the formation of nanoclusters, in different shapes, of $Al_2Si_2Sr$ within the eutectic Si is the contributing factor to the modification potential of Sr[26,27]. Therefore, further work, by means of transmission electron microscopy and atom probe tomography, is required to fully characterise the eutectic Si partially modified by Y, and to explore whether such nanoclusters also form after addition of Y.

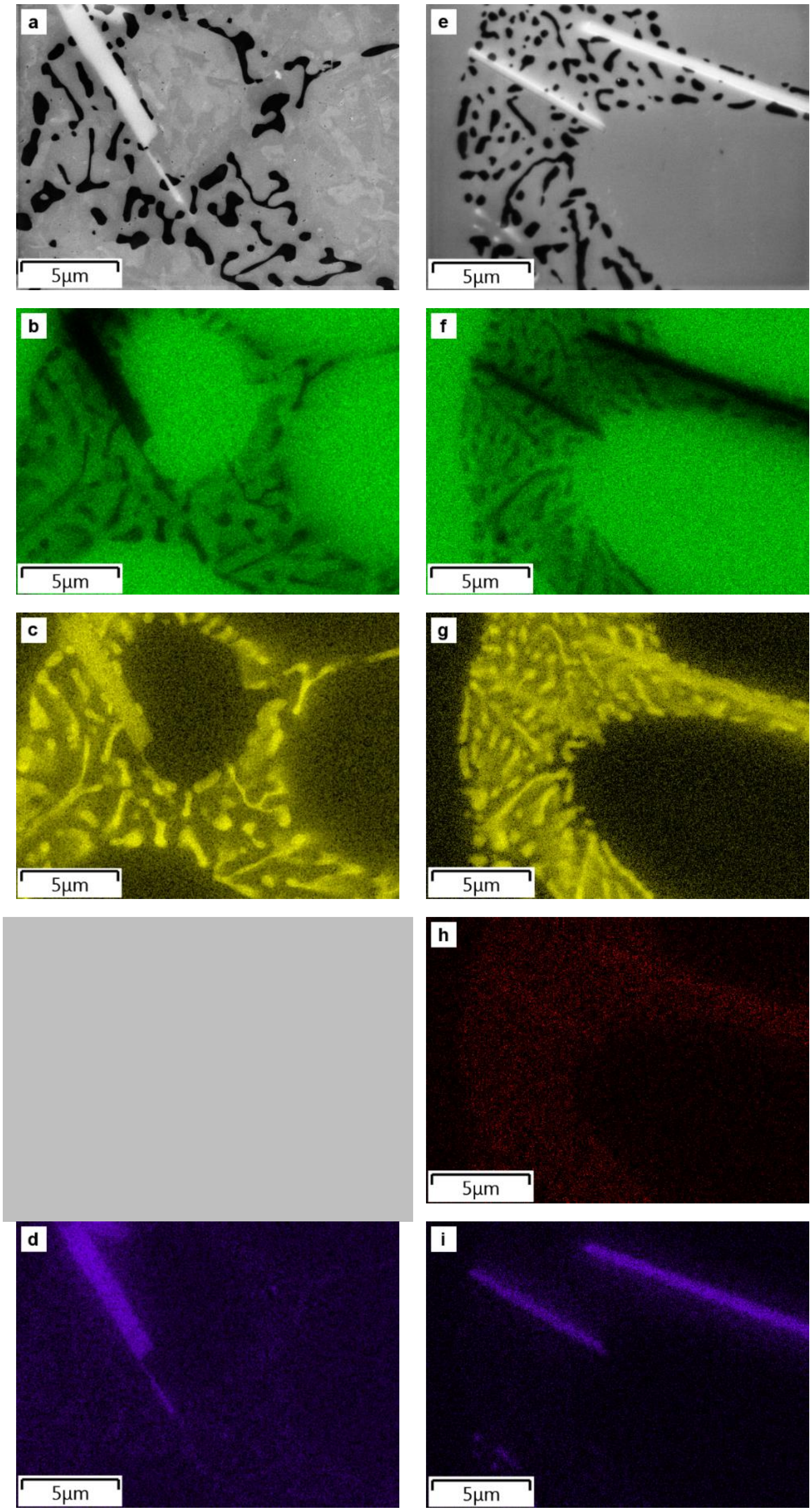

Figure 4.5: SEM images representing the (a) Al-Si-Y, (e) Al-Si-Y-Sr alloys, and the corresponding EDS elemental maps for Al (b, f), Si (c, g), Sr (h) and Y (d, i).

### 4.4.4. Thermal Analysis

Figure 4.6 shows the cooling curves for Al-Si-Y and Al-Si-Y-Sr, and compares them with previously published data for unmodified and Sr-modified Al-Si alloys[20]. Figure 4.6 (b) focuses on the eutectic region of these cooling curves and presents critical points in the eutectic transition: namely the nucleation temperature ($T_N$), minimum temperature ($T_{MIN}$), growth temperature ($T_G$) and recalescence ($T_G$ - $T_{MIN}$). The eutectic $T_N$ is the point at which the Si crystals start to nucleate and is extracted from the cooling curves by plotting the derivative of the curve and reading out where two slope tangents meet. The $T_{MIN}$ is the point where the eutectic Si and Al have grown to a stage where the latent heat evolved during the growth process balances the heat flow out of the system. $T_{MIN}$ leads to recalescence which takes place when the release of latent heat exceeds the heat extraction from the system. This results in a new heat balance which is denoted as $T_G$[11]. The results show that the addition of 1% Y, similarly to what was observed for the addition of Ce[20], extends the mushy zone as the primary growth temperature is increased whilst the eutectic arrest temperature decreases. This allows for further growth of primary Al. The primary growth temperature following Y addition shows a similar behaviour to that reported in chapter 3:. It is therefore believed that a similar combination of factors cause this shift. The eutectic nucleation decreases by 5 °C upon adding 400 ppm Sr. Upon adding 1% Y the nucleation temperature is depressed by a further 4 °C, with no variation when 400 ppm Sr are added. The eutectic growth temperature is only slightly depressed when 400 ppm Sr are added to Al-Si alloy, however it decreases by 5 °C when 1% Y is added. The depression of the eutectic growth temperature is frequently regarded as an indication of the microstructural modification obtained. This is normally attributed to the aluminium phosphide (AlP) nucleation sites becoming poisoned by the modifying element and causing the eutectic nucleation to occur at a lower temperature. However, in this case it can be noted that the depression of the eutectic growth temperature does not reflect the microstructural modification obtained. This was also observed by other authors when adding rare earth elements to Al-Si alloys[11,28,29]. There is also a marked difference in the eutectic recalescence in the presence of Y, as this is increased from 1.4 °C for unmodified Al-Si to over 4 °C in the presence of Y, both in Al-Si-Y and Al-Si-Y-Sr. The depletion in the eutectic growth temperature, in all three modified alloys, seems to indicate the $Al_2Si_2X$ compounds, where X could be either Y or Sr, deactivates any AlP from acting as a nucleating site for the eutectic. The higher extent to which the eutectic growth temperature is effected in the Y-containing alloys could be possibly related to the higher content of Y in the alloy when compared to the Sr addition in Al-Si-Sr. The lack of nucleation sites and therefore a more homogenous nucleation is shown by smaller but nevertheless flake-like Si structure. Therefore the depletion in the eutectic growth can be related to the removal of the nucleation sites and a more homogenous nucleation, but not related to the morphological transition to fibre-like eutectic observed in the presence of Sr. Furthermore, it can be noted that supercooling ($T_G - T_N$) was observed in all alloys, except the unmodified alloy. Hanna et al. showed that supercooling occurs in hypoeutectic Sodium (Na)-modified Al-Si alloy, but not in unmodified alloy indicating that the modification affects the nucleation of eutectic Si[30]. The fact that the same effect can be seen in Al-Si alloys containing both Sr or Y indicates that both of these elements affect the nucleation of eutectic Si.

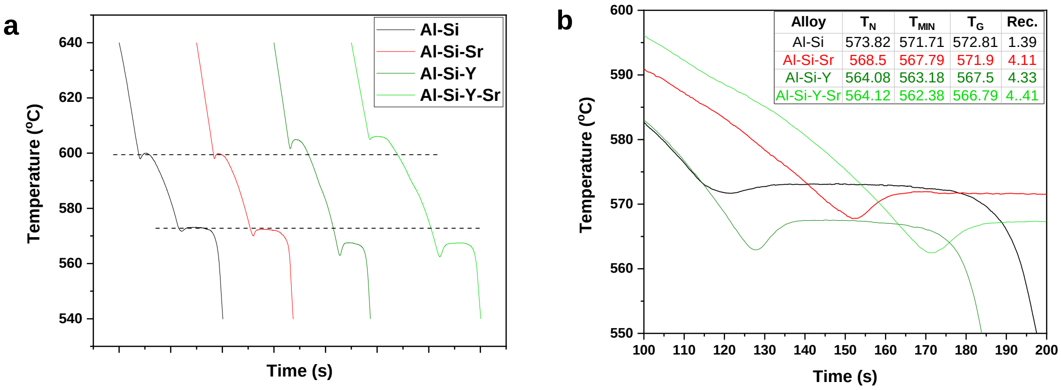

| Alloy | $T_N$ | $T_{MIN}$ | $T_G$ | Rec. |
|---|---|---|---|---|
| Al-Si | 573.82 | 571.71 | 572.81 | 1.39 |
| Al-Si-Sr | 568.5 | 567.79 | 571.9 | 4.11 |
| Al-Si-Y | 564.08 | 563.18 | 567.5 | 4.33 |
| Al-Si-Y-Sr | 564.12 | 562.38 | 566.79 | 4..41 |

Figure 4.6: Comparison of cooling curves of Al-Si, Al-Si-Sr, Al-Si-Y and Al-Si-Y-Sr. a shows the entire cooling curve whilst b zooms in on the eutectic transition.

### 4.4.5. Differential Scanning Calorimetry (DSC)

The cooling curves thermal analysis did not show any intermetallic formation and therefore DSC was used to identify the temperature at which the intermetallic forms. A cross-check for the trends observed in the cooling curves was also performed on the data obtained from the DSC. Figure 4.7 shows the second cooling cycle during the DSC analysis of Al-Si-Y and Al-Si-Y-Sr, and compares them with previously published data for unmodified and Sr-modified Al-Si alloys[20]. The plots for Al-Si and Al-Si-Sr can be split into two peaks, primary and eutectic. On the other hand a third peak is present in between the eutectic and primary peaks in the Al-Si-Y and Al-Si-Y-Sr peaks, indicating that the intermetallics form at this point. The inset table presents the average and a standard deviation for the three cooling cycles for the primary and eutectic onsets. The DSC curves show an earlier onset for the primary Al in Al-Si when compared to the other alloys. This is similar to the observations made from the cooling curves, though it is more evident now, due to the slower cooling rates in the DSC. Extracting the eutectic onset from the DSC data was more challenging as this overlaps with the primary onset. This was performed by fitting a biguassian curve function and the first deviation from the base-line of the eutectic curve was extracted as the eutectic onset.

This data should only be used as correlation between the alloys under analysis rather than more general absolute values. This is demonstrated by the eutectic onset for the unmodified Al-Si happening at 587 °C rather than the well-known equilibrium eutectic temperature of 577 °C. Nonetheless in all modified samples, the eutectic onset happens at a much lower temperature than in the unmodified sample, which follows the trend from the cooling curves in figure 4.6. The Sr-modified sample has a similar eutectic onset temperature to the Al-Si-Y alloy, which contrasts with the cooling curve data, where eutectic nucleation temperature was significantly higher for Al-Si-Sr when compared to Al-Si-Y. On the other hand the Al-Si-Y-Sr presents a eutectic onset temperature that is markedly lower than Al-Si-Sr and Al-Si-Y. It can be noted that the intermetallic peak in Al-Si-Y happens slightly closer to the eutectic than in Al-Si-Y-Sr and thus would have a greater influence on the curve fitting exercise to determine the eutectic onset temperature. This could possibly explain the discrepancy between Al-Si-Y and Al-Si-Y-Sr which was not observed in the cooling curves.

A number of authors previously employed DSC to measure the undercooling in Al-Si using melt-spun alloys. In such cases two distinct peaks form for the eutectic formation: the first which represents the solidification of eutectic Si along the grain boundary, whilst the second peak represents the solidification of entrained eutectic Si within the Al matrix[31,32]. In some cases exploring the effect of the addition trace amounts of modification elements such as strontium and europium, the detection of intermetallic compound formation was also achieved, this appearing as a small peak just after the first eutectic peak[33,34]. In this study the intermetallic formation was detected just at the start of the eutectic formation. The addition of Sr to Al-Si-Y also seems to bring forward slightly the intermetallic formation, an effect which was also observed when Sr was added to Al-Si-Ce[20].

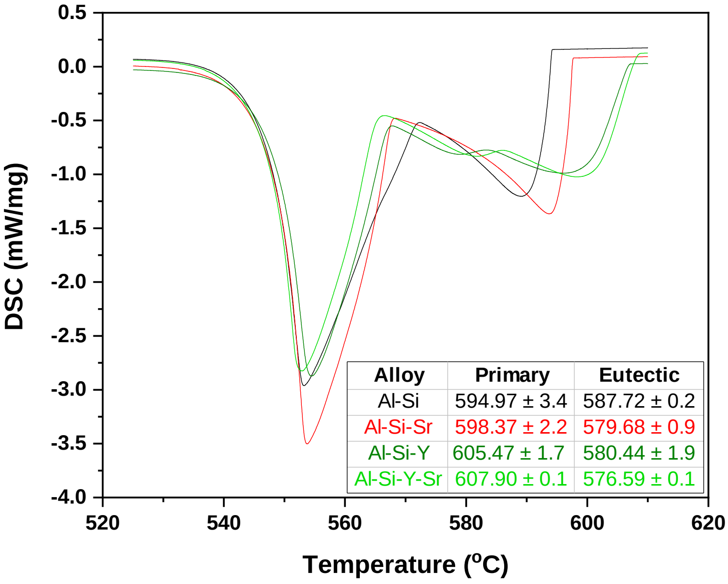

| Alloy | Primary | Eutectic |
|---|---|---|
| Al-Si | 594.97 ± 3.4 | 587.72 ± 0.2 |
| Al-Si-Sr | 598.37 ± 2.2 | 579.68 ± 0.9 |
| Al-Si-Y | 605.47 ± 1.7 | 580.44 ± 1.9 |
| Al-Si-Y-Sr | 607.90 ± 0.1 | 576.59 ± 0.1 |

Figure 4.7: Comparison of the second cooling cycle in DSC analysis of Al-Si, Al-Si-Sr, Al-Si-Y and Al-Si-Y-Sr.

### 4.4.6. Electron Backscatter Diffraction (EBSD)

EBSD misorientation maps were acquired on Al-Si-Y and Al-Sr-Y-Sr alloys and are presented in figure 4.8 (a and d). A different grain colour indicates a misorienation greater than 5°. It is known that in unmodified Al-Si the primary Al dendrite orientation extends within the eutectic Al which indicates that the solidification of the eutectic Al occurred mainly on the primary Al dendrites[20]. The eutectic Al in Sr-modified Al-Si, on the other hand, has been observed to solidify separately from the eutectic[20]. In Al-Si-Y the solidification pattern seems to approach that of unmodified Al-Si as most of the eutectic Al seems to share the same orientation as the primary Al, though some degree of misorientation can be observed. In Al-Si-Y-Sr the solidification of the Al appears similar to Sr-modified Al-Si as the eutectic regions are misorientated relative to the primary Al dendrite.

Magnified images of different regions from each EBSD map are provided in figure 4.8, providing more detailed information. Images from the Al-Si-Y map are shown in figure 4.8 (b and c). It can be noted that most of the eutectic Al region has the same orientation as the primary Al in proximity, though some degree of misorientation can be observed within some areas around the boundary of the eutectic. This contrasts with the observations recorded by Nogita et al, who detected a significant misorientation in the eutectic following the addition of 700 – 5200 ppm Y to A356.0 alloy[35]. In the Al-Si-Y-Sr alloy (figure 4.8 e and f) the grain misorientation within the eutectic is significantly more evident.

EBSD has been previously employed to shed light on the solidification behaviour of Sr-modified and unmodified Al-Si alloys[17,35–38]. Most of this research has explored the Al solidification. Nogita and Dahle[36] argue that if the eutectic Al nucleates on the primary Al dendrite, the orientation of the eutectic Al would be the same as that of the primary dendrite, whereas if the eutectic Al nucleates in the interdendritic liquid the orientation would be different from that of the primary Al dendrite. Their results indicate a transition from the former to the latter mechanism upon modifying alloy 319 with 70 ppm Sr. Dahle et al.[17] agreed with this observation but noted that at higher levels of Sr, the eutectic Al growth reverted back to growth in the same orientation of the primary Al dendrite whilst still achieving complete modification of the Si phase. Heiberg and Arnberg[37] observed the same mechanism when using high purity alloys modified with 150 ppm Sr. The results presented here show that upon addition of Y the eutectic Al solidifies together with the primary Al whilst when Sr is added to Al-Si-Y the solidification of the eutectic Al occurs independently from the primary Al dendrite. In this latter case individual eutectic Al regions have different orientations with respect to the primary Al.

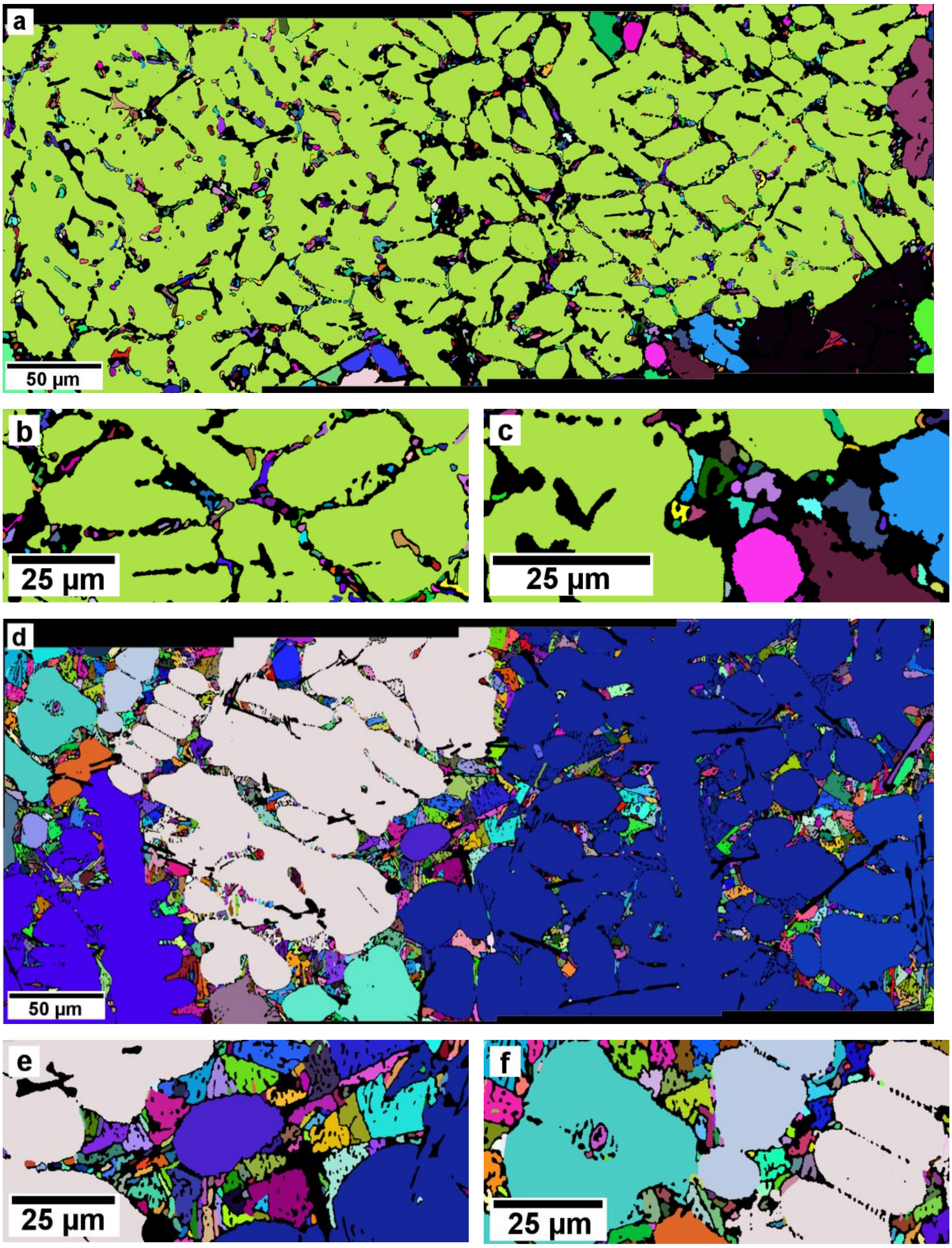

Figure 4.8: EBSD maps for (a-c) Al-Si-Y and (d-f) Al-Si-Y-Sr.

## 4.5. Conclusion

- The addition of 1% Y causes a partial modification of the eutectic Si in Al-Si. Upon addition of 0.04% Sr to Al-Si-Y full modification is obtained which is comparable to the industrially employed Sr modification.

- Cooling curves and DSC have shown that the primary Al growth temperatures are increased in the presence of 1% Y.
- Cooling curves and DSC have shown that the eutectic nucleation and growth temperatures are reduced. It is also noted that in the presence of 1% Y the eutectic growth temperature is significantly lower than in the unmodified and the Sr-modified Al-Si alloys. This shows that using eutectic arrest temperature depression as an indication of modification efficiency can be inaccurate.
- Addition of Y causes the formation of an intermetallic phase which has been identified as $Al_2Si_2Y$ by means of XRD and EDS.
- EBSD indicates that in Al-Si-Y the eutectic Al solidifies together with the primary Al, whilst upon addition of Sr the solidification of the eutectic Al becomes independent from the primary Al.

## 4.6. References

1. Polmear, I. J. in *Light Alloys* 205–235 (Elsevier, 2005). doi:10.1016/B978-075066371-7/50008-6
2. Bartley, R. *British and European Aluminium Casting Alloys*. (Association of Light Alloy Refiners, 1996).
3. Pacz, A. Alloy. (1921). at <http://www.google.com/patents/US1387900>
4. Hatch, J. E. *Aluminium: Properties and Physical Metallurgy*. (American Society of Metals, 1984).
5. Nogita, K., McDonald, S. D. & Dahle, A. K. Eutectic Modification of Al-Si Alloys with Rare Earth Metals. *Mater. Trans.* **45,** 323–326 (2004).
6. Ye, B. J. An assessment of the role of rare earth in the eutectic modification of cast Al-Si. *Trans. Am. Foundrymen's Soc.* **93,** 533–544 (1985).
7. Shi, Z., Wang, Q., Shi, Y., Zhao, G. & Zhang, R. Microstructure and mechanical properties of Gd-modified A356 aluminum alloys. *J. Rare Earths* **33,** 1004–1009 (2015).
8. Qiu, H., Yan, H. & Hu, Z. Effect of samarium (Sm) addition on the microstructures and mechanical properties of Al–7Si–0.7Mg alloys. *J. Alloys Compd.* **567,** 77–81 (2013).

9. Tsai, Y. C. *et al.* Effect of trace La addition on the microstructures and mechanical properties of A356 (Al–7Si–0.35Mg) aluminum alloys. *J. Alloys Compd.* **487,** 157–162 (2009).
10. Vijeesh, V. & Prabhu, K. N. in *Light Metals 2015* 403–407 (John Wiley & Sons, Inc., 2015). doi:10.1002/9781119093435.ch67
11. Li, J. H. & Schumacher, P. Effect of Y addition and cooling rate on refinement of eutectic Si in Al–5 wt-%Si alloys. *Int. J. Cast Met. Res.* **25,** 347–357 (2012).
12. Knuutinen, A., Nogita, K., McDonald, S. D. & Dahle, A. K. Modification of Al–Si alloys with Ba, Ca, Y and Yb. *J. Light Met.* **1,** 229–240 (2001).
13. Li, B., Wang, H., Jie, J. & Wei, Z. Effects of yttrium and heat treatment on the microstructure and tensile properties of Al–7.5Si–0.5Mg alloy. *Mater. Des.* **32,** 1617–1622 (2011).
14. Lu, S. & Hellawell, A. Growth mechanisms of silicon in Al-Si alloys. *J. Cryst. Growth* **73,** 316–328 (1985).
15. Lu, S.-Z. S. & Hellawell, A. The mechanism of silicon modification in aluminum-silicon alloys: Impurity induced twinning. *Metall. Trans. A* **18,** 1721–1733 (1987).
16. Kobayashi, K. F. & Hogan, L. M. The crystal growth of silicon in Al-Si alloys. *J. Mater. Sci.* **20,** 1961–1975 (1985).
17. Dahle, A. K., Nogita, K., McDonald, S. D., Zindel, J. W. & Hogan, L. M. Eutectic nucleation and growth in hypoeutectic Al-Si alloys at different strontium levels. *Metall. Mater. Trans. A* **32,** 949–960 (2001).
18. Cho, Y. H., Lee, H.-C., Oh, K. H. & Dahle, A. K. Effect of Strontium and Phosphorus on Eutectic Al-Si Nucleation and Formation of β-Al5FeSi in Hypoeutectic Al-Si Foundry Alloys. *Metall. Mater. Trans. A* **39,** 2435–2448 (2008).
19. Srirangam, P. *et al.* Probing the local atomic structure of Sr-modified Al–Si alloys. *Acta Mater.* **65,** 185–193 (2014).
20. De Giovanni, M., Kaduk, J. A. & Srirangam, P. Modification of Al-Si Alloys by Ce or Ce with Sr. *JOM* 1–9 (2018). doi:10.1007/s11837-018-3192-6
21. Hua, G., Ahmadi, H., Nouri, M. & Li, D. Positive effect of yttrium on the reduction of pores in cast Al alloy. *Mater. Chem. Phys.* **149–150,** 140–144 (2015).

22. Ferreira, T. & Rasband, W. *ImageJ User Guide IJ 1.46r*. *IJ 1.46r* (2012). doi:10.1038/nmeth.2019

23. De-Giovanni, M., Alam, T., Banerjee, R. & Srirangam, P. 3D Atom Probe Tomography Study on Segregation of Yttrium in Modified Al-Si Alloys. *JOM* **70,** 1765–1770 (2018).

24. De Giovanni, M., Warnett, J. M., Williams, M. A. & Srirangam, P. 3D imaging and quantification of porosity and intermetallic particles in strontium modified Al-Si alloys. *J. Alloys Compd.* **727,** 353–361 (2017).

25. Barrirero, J. *et al.* Comparison of segregations formed in unmodified and Sr-modified Al–Si alloys studied by atom probe tomography and transmission electron microscopy. *J. Alloys Compd.* **611,** 410–421 (2014).

26. Barrirero, J. *et al.* Cluster formation at the Si/liquid interface in Sr and Na modified Al–Si alloys. *Scr. Mater.* **117,** 16–19 (2016).

27. Timpel, M. *et al.* Sr–Al–Si co-segregated regions in eutectic Si phase of Sr-modified Al–10Si alloy. *Ultramicroscopy* **132,** 216–221 (2013).

28. Tsai, Y. C., Lee, S. L. & Lin, C. K. Effect of trace Ce addition on the microstructures and mechanical properties of A356 (Al–7SI–0.35 Mg) aluminum alloys. *J. Chinese Inst. Eng.* **34,** 609–616 (2011).

29. Mahmoud, M. G., Elgallad, E. M., Ibrahim, M. F. & Samuel, F. H. Effect of Rare Earth Metals on Porosity Formation in A356 Alloy. *Int. J. Met.* **12,** 251–265 (2018).

30. Hanna, M. D., Lu, S. & Hellawell, A. Modification in the aluminum silicon system. *Metall. Trans. A* **15,** 459–469 (1984).

31. Ho, C. R. & Cantor, B. Modification of hypoeutectic Al-Si alloys. *J. Mater. Sci.* **30,** 1912–1920 (1995).

32. Liao, C., Chen, J., Li, Y., Tu, R. & Pan, C. Morphologies of Al4Sr Intermetallic Phase and Its Modification Property upon A356 Alloys. *J. Mater. Sci. Technol.* **28,** 524–530 (2012).

33. Zarif, M., Mckay, B. & Schumacher, P. Study of Heterogeneous Nucleation of Eutectic Si in High-Purity Al-Si Alloys with Sr Addition. *Metall. Mater. Trans. A* **42,** 1684–1691 (2010).

34. Li, J. H. *et al.* Modification of eutectic Si in Al–Si alloys with Eu addition. *Acta Mater.* **84,** 153–163 (2015).

35. Nogita, K., Knuutinen, A., McDonald, S. D. & Dahle, A. K. Mechanisms of

eutectic solidification in Al–Si alloys modified with Ba, Ca, Y and Yb. *J. Light Met.* **1,** 219–228 (2001).

36. Nogita, K. & Dahle, A. K. Eutectic solidification in hypoeutectic Al–Si alloys: electron backscatter diffraction analysis. *Mater. Charact.* **46,** 305–310 (2001).
37. Heiberg, G. & Arnberg, L. Investigation of the microstructure of the Al–Si eutectic in binary aluminium–7 wt% silicon alloys by electron backscatter diffraction (EBSD). *J. Light Met.* **1,** 43–49 (2001).
38. Dahle, A. K., Nogita, K., McDonald, S. D., Dinnis, C. & Lu, L. Eutectic modification and microstructure development in Al–Si Alloys. *Mater. Sci. Eng. A* **413–414,** 243–248 (2005).

# Chapter 5:

# 3D Atom probe tomography study on segregation of yttrium in modified Al-Si alloys

## Summary

This chapter again seeks to address the first objective of this thesis, that is understanding the modification mechanism of hypoeutectic Al-Si alloys by comparing full modification and partial modification. In this chapter the segregation of Y, which has been clearly identified as a partial modifier, is investigated by 3D APT and compared against similar analysis presented in the literature for full modification performed by Sr or Na addition. Some microstructural analysis is presented again in this chapter for completeness and ease of reference, whilst the full analysis of the APT results is presented.

This is published work as indicated below and four authors have contributed, the author (M. De Giovanni), the author's thesis supervisor (P. Srirangam), Dr. Alam and Prof. Banerjee, both from the University of North Texas. The author's contribution to this publication was sample preparation, carrying out the microstructural analysis and the writing up of the publication. Dr. Talukder carried out the APT experimental work analysis, whilst Dr. Srirangam and Prof. Banerjee contributed intellectually.

*Results in this chapter published as:*

*De-Giovanni, M., Alam, T., Banerjee, R. & Srirangam, P. 3D Atom Probe Tomography Study on Segregation of Yttrium in Modified Al-Si Alloys. JOM* ***70,*** *1765–1770 (2018). doi: 10.1007/s11837-018-2909-x*

## 5.1. Abstract

Yttrium segregation behaviour in Al-Si alloys has been studied using three-dimensional atom probe tomography technique. Al-Si alloys were prepared by casting method, and yttrium was added to modify the eutectic silicon morphology in these alloys. The results indicate that yttrium is preferentially located within the Si phase, with the highest concentration being at the interface between eutectic Al and eutectic Si.

**Keywords:** Al-Si alloys, modification, atom probe tomography, yttrium.

## 5.2. Introduction

Aluminium-Silicon (Al-Si) alloys are widely used in automotive and aerospace industries due to their high strength to weight ratio, good castability, excellent mechanical and performance properties[1]. The microstructure of eutectic and hypoeutectic Al-Si is very coarse, with the eutectic being made up of large platelets or needles of silicon in a continuous aluminium matrix. Alloys exhibiting this microstructure show poor ductility due to the large and brittle silicon plates. The ductility and tensile strength of these alloys can be improved by addition of modifying elements such as sodium, strontium and rare-earth elements, which modify the eutectic silicon morphology from flake to fibrous shape[1–3]. The change in size and shape of the Si phase also improves the wear resistance of Al-Si alloys[4]. Among all these modifying elements, Sr is considered to be the best for modifying Al-Si alloys. There has been an ongoing debate regarding the mechanism of modification of Al-Si alloys. In an attempt to understand the modification mechanism, a number of researchers have looked into the segregation behaviour of modifying elements within the alloy. Clapham and Smith[5] used atomic absorption spectroscopy (AAS) and observed that Sr is preferentially located in the Si phase. Nogita et al.[6] used synchrotron-based micro-x-ray fluorescence (µXRF) and noted that Sr was segregated within the eutectic Si phase. Atom probe tomography (APT) has been used by several researchers to look into the segregation of the modifying element within Al-Si alloys[7–12]. Past studies have explored the application of Y as a modifier of Al-Si alloys. Researchers used varying amounts of Y, between 200 ppm and 6000 ppm and observed that, in the presence of Y, the Si eutectic forms a refined plate-like morphology rather than a fibrous one[13–15]. However, no studies were reported on the segregation behaviour of yttrium in such modified Al-Si alloys. In the work presented herein, for the first time, the segregation behaviour of yttrium in Al-Si alloy was studied using atom probe tomography; the results obtained from this study are presented and discussed.

## 5.3. Methodology

### 5.3.1. Alloy preparation

Al-Si alloy was prepared by melting 99.999% purity aluminium (NewMet, UK) in a clay graphite crucible using a Carbolite RHF1500 high-temperature chamber furnace. Silicon (99.999%, Alfa Aeser, UK) was added to the molten aluminium and stirred in. Once melting was complete, the mixture was poured into a preheated clay graphite crucible and left to solidify. The Al-Si was then used to prepare Al-Si-Y alloy. The Al-Si alloy was molten, then Al-10Y (wt.%) master alloy was added employing the same procedure. This master alloy was produced using a similar procedure using the same 99.999% purity aluminium and 99.9% purity yttrium (Alfa Aeser, UK). The chemical compositions of the two alloys were analysed by inductively coupled plasma optical emission spectroscopy (ICP-OES) and are presented in table 5.1.

Table 5.1: ICP-OES chemical composition analysis performed on the two alloys in weight percentage (wt%).

| | **Al** | **Si** | **Y** | **Fe** | **Cu** | **Mn** |
|---|---|---|---|---|---|---|
| **Al-Si** | Balance | 8.82 | - | <0.01 | <0.01 | <0.01 |
| **Al-Si-Y** | Balance | 7.75 | 1.09 | <0.01 | <0.01 | <0.01 |

### 5.3.2. Microstructural analysis

Metallographic samples were prepared from the cast cylinders for microstructural analysis by means of optical microscopy and scanning electron microscopy (SEM). Chemical analysis was performed using energy-dispersive spectroscopy (EDS). Etching was performed using 20% hydrochloric acid (37%) and 80% isopropyl alcohol mixture, to reveal the fibrous or lamellar structure of the Si eutectic. Five SEM images per composition were acquired at 5000 x magnification and analysed by using thresholding in ImageJ software.

### 5.3.3. Atom probe tomography

Site-specific APT specimens were prepared in a dual-beam focused ion beam scanning electron microscope (FIB/SEM) (FEI Nova 200 NanoLab) by standard lift-out method utilizing Pt-deposition and a micro-manipulator. A long bar was detached from the surface using the micromanipulator and transferred to prefabricated Si posts on a coupon, and small cut sections (~2 $\mu$m long) of the bar were welded on the Si posts. A procedure similar to that carried out in this research was described by Felfer et al.[16].

The samples mounted on the Si posts were annular milled to prepare taper-shaped needles with end radius of 20 nm to 40 nm. Under high vacuum and low temperature of 40 K, ions from the surface of this needle were evaporated inside the local electrode atom probe (LEAP) (Cameca 3000X HR). The energy for evaporation was supplied by a 512-nm green laser with laser pulse energy of 0.5 nJ. An automatic evaporation control protocol was employed to maintain steady-state evaporation of 0.5%. Raw APT data were collected from the LEAP, and reconstructed using the IVAS® 3.6.10 software package.

## 5.4. Results

Figure 5.1a and b shows optical images of the unmodified and the Y-modified Al-Si alloys. From these images, it is clearly visible that the Si eutectic is present in the form of plate-like structures in the unmodified alloy, whereas in Y-modified alloy the Si phase is present in finer lamellar structures. These structures are shown in greater detail in the images of etched samples in figure 5.1c and d. In the optical microscopy images, one can also observe the presence of a ternary phase in the Y-modified alloy. The arrows indicate two ternary-phase particles, however identifying these ternary phases is difficult due to similar contrast to the Si phase. The modification effect of yttrium was analysed quantitatively, in terms of Feret diameter and circularity by analysing a number of SEM images. It must be clarified that the quantitative analysis was performed on a two-dimensional (2D) cross-section and thus yields information regarding the apparent size and shape of the Si eutectic in this plane. The Feret diameter is defined as the longest distance between any two points along the selection boundary[17]. Circularity is defined by $4\pi * \frac{Area}{Perimeter^2}$, where a value of 1 indicates a perfect circle, with decreasing values indicating a less circular feature[17]. Histograms are presented in figure 5.1e and f, showing that the Feret diameter in the samples containing Y was typically smaller. A further indication of the marginal modification after Y addition is given by the higher circularity of the Si phase in this alloy.

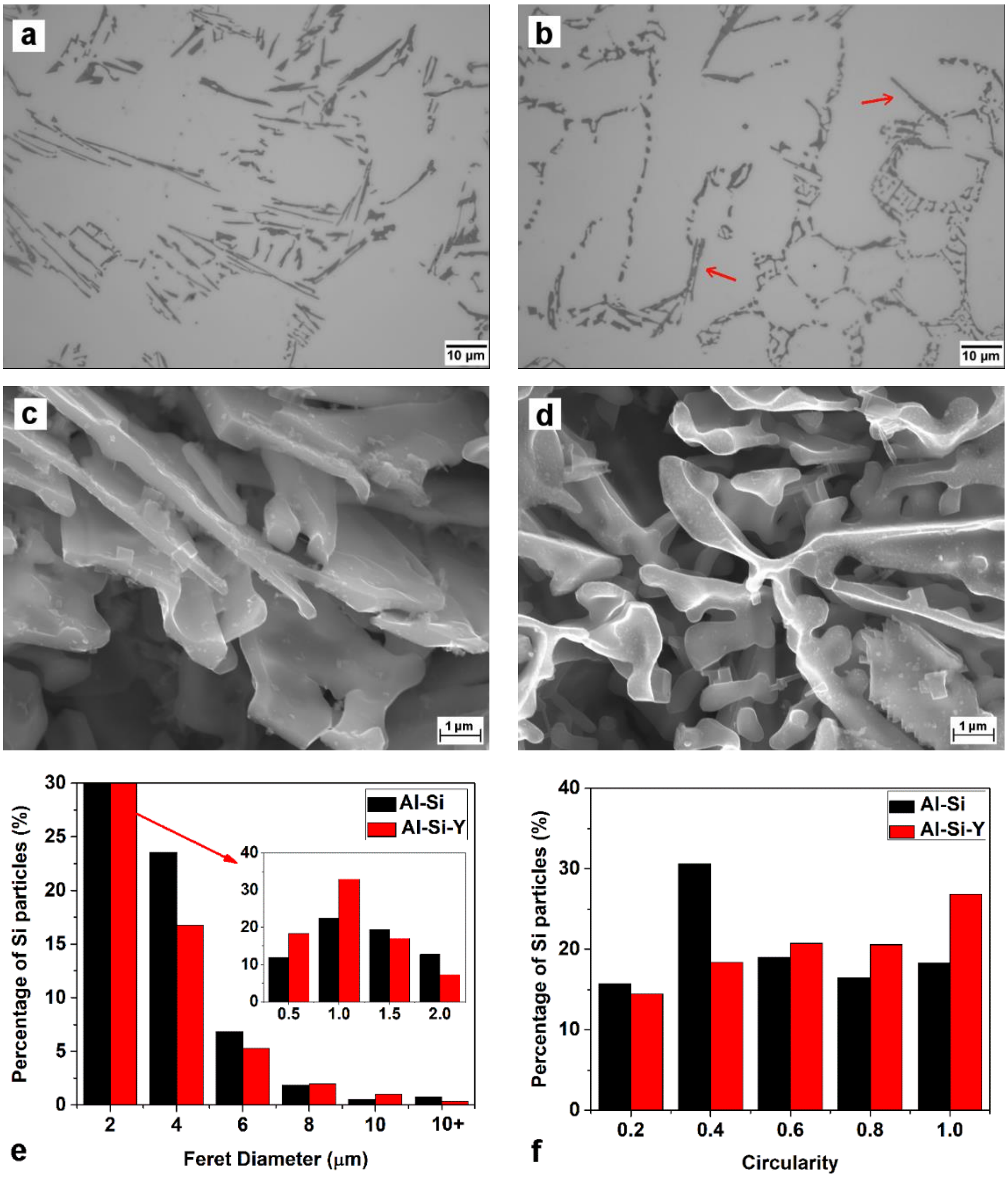

Figure 5.1: Optical micrographs showing (a) unmodified Al-Si alloy and (b) modified Al-Si-Y alloy. SEM images of etched samples of (c) unmodified Al-Si alloy and (d) modified Al-Si-Y). (e) Size and (f) shape analysis of Si phase extracted from SEM images at x5k.

Figure 5.2 presents SEM images, including chemical analysis. The electron images yield similar information to the optical microscopy images, though at higher magnification. Furthermore, the ternary-phase intermetallics have bright contrast. The chemical analysis images show that Y was found mainly in the ternary intermetallic phase. The concentration of Y in eutectic Si or primary Al would be very low, hence detection of such small concentrations by means of EDS would be difficult and unreliable. Similar ternary intermetallic precipitates were observed at concentrations as low as 200 ppm Y[15].

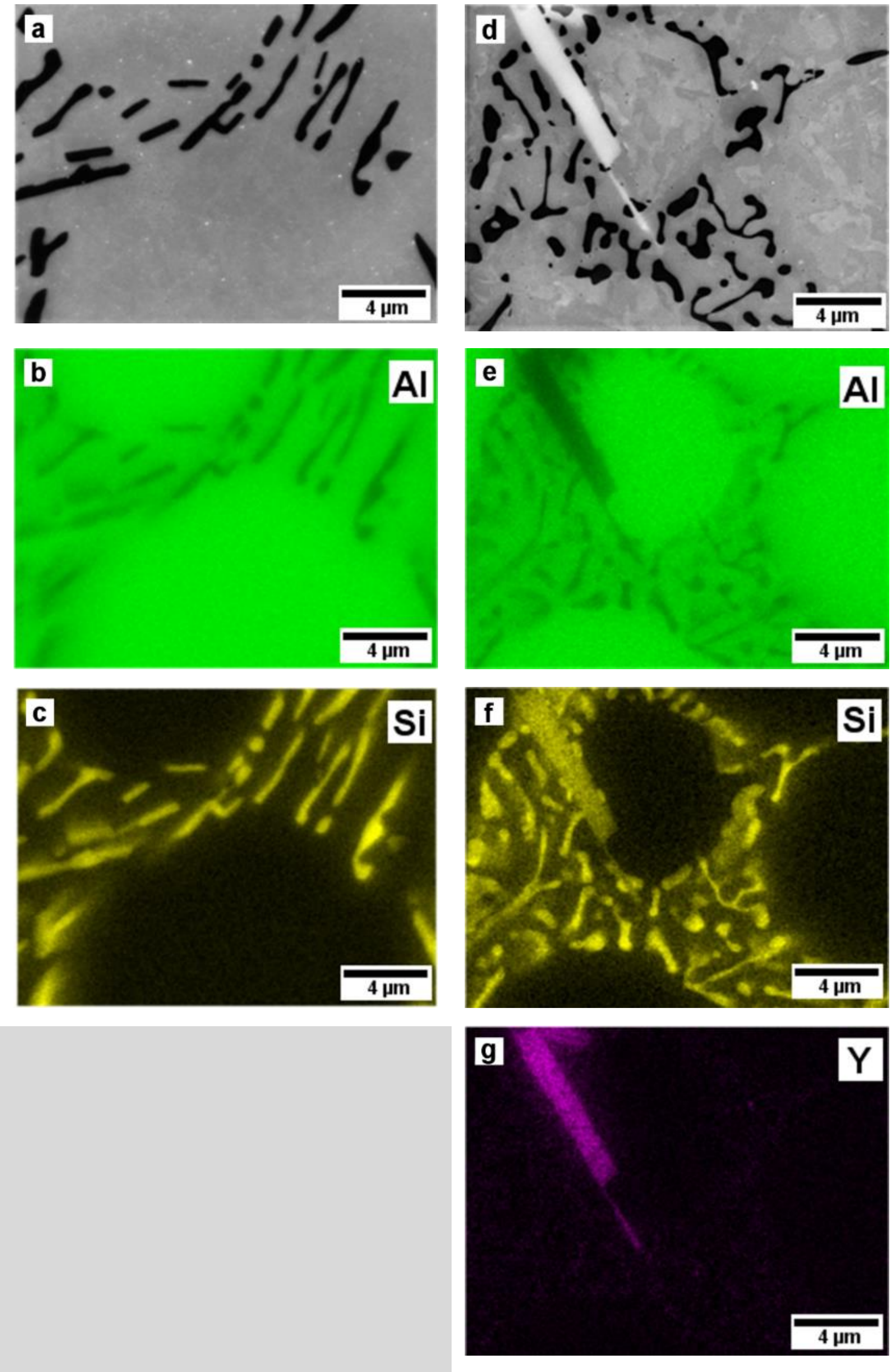

Figure 5.2: SEM images representing (a) unmodified Al-Si and (d) Al-Si-Y alloy, and EDS maps representing elemental analysis for corresponding Al (b, e), Si (c, f) and Y (g).

Figure 5.3 shows raw ion maps of the whole reconstructed area. From this map it can be observed that there is a clear distinction between the Al and Si phases and the presence of the different elements in the other phases is minimal. From these raw ion maps, it can also be observed that, although Y is present throughout the entire sample, it is preferentially located in the Si phase.

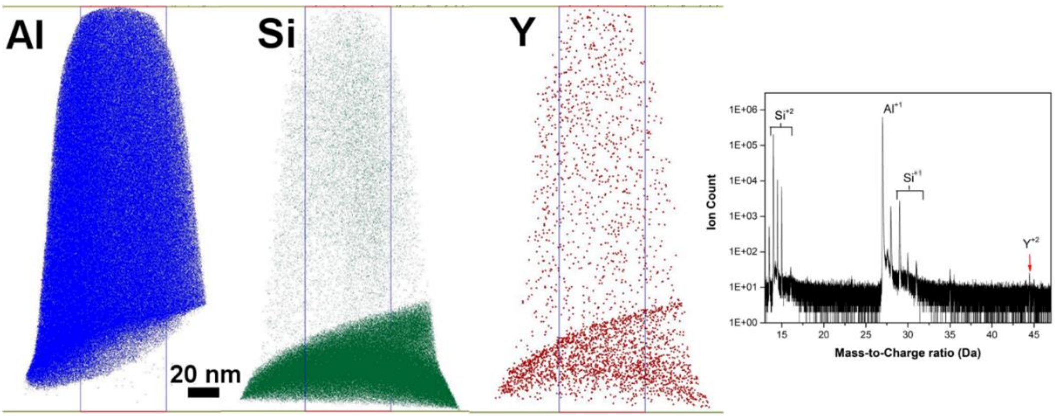

Figure 5.3: Raw ion maps of the whole APT reconstruction of Al-Si alloys modified with yttrium, including the mass-to-charge ratio spectra with identified Al, Si and Y peaks.

Figure 5.4a is a 150-nm cropped section across the phase boundary between the Al and Si phases.  The Y ions, depicted as red spheres, are clearly seen to segregate at the Si phase, with higher presence at the phase boundary. This segregation at the boundary could occur due to Y atoms being pushed out of the solidifying phases, thus a boundary that is rich in Y forms in this position.

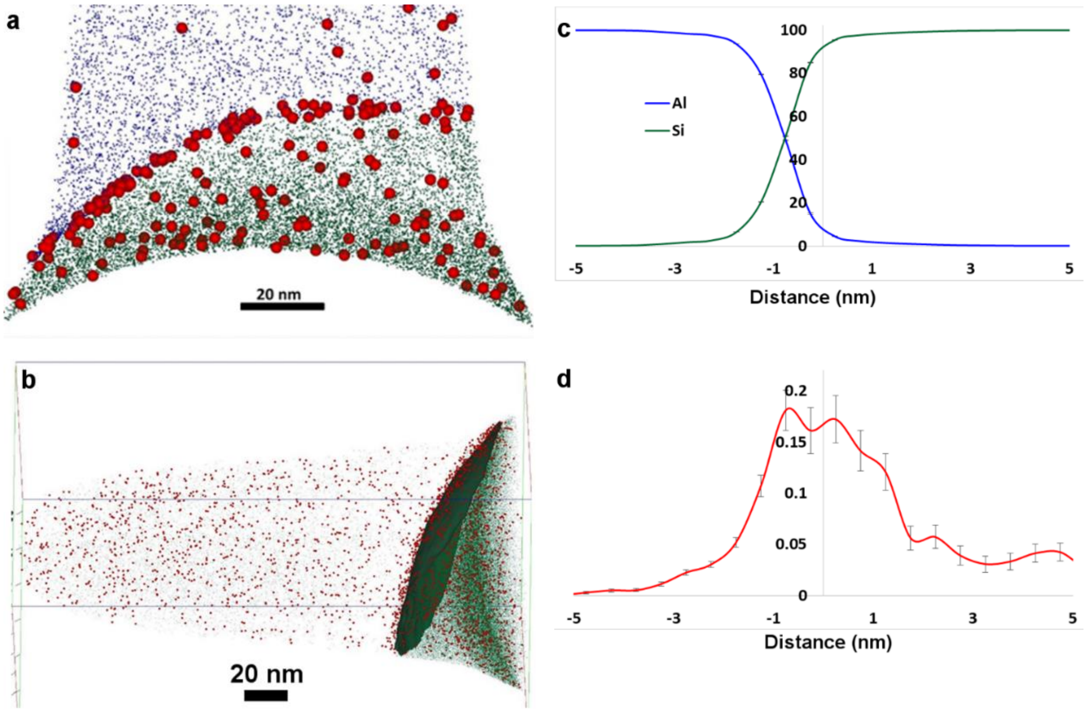

Figure 5.4: (a) 15-nm slice view of reconstruction showing segregation of Y in the phase boundary. Y ions (red spheres) are clearly seen at the interface of Al-rich and Si-rich phase. (b) isoconcentration surface of Si at 50% outlines the phase boundary between the Al-rich and Si-rich phases. (c) Proxigram generated from the isosurface reveals the Al and Si partitioning between the phases. (d) Proxigram of Y clearly reveals that it is segregated in the phase boundary and preferentially partitions to the Si-rich phase.

Figure 5.4b, c and d shows the isoconcentration surface of Si = 50 at% outlining the phase boundary between the Al-rich and Si-rich phases with the corresponding proxigrams for Al, Si and Y. From these, it can be observed that there is minimal mixing between the Al and Si phases. More importantly, Y is clearly revealed to be segregated at the phase boundary of the two phases and preferentially partitions into the Si-rich phase.

## 5.5. Discussion

From the APT results obtained, it is clear that Y, similarly to other elements which fully modify the eutectic Si phase such as Sr and Na, segregates preferentially into the Si phase. Furthermore, Y seems to be pushed to the eutectic Si boundary. This behaviour correlates with the findings of Li et al.[11] for Na modification but is in contrast to Srirangam et al.[7] for Sr modification. Srirangam et al.[7] noted segregation of Sr within the eutectic Si phase with no indication of enrichment at the interface whereas, Li et al.[11] noted that Na enrichment at the interface between eutectic Si and eutectic Al in Na-modified Al-Si alloys. It is therefore indicative that the phase where the additional element segregates does not necessarily indicate the modification potential of the element.

Other authors delved deeper into the eutectic Si and explored the characteristics of the Sr segregations within this phase. Timpel et al.[8,9] noted that Sr is heterogeneously cosegregated with Al within the Si phase and these form either a nanometre-scale rod-like segregation or more extended structures. The rod-like formations were regarded as being responsible for the twin formation and the enablement of growth in different crystallographic orientations, whereas the extended structures were believed to be responsible for growth restriction and branching of the Si crystal. The ability of these three elements to cosegregate was regarded as indicative that these promote the formation of new twins. Barrirero et al.[10] similarly identified rod-like nanoscale cosegregations (responsible for smoothening of Al-Si boundaries in eutectic phase) and particle-like and planar cosegregations (favouring formation of twin boundaries). The particle-like segregations were also observed in the unmodified alloy, though obviously containing exclusively Al. The authors further noted that the concentration of Al within the eutectic was approximately four times higher in the modified alloy when compared with the unmodified, which further supports the hypothesis that Al and Sr are incorporated together into the Si phase in the form of nanometre-sized phases. Li et al.[11] investigated the segregation of sodium (Na), another well-known modifier, in Al-5Si alloy. They noted that similar rod-like and particle-like structures formed. Barrireo et al.[12] also performed compositional analysis of the nanometre-sized clusters by means of APT, which indicated presence of NaAlSi and $SrAl_2Si_2$ in Na- and Sr-modified Al-Si alloys respectively. They proposed that the clusters form at the Si/liquid interface and take part in the modification process by altering the eutectic growth. They suggest that the efficiency of a modifier depends on the ability to form ternary compound clusters at the Si/liquid interface near the binary eutectic point. Further research is required to investigate the segregation of the Y within Si to identify whether Y within the Si phase is cosegregated with Al, similarly to the case of Sr and Na, and the morphology of such segregations. Future studies involving extensive transmission electron microscopy (TEM) work is required to understand the effect of yttrium on formation of nano ternary compounds and twins in eutectic silicon phase in Al-Si alloys. However, the present study clearly shows that the yttrium addition does not result in significant modification of eutectic silicon morphology, although yttrium is found to be preferentially segregated in the silicon phase.

## 5.6. Conclusions

- Al-Si alloys are partially modified with addition of yttrium using casting method.
- Segregation behaviour of yttrium was studied using 3D atom probe tomography.
- APT results clearly shows that yttrium preferentially segregated in eutectic silicon phase and resulted in only partial modification of eutectic silicon.

## 5.7. References

1. Polmear, I. J. in *Light Alloys* 205–235 (Elsevier, 2005). doi:10.1016/B978-075066371-7/50008-6
2. Bartley, R. *British and European Aluminium Casting Alloys*. (Association of Light Alloy Refiners, 1996).
3. Hatch, J. E. *Aluminium: Properties and Physical Metallurgy*. (American Society of Metals, 1984).
4. Lee, S.-L., Cheng, Y.-C., Chen, W.-C., Lee, C.-K. & Tan, A.-H. Effects of strontium and heat treatment on the wear-corrosion property of Al–7Si–0.3Mg alloy. *Mater. Chem. Phys.* **135,** 503–509 (2012).
5. Clapham, L. & Smith, R. W. Segregation behaviour of strontium in modified and unmodified Al-Si alloys. *J. Cryst. Growth* **92,** 263–270 (1988).
6. Nogita, K. *et al.* Determination of strontium segregation in modified hypoeutectic Al–Si alloy by micro X-ray fluorescence analysis. *Scr. Mater.*

**55,** 787–790 (2006).

7. Srirangam, P. *et al.* Probing the local atomic structure of Sr-modified Al–Si alloys. *Acta Mater.* **65,** 185–193 (2014).
8. Timpel, M. *et al.* The role of strontium in modifying aluminium–silicon alloys. *Acta Mater.* **60,** 3920–3928 (2012).
9. Timpel, M. *et al.* Sr–Al–Si co-segregated regions in eutectic Si phase of Sr-modified Al–10Si alloy. *Ultramicroscopy* **132,** 216–221 (2013).
10. Barrirero, J. *et al.* Comparison of segregations formed in unmodified and Sr-modified Al–Si alloys studied by atom probe tomography and transmission electron microscopy. *J. Alloys Compd.* **611,** 410–421 (2014).
11. Li, J. H. *et al.* Nucleation and Growth of Eutectic Si in Al-Si Alloys with Na Addition. *Metall. Mater. Trans. A* **46,** 1300–1311 (2015).
12. Barrirero, J. *et al.* Cluster formation at the Si/liquid interface in Sr and Na modified Al–Si alloys. *Scr. Mater.* **117,** 16–19 (2016).
13. Knuutinen, A., Nogita, K., McDonald, S. D. & Dahle, A. K. Modification of Al–Si alloys with Ba, Ca, Y and Yb. *J. Light Met.* **1,** 229–240 (2001).
14. Li, B., Wang, H., Jie, J. & Wei, Z. Effects of yttrium and heat treatment on the microstructure and tensile properties of Al–7.5Si–0.5Mg alloy. *Mater. Des.* **32,** 1617–1622 (2011).
15. Li, J. H. & Schumacher, P. Effect of Y addition and cooling rate on refinement of eutectic Si in Al–5 wt-%Si alloys. *Int. J. Cast Met. Res.* **25,** 347–357 (2012).
16. Felfer, P. J., Alam, T., Ringer, S. P. & Cairney, J. M. A reproducible method for damage-free site-specific preparation of atom probe tips from interfaces. *Microsc. Res. Tech.* **75,** 484–491 (2012).
17. Ferreira, T. & Rasband, W. *ImageJ User Guide IJ 1.46r*. *IJ 1.46r* (2012). doi:10.1038/nmeth.2019

# Chapter 6:

# 3D imaging and quantification of porosity and intermetallic particles in strontium modified Al-Si alloys

## Summary

This chapter seeks to address part of the second objective of this thesis, that is whether porosity in modified alloys can be reduced by adding rare earth elements. In this chapter the porosity in Sr-modified Al-Si was addressed specifically by using 3D XCT. This was done to provide an understanding of the shape and size characteristics of porosity within such alloys. Furthermore, the intermetallics characteristics were also analysed and their relationship to the porosity was also discussed.

This is published work as indicated below and four authors have contributed, the author (M. De Giovanni), the author's thesis supervisor (P. Srirangam), Dr. Warnett and Prof. Williams, both from the metrology group at WMG, University of Warwick. The author's contribution to this publication was sample preparation, carrying out the microstructural analysis and the writing up of the publication. Dr. Warnett carried out the XCT experimental work and analysis, whilst Dr. Srirangam and Prof. Williams contributed intellectually.

*Results in this chapter published as:*
*M. De Giovanni, J.M. Warnett, M.A. Williams, and P.Srirangam, 3D imaging and quantification of porosity and intermetallic particles in strontium modified Al-Si alloys, Journal of Alloys and Compounds 727 (2017) 353-361. doi: 10.1016/j.jallcom.2017.08.146.*

## 6.1. Abstract

Al-Si alloys are widely used in the automotive and aerospace industries. Porosity is considered to be a major defect in these cast alloys. In this study, the effect of strontium (Sr) modification on porosity formation and intermetallic formation in Al-Si alloys is quantified using x-ray tomography. Quantitative information such as average pore size, shape, pore distribution and intermetallic particle size distribution were evaluated for Sr modified and unmodified Al-Si alloys. Results show that the addition of 400 ppm of Sr increases the porosity by 10% as compared to unmodified Al-Si alloy. Further, Sr addition increases the average equivalent diameter of pores from 2 µm to 18 µm compared to unmodified alloys. A greater number of larger pores were found in the Sr modified alloy, whereas the number of small sized pores was significantly higher in unmodified alloy. The addition of 400 ppm of Sr results in formation of Al-Si-Sr intermetallics with an average equivalent diameter of 4.5 µm. It can be hypothesised that these intermetallic particles act as heterogeneous sites for pore nucleation and significant further growth of porosity in Sr modified alloys.

**Keywords:** Al-Si alloys, Sr modification, micro porosity, $Al_2Si_2Sr$ intermetallics, x-ray tomography.

## 6.2. Introduction

Aluminium-Silicon (Al-Si) alloys are widely used in the automotive, aerospace and casting industries due to their excellent strength to weight ratio, high corrosion resistance, good weldability, excellent mechanical and performance properties[1]. Eutectic silicon appears in the form of needles or platelets which results in poor mechanical properties of these alloys. To reduce this effect, these alloys are usually treated with trace level additions of modifying elements such as sodium or strontium or rare earth elements[1,2]. Strontium is typically used due to its high retention and low over-modification issues in cast Al-Si alloys. Although strontium modification improves microstructure and mechanical properties[1–3], it also results in a significant increase in porosity that negatively impacts the fatigue properties of cast alloy[4–8].

Porosity in Al-Si cast alloys occurs as gas porosity or shrinkage porosity[9]. Emadi et al.[9] list several factors that could lead to an increase in porosity due to strontium modification in Al-Si alloys; an increase in hydrogen content of melt, an absorption of hydrogen to oxides, a decrease in solubility of hydrogen during solidification, a depression in eutectic temperature, an increase in inclusion content, a decrease in surface tension of molten metal and an increased volumetric shrinkage of the alloy. Emadi et al.[9] noted that addition of 0.01 wt% Sr to A356 alloy decreases the surface tension by 19% and increases the volumetric shrinkage by 12%. Furthermore, it was observed that the modification treatment promotes the early formation of pores during solidification thus allowing more time for large pores to develop[9,10]. Several studies suggested that in unmodified alloys the eutectic liquid seemed to flow between interdendritic regions, while, Sr modification affects the bifilms' retention in liquid which restricts the mobility of liquid into interdendritic regions thereby increasing porosity content in the alloys[11–13]. A number of studies have shown that the presence of oxides increases porosity by decreasing the fluidity of the melt[14–18].

Though much research has been carried out to understand the porosity formation in Sr modified alloys, the mechanism is still unclear. Understanding porosity formation and its increase in Sr modified Al-Si alloys is essential to improve the melt quality, mechanical properties and to reduce hot tearing and wastage of castings. This porosity is one of the main reasons for fatigue cracks initiation in the castings[19–22]. Researchers have observed a direct correlation between pore size and shape to resultant fatigue life of cast components[19,23]. Most of these studies were carried out using conventional microscopy techniques which provides 2D microstructural images of pores, used to predict the mechanical properties of Al-Si alloys. Since pores will have different shapes and morphologies in different orientations, it is essential to visualise and quantify them in 3D to better predict the mechanical properties of these alloys.

X-Ray Computed Tomography (XCT) is a powerful non-destructive technique which provides a three-dimensional (3D) visualisation of internal structure inhomogeneities representative of bulk sample[24–26]. XCT has been applied in numerous fields of research such as medical[27], geology[28] and civil engineering[29]. Several XCT studies were carried out in the past on characterising porosity in Al alloys using XCT and using this data in predicting fatigue properties of these alloys. However, the resolutions obtained in these studies varied between 1.7 – 30 µm[30–34]. In this study, for the first time, lab-based submicron resolution XCT was used to visualise and quantify porosity in Sr modified Al-Si alloys and compare to an unmodified alloy. Furthermore, the formation of Al-Si-Sr intermetallics in Sr modified Al-Si alloys were studied using XCT and SEM analysis.

## 6.3. Experimental Methods

### 6.3.1. Alloy preparation

Al-Si alloy was prepared by melting 99.999% purity aluminium (NewMet, UK) in a clay graphite crucible using a Carbolite RHF1500 high temperature chamber furnace. High purity (99.999%) silicon (Alfa Aeser, UK) was added to the molten aluminium and stirred to ensure mixing of silicon in the melt. Once the silicon dissolved in the melt, the mixture was poured into a graphite cylindrical mould (12 mm diameter, 85 mm deep). A portion of the Al-Si alloy was then used to prepare modified Al-Si-Sr alloy. When the Al-Si alloy was in a molten state, the Al-10Sr (wt%) master alloy was added to the melt, and returned to the same mould. The cooling rate was approximately 75 °C/s. Table 6.1 shows the composition analysis performed by inductively coupled plasma optical emission spectroscopy (ICP-OES).

Table 6.1: ICP-OES chemical composition analysis performed on the two alloys in weight percentage (wt%).

| | **Al** | **Si** | **Ce** | **Sr** | **Fe** | **Cu** | **Mn** |
|---|---|---|---|---|---|---|---|
| **Al-Si** | Balance | 8.82 | - | <0.01 | <0.01 | <0.01 | <0.01 |
| **Al-Si-Sr** | Balance | 8.78 | - | 0.02 | <0.01 | <0.01 | <0.01 |

For XCT measurements, samples with a diameter of 1 mm were machined from the centre of the cast using wire EDM.

### 6.3.2. X-Ray computed tomography

XCT measurements were performed using the Zeiss Versa 520 system. The cylindrical samples with 1 mm diameter were mounted on the rotating stage in the XCT machine. As x-rays pass through the sample, they are either attenuated or pass through the sample resulting in a grey-scale radiograph on the detector screen. Numerous radiographic projections obtained through a 360 degree rotation were then reconstructed into a 3D volume through the process of filtered back projection. The volume consisted of a number of 3D pixels called voxels with an associated grey value between 0 and 65535, proportional to the attenuation of the material.

Table 6.2: X-Ray tomography scanning parameters

| | |
|---|---|
| Voltage (kV) | 80 |
| Power (W) | 7 |
| Exposure (s) | 24 |
| Filter ($SiO_2$, mm) | 0.35 |
| Number of Projections | 3201 |
| Voxel size (nm) | 390 |

The XCT scan parameters are given in table 6.2. In the scans provided for this study a 20x optic was used in combination with a 2000 * 2000 pixel detector. This resulted in a 390 nm voxel size in the reconstructed volume, measuring 780 * 780 *780 microns. The imaged volumes were segmented using a watershed based algorithm in Avizo 9.3 (FEI, USA)[35]. The principles of image segmentation and XCT operation can be found in an earlier publication[36].

### 6.3.3. Cooling curves

The progression of solidification of the two samples was analysed by examining their respective cooling curves. Approximately 15 g of each sample were placed in a clay graphite crucible and melted at 750 °C in an electrical resistance furnace. Once molten, the crucible was taken out and immediately a K-type thermocouple was inserted below the surface of the melt. The cooling curve was collected using a data logger recording at 10 Hz. A cooling rate of 1.2 °C/s was observed.

## 6.4. Results and Discussion

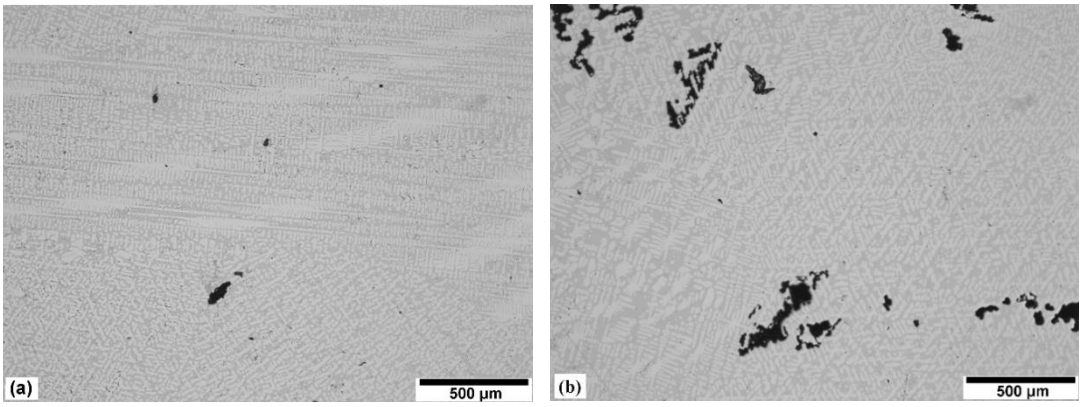

Figure 6.1: Optical microscopy images of (a) Al-Si, and (b) Al-Si-Sr.

Figure 6.1 shows the optical microscopy images of Al-Si and Al-Si-Sr modified alloys. It is clearly evident from figure 6.1 that there is a significant difference in the porosity distribution in the two alloys. The unmodified alloy shows less porosity with a few small pores as represented in figure 6.1 (a), while, the modified alloy shows higher porosity with the presence of large pores shown in figure 6.1 (b). Figure 6.2 (a and b) shows XY ortho slices in Al-Si and Al-Si-Sr alloy samples respectively from XCT measurements. It is evident that the Al-Si unmodified alloy contains very fine pores (figure 6.2 a), whereas the Al-Si-Sr modified alloy contains extremely large pores (figure 6.2 b). The insets in these images represent higher magnification images showing different pore features in the two alloys. As shown in figure 6.2 (a), an area is magnified for highlighting small pores in the unmodified alloy. In the modified alloy, the magnified image figure 6.2 (b) clearly shows the presence of intermetallic particles represented by bright spots. The scanned samples were taken from the centre of the alloy castings where it is known that porosity is higher[37]. Figure 6.2 (c and d) represents the complete three-dimensional reconstructions of porosity and intermetallic particles in unmodified and Sr modified Al-Si alloys respectively. The green, blue and red colours in figure 6.2 (c and d) represents the Al matrix, porosity and intermetallic particles in cast alloys respectively.

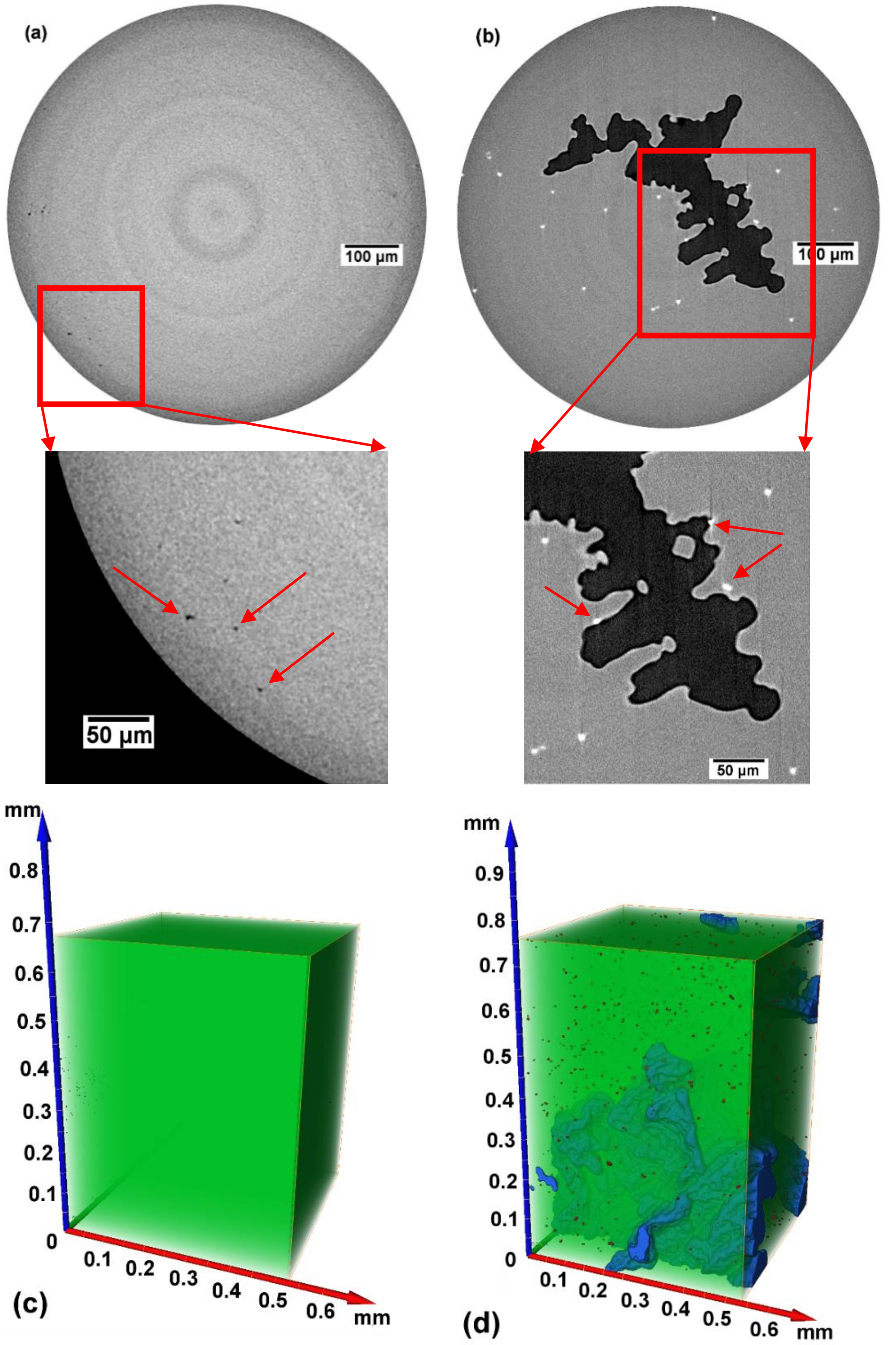

Figure 6.2: XY ortho slices in (a) Al-Si showing the presence of small pores and (b) Al-Si-Sr showing the presence of a large pore and smaller intermetallic particles. The insets show higher magnification images. In the Al-Si inset, the small pores can be observed better, whereas in the Al-Si-Sr the intermetallics surrounding the pore are highlighted. Full 3D reconstructed images of (c) Al-Si alloy showing the matrix (green) and pores (blue) and (d) Al-Si-Sr alloy showing the matrix (green), pores (blue) and particles (red).

In figure 6.3 the matrix is removed from view displaying only the pores. Since the pores are particularly small in the Al-Si alloy, they have been dilated 3x for visualisation purposes. The unmodified Al-Si alloy contains a large number of small pores (figure 6.3 a) which are mainly located in the central region of the sample, compared to the significantly larger pores observed with the addition of Sr (figure 6.3 b). There are still a limited number of smaller pores in the Al-Si-Sr alloy, but the large pores dominate the image. In order to visualise the smaller pores, the larger pores have been removed and the smaller pores dilated by 3x in figure 6.3 c. Furthermore it can be noted that in figure 6.3  the pores are in contact with the edge of the boundary box. This suggests that these pores extend beyond the boundary box and thus it is likely that the sizes of these pores is underestimated.

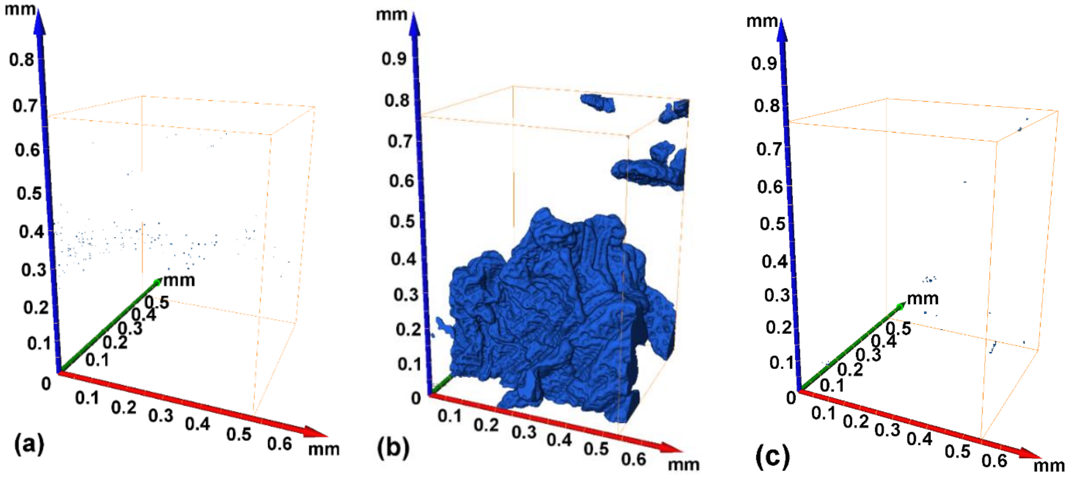

Figure 6.3: 3D reconstruction of pores from XCT data in (a) Al-Si, (b) Al-Si-Sr and (c) Al-Si-Sr following the removal of large pores. For visualisation purposes the pores in (a) and (c) were dilated by 3x.

To assess the porosity shape and size distribution in unmodified and modified alloys, XCT data was analysed using Avizo and is presented in figure 6.4. Figure 6.4 (a) shows that the vast majority of the pores in the Al-Si alloy were found to have an equivalent diameter which is less than 2 µm, with the largest pore having an equivalent diameter which is approximately 4 µm. In order to understand the shape change of pores due to Sr addition, sphericity calculations were performed using equation 1.  Sphericity is a measure of how spherical a feature is where, a sphericity value of 1 represents a perfect spherical shape of the pore[38].

$$\Psi = \frac{\pi^{\frac{1}{3}}(6V_p)^{\frac{2}{3}}}{A_p} \qquad (1)$$

In equation 1, $\Psi$ represents the sphericity, Vp represents the volume of a pore, $A_p$ represents the area of a pore. Figure 6.4 (b and c) represents the sphericity analysis of Al-7Si. Figure 6.4 (b) shows that the sphericity value for most of the pores in unmodified alloys is in the range between 0.8 and 0.9 which represents that the pores are close to spherical in shape in unmodified alloy. Figure 6.4 (c) shows how sphericity varies with the volume of the particle. It can be noted that almost all pores with an equivalent diameter greater than 2 µm have a sphericity value between 0.7 and 1.0 showing that a pore nucleates in an almost spherical shape. This spherical shape can change as the pore grows further with more diffusion of hydrogen into the nucleated pore during solidification of alloy casting.

Figure 6.4 (d-f) represents quantification of porosity in the Al-Si-Sr modified alloy. As shown in figure 6.4 (d), the modified alloy shows a significant number of large pores with an equivalent diameter >5 µm. Further it is evident that, the number of small sized pores with an equivalent diameter <2 µm, were found to be less in number in the modified alloy as compared to the unmodified alloy. The modified alloy demonstrated a bi-modal distribution of pores (2.5 - 4 µm vs >5 µm) in the casting as shown in figure 6.4 (d). Similar observations were made by Lashkari et al.[31] in which they attributed the large size pores formation to hydrogen gas solubility in the alloy and small pores formation to the local entrapment of liquid metal at the end of interdendritic feeding. It is well known that gas pores form in spherical shape but as solidification proceeds, more hydrogen diffuses into already nucleated pores resulting in their growth and ultimately large pore formation in the casting. Figure 6.4 (e) represents the sphericity of pores in the Al-Si-Sr modified alloy. The sphericity of pores in the modified alloy is largely confined to values between 0.6 and 0.8, with the exception of a countable few that are very low in sphericity and correlate to the largest pores. Even eliminating these exceptions, the sphericity of the pores in the modified alloy is lower than the Al-Si cast. This observation is in contradiction to Liao et al.'s[4] study where they noted that the sphericity in modified alloys is higher compared to unmodified alloys. The presented data is of higher resolution than the previous study, which could account for differences in the perceived sphericity.

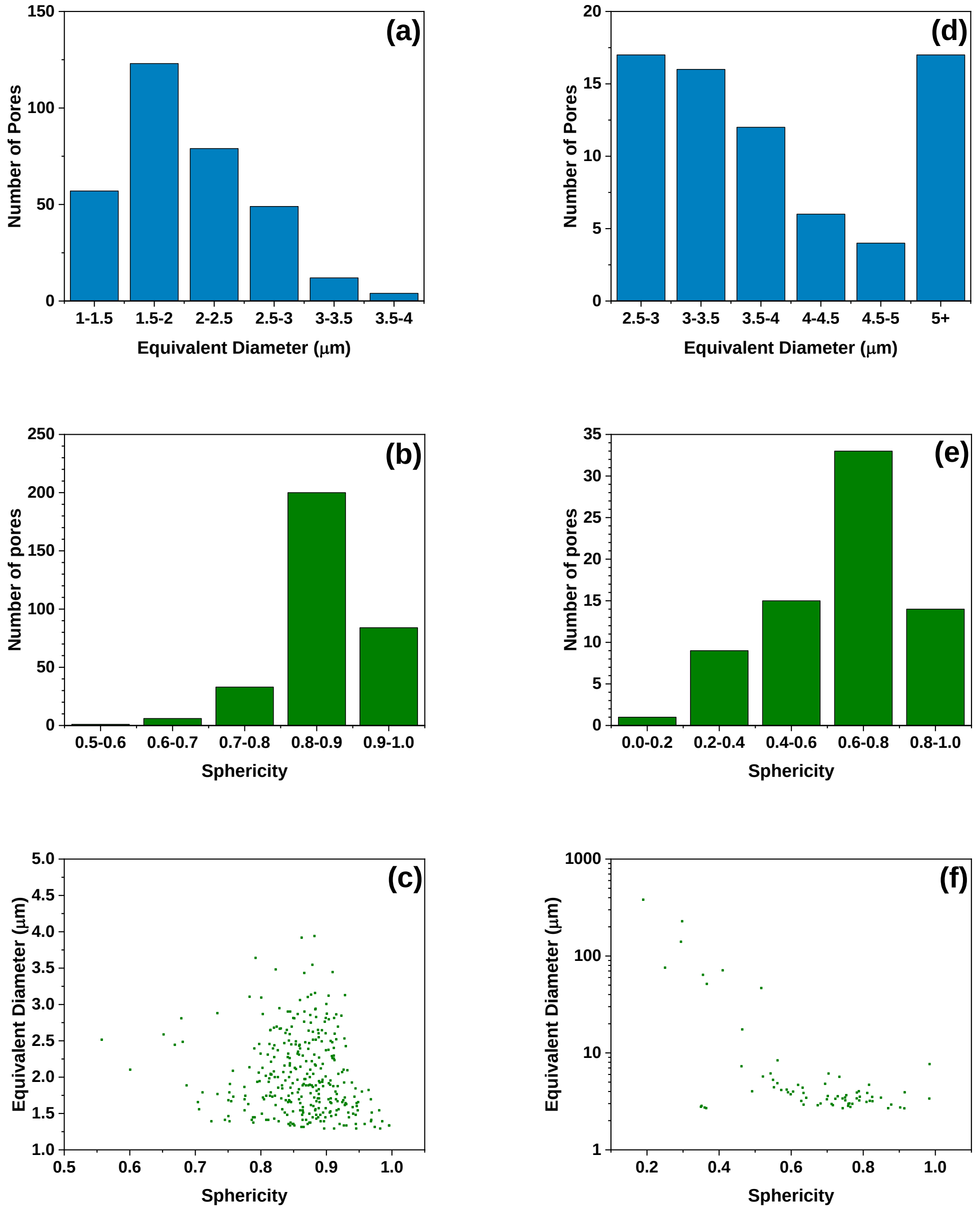

Figure 6.4: Data obtained from XCT for (a-c) Al-Si, (d-f) Al-Si-Sr alloy. (a, d) Size distribution of porosity, (b, e) Sphericity of the pores, (c, f) Relationship of sphericity to the size of the pores. Note that the y-scale is different for the two different samples.

Figure 6.5 (a and b) represents the magnified images of a single largest pore in Al-Si and Al-Si-Sr alloys respectively. The largest pore in Al-Si is close to a spherical shape and is approximately 0.01 mm in diameter, compared to the Sr modified alloy that is nearly 100 times larger and distinctly non-spherical. This shape of the largest pore in the modified alloy is indicative of shrinkage porosity as it shows the inter-dendritic shape resulting from lack of mass feeding. This kind of dendritic arm impingement on the pore has previously been reported in Al-Si alloys with Si content (<10%) in the alloys[39].

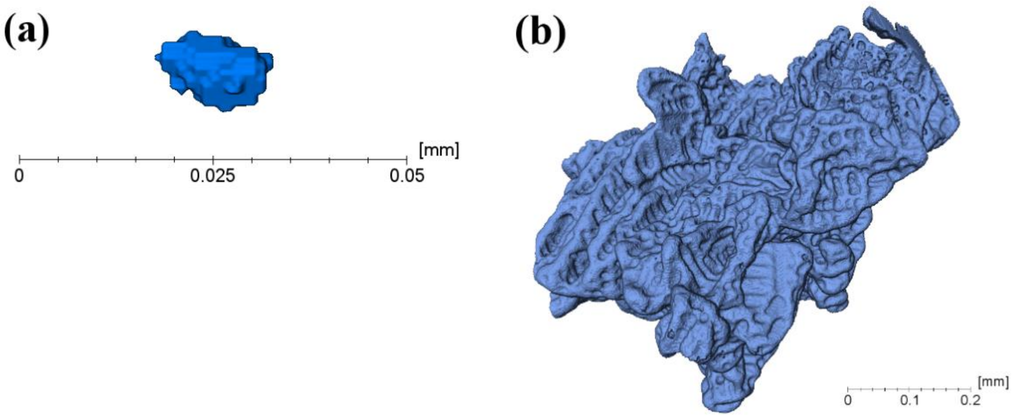

Figure 6.5: 3D reconstructed images of the largest pores in (a) Al-Si, (b) Al-Si-Sr.

A numerical comparison of the porosity is given in table 6.3. It is clear from table 6.3 that the porosity is only 0.00006% in unmodified alloy, while that in the Sr modified alloy is greater than 10%. Similar observations were made by previous researchers where they noted a reduction in the number of pores but the overall porosity increases due to modification with Sr in Al-Si alloys [4]. This is further shown by comparing the average and maximum pore volumes in the sample, where the maximum pore volume in the Sr modified alloy was found to be six orders of magnitude greater than the unmodified alloy.

Table 6.3: Quantitative information of porosity in Al-Si and Al-Si-Sr alloys as well as and intermetallic particles in Al-Si-Sr.

| | **Al-Si** | **Al-Si-Sr** |
|---|---|---|
| Total volume analysed (mm$^3$) | 0.290 | 0.336 |
| Pore percentage (%) | 0.00006 | 11.101 |
| Particle percentage (%) | - | 0.034 |
| Average pore equivalent diameter (µm) | 2.03 | 18.30 |
| Maximum pore equivalent diameter (µm) | 3.94 | 381.00 |
| Average intermetallic equivalent diameter (µm) | - | 4.52 |
| Maximum intermetallic equivalent diameter (µm) | - | 10.66 |

Figure 6.6 shows the presence and quantification of intermetallic particles in the Al-Si-Sr alloy. The 3D reconstruction of these particles within the alloy is shown in figure 6.6 (a), where an even spatial distribution is observed. Figure 6.6 (b) shows the size distribution of these particles where the majority are less than 6 µm, however a few exceed an equivalent diameter of 10 µm. Similar to pores, the sphericity of these intermetallic particles was also investigated as shown in figure 6.6 (c and d). Figure 6.6 (c) shows that majority of intermetallic particles were close to a value between 0.9 and 1, demonstrating a strongly spherical nature. Furthermore, very few particles (0.3%) have a sphericity value less than 0.8. Figure 6.6 (d) shows that sphericity values between 0.9 and 1.0 are mainly occupied by particles with an equivalent diameter less than 6 µm, whilst larger particles tend to be less spherical. Figure 6.6 (e) shows a magnified image of the largest intermetallic particle in the Sr modified alloy. Miresmaeili et al.[40] have observed similar intermetallic particles in A356 alloy modified by 0.04 wt% Sr by SEM, a 2D technique. Sigworth et al.[41] note that the usual amount of Sr required for modification is in the range 100-200 ppm and any amount higher than 200 ppm would result in formation of Al-Si-Sr intermetallic compounds. The reason for formation of these particles in the Sr modified alloy in this study could be due to higher amounts of Sr in the melt, in addition to holding the melt at 750 °C for longer time.

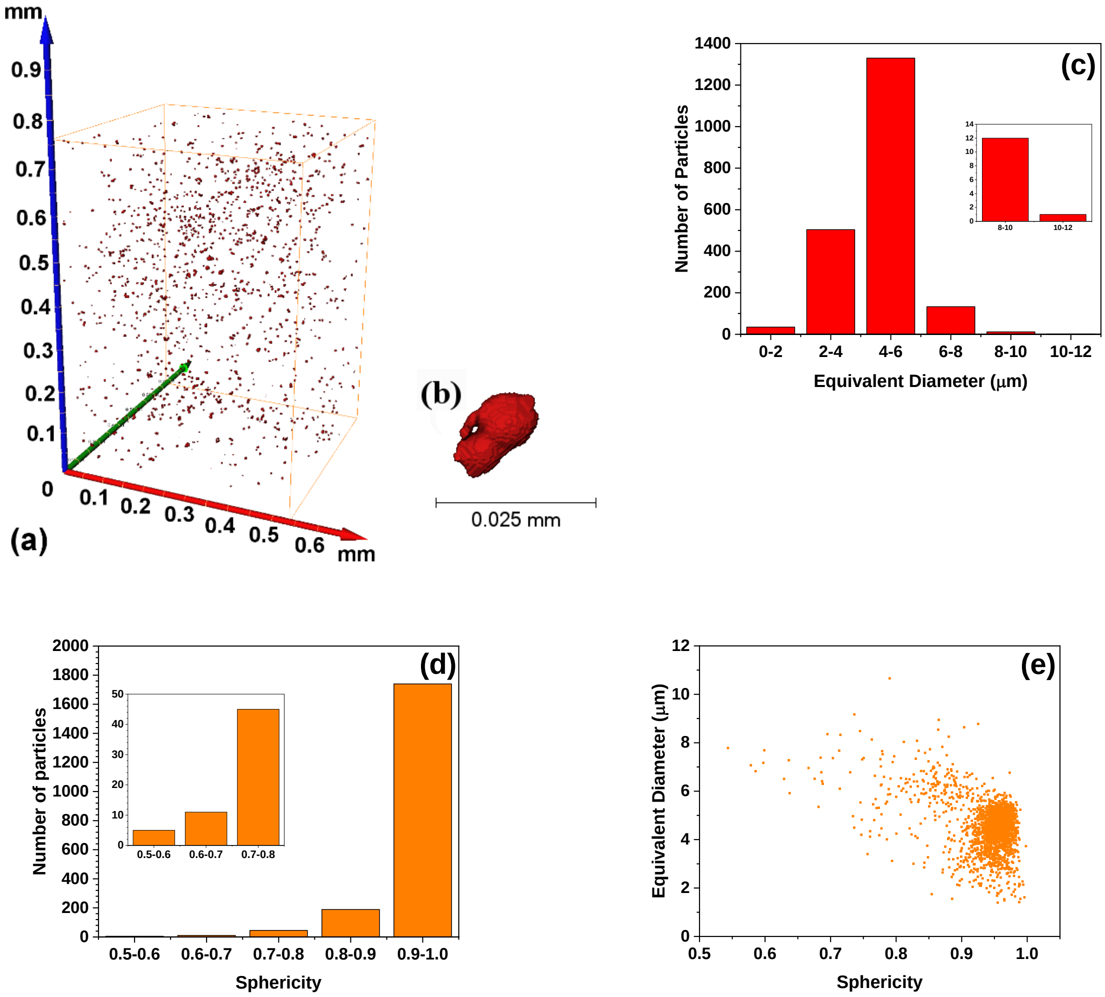

Figure 6.6: XCT and SEM-EDS data for intermetallic particles in Al-Si-Sr alloy. (a) 3D reconstruction of particles in the alloy, (b) Size distribution of the intermetallics, (c) Sphericity of the intermetallics, (d) Relationship of sphericity to the size of the intermetallics, (e) largest particle in alloy.

In this research, these intermetallic particles were also characterised by means of energy dispersive spectroscopy (EDS). Figure 6.7 (a) shows a secondary electron image of an intermetallic particle, and its corresponding EDS maps showing presence of Al, Si, Sr and O elements is presented in figure 6.7 (b-d). When examining the maps the intensity of the colour is representative of the relative intensity of the element. Thus, the black area in the Al map does not mean that there is no Al present but rather that it is much less than in other areas. Furthermore, Si and Sr have overlapping energy lines and thus higher intensity areas of either could simply be wrongly attributed to either element. By using the 'Trumap' method in the Aztec software, a distinction between the two elements could be achieved[42].

Previous research studies indicated that SrO could act as a nucleation site for similar intermetallic particles[40]. The O map shows an area of high O concentration indicating a possibility that this intermetallic particles could have nucleated on a SrO particle.  The stoichiometry of these intermetallic particles is difficult to determine from the SEM-EDS, but by inspecting the Al-Si-Sr ternary phase diagram, it can be inferred that these particles are $Al_2Si_2Sr$ particles[43].

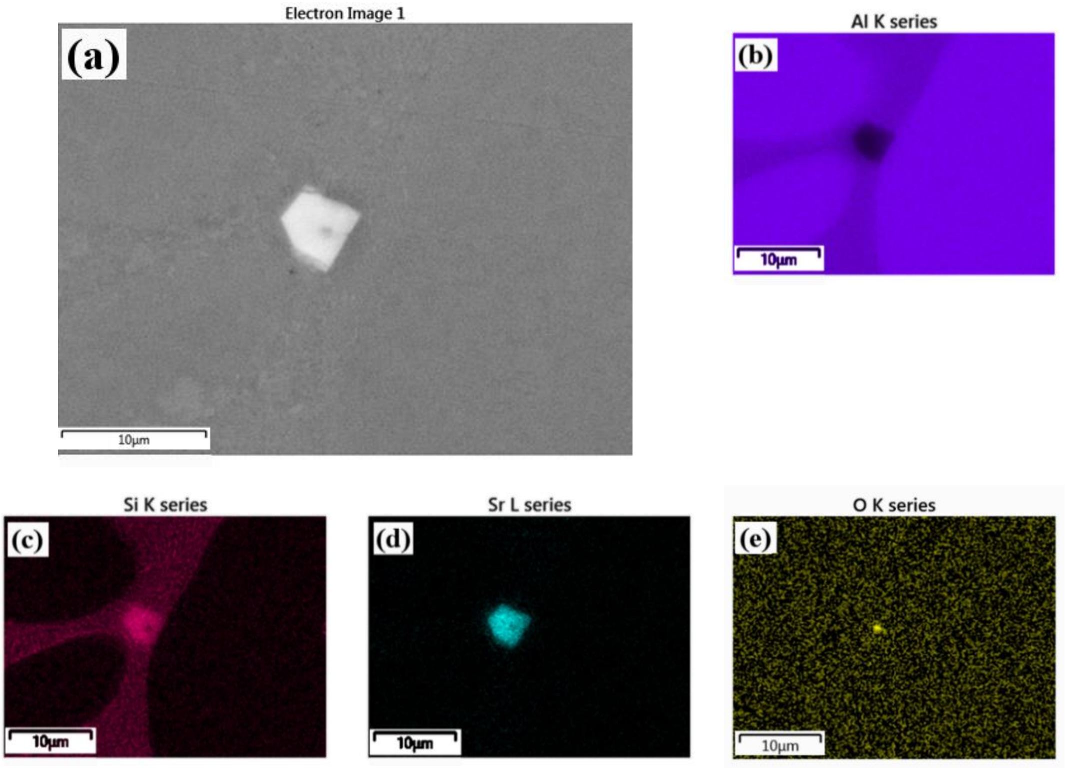

Figure 6.7: SEM-EDS characterisation of intermetallic particle showing (a) SE image, (b) Al EDS map, (c) Si EDS map, (d) Sr EDS map, (e) O EDS map.

Figure 6.8 (a-d) shows the cooling curves obtained by analysing the unmodified and Sr-modified samples. In this figure the eutectic time growth is indicated along the thermal profiles (a and c), whereas a magnified plot on the eutectic transition (b and d) marks the eutectic nucleation temperature, minimum temperature and growth temperature. The major differences between the two cooling curves can be identified in the undercooling phase, which is an indication of the microstructural modification, and the eutectic growth time. This longer eutectic time also provides an extended time for porosity growth. Furthermore, the temperature of formation of the Sr intermetallic could not be determined by using this method. The ternary equilibrium phase diagram of Al-Si-Sr indicates that $Al_2Si_2Sr$ is formed after the primary Al dendrites, however it has also been reported that under non-equilibrium conditions takes place before primary Al solidification[43-47]. The precipitation of Sr intermetallics before and during eutectic solidification could promote pore formation[44].

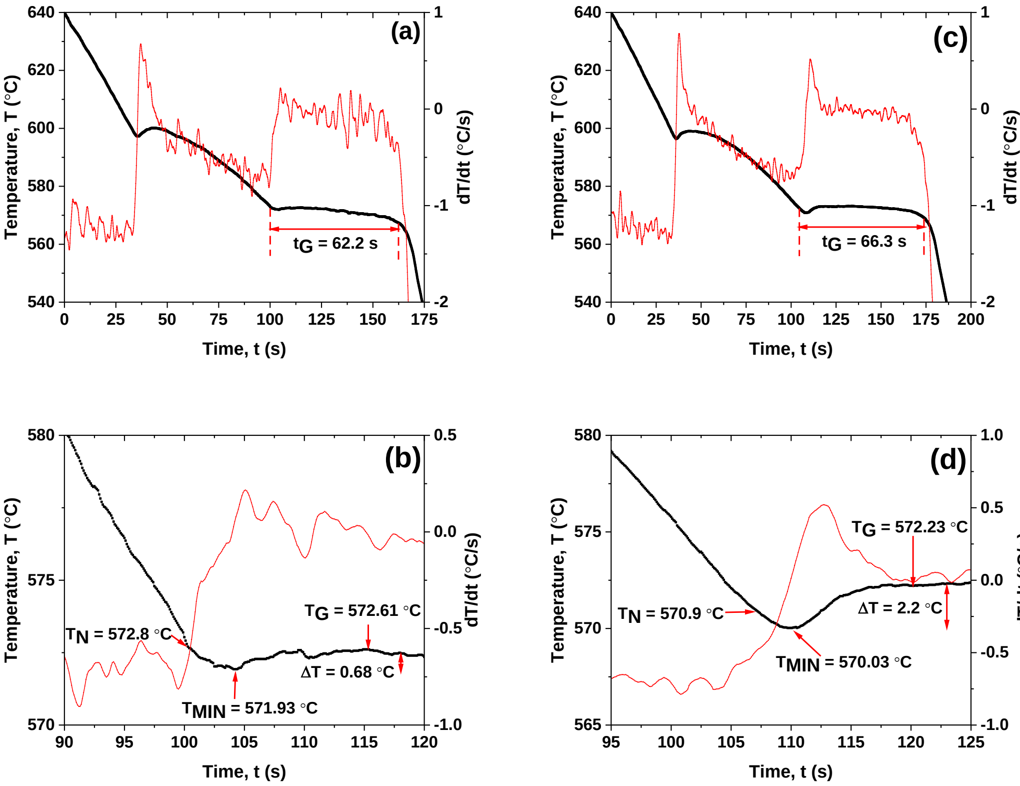

Figure 6.8: Cooling curves showing the (a, c) entire thermal profile and the (b, d) eutectic section for the (a, b) Al-Si and the (c, d) Al-Si-Sr. In these images the time of eutectic growth (tG), the eutectic nucleation temperature (TN), minimum temperature (TMIN), eutectic growth temperature (TG) and eutectic undercooling (ΔT) are indicated.

This study clearly shows that the XCT is a powerful technique in understanding porosity formation in Al-Si alloys. It is evident that the addition of Sr to Al-Si alloys results in increased porosity compared to unmodified alloys as shown in figure 6.1 to figure 6.5 and in table 6.3. The presence of oxides and intermetallic particles could act as heterogeneous nucleation sites for pore formation and depending on the availability of hydrogen present in the melt, the pores grow and form large size pores in the castings. Denton et al.[37] observed that the melt hydrogen content increases upon addition of 0.04%Sr in Al-Si alloys. Samuel et al.[44] observed that the presence of impurities, such as Al-Sr-O or Al-Si-Sr, close to pores and hypothesised that these particles act as heterogeneous nucleation sites for porosity formation, with similar observations found in this study shown in figure 6.2 (b). Further, from differential analysis and cooling curve studies in figure 6.8 it is evident that the undercooling of the melt and eutectic solidification time increased upon addition of Sr to alloy. This increase in solidification time increases the freezing range and length of the mushy zone which ultimately results in an increase in porosity formation in modified alloys. With an increase in solidification time, there is more time for nucleated pore to grow with more hydrogen to diffuse into it. Atwood et al.[5] developed a model for pore nucleation rate as a function of time and found that the increase in undercooling increases the pore nucleation sites. Once the pore nucleated, hydrogen diffuses into them resulting in pore growth and large pore formation. Figure 6.5 clearly shows that the pores in Sr modified alloys are significantly larger in size compared to pores observed in unmodified alloy. Felberbaum et al.[45] studied pore morphology in Al-Cu alloys using XCT and found in their 3D rendering that interdendritic porosity originates from bifilms present in the alloy. Campbell[46] noted that pores can nucleate either from particles or biflims present in the alloy. In this study we have shown that intermetallic particles can nucleate on oxide particles and that these could promote pore formation and growth in Sr modified Al-Si alloys. It is difficult to confirm the role these intermetallic particles have in the increased porosity as the samples studied were solidified alloys. Future studies involving in-situ synchrotron 3D XCT studies during solidification from molten state would further aid in understanding the mechanism of pore nucleation and pore growth in aluminium alloy castings.

## 6.5. Conclusions

X –ray tomography was used to quantify porosity and intermetallic particles in Sr modified Al-Si alloys. The visualisation of pores and intermetallic particles in these alloys was carried out using a high resolution XCT with a voxel size of 390 nm.

- XCT results show that the addition of 400 ppm of Sr to Al-Si alloy resulted in a higher volume fraction of porosity (by over 10%) compared to unmodified alloys. Further it was observed that the average equivalent diameter of pore increased from 2 µm to 18 µm upon addition of Sr.

- The XCT analysis of Sr modified alloy allowed for the analysis of the intermetallic particles present in the Sr-modified alloy. These intermetallic particles occupy a volume fraction of 0.03% and have an average equivalent diameter of 4.5 µm. SEM-EDS analysis confirms the presence and formation of $Al_2Si_2Sr$ type intermetallic compounds in Sr modified Al-Si alloys.
- This study shows that the Sr modification results in the formation of intermetallic particles and the presence of these intermetallic particles enhance porosity in the alloys. Further, it was shown that Sr modification affects undercooling and eutectic temperature which allows more time for already nucleated pore to grow into a large size pore in modified alloys compared to unmodified alloys.

## 6.6. References

1. Polmear, I. J. in *Light Alloys* 205–235 (Elsevier, 2005). doi:10.1016/B978-075066371-7/50008-6
2. Bartley, R. *British and European Aluminium Casting Alloys*. (Association of Light Alloy Refiners, 1996).
3. Hatch, J. E. *Aluminium: Properties and Physical Metallurgy*. (American Society of Metals, 1984).
4. Liao, H. C. *et al.* Effect of Sr addition on porosity formation in directionally solidified A356 alloy. *Int. J. Cast Met. Res.* **26,** 201–208 (2013).
5. Atwood, R. C., Sridhar, S. & Lee, P. D. Equations for nucleation of hydrogen gas pores during solidification of aluminium seven weight percent silicon alloy. *Scr. Mater.* **41,** 1255–1259 (1999).
6. Byczynski, G. E. & Cusinato, D. A. The effects of strontium and grain refiner additions on the fatigue and tensile properties of industrial Al-Si-Cu-Mg alloy castings produced using the Ford Motor Company - Cosworth precision sand process. *Int. J. Cast Met. Res.* **15,** 315–324 (2002).
7. Hetke, A. & Grundlach, R. B. Aluminum casting quality in alloy 356 engine components. *AFS Trans.* **102,** 367–380 (1994).

8. Brosnan, M. & Shivkumar, S. Elevated Temperature Tensile Properties and Fracture Behavior of A356 Castings. *AFS Trans.* **103,** 727–737 (1995).

9. Emadi, D., Gruzleski, J. E. & Toguri, J. M. The effect of Na and Sr modification on surface tension and volumetric shrinkage of A356 alloy and their influence on porosity formation. *Metall. Trans. B* **24,** 1055–1063 (1993).

10. Campbell, J. & Tiryakioğlu, M. Review of effect of P and Sr on modification and porosity development in Al–Si alloys. *Mater. Sci. Technol.* **26,** 262–268 (2010).

11. Fuoco, R., Correa, E. R. & Correa, A. V. O. Effect of modification treatment on microporosity formation in 356 Al alloy. *AFS Trans.* **103,** 379–387 (1995).

12. Fuoco, R., Correa, E. R. & Goldenstein, H. The effect of modification treatment on microporosity formation in 356 Al Alloy, part I: Interdendritic Feeding Evaluation. *AFS Trans.* **104,** 1151–1158 (1996).

13. Fuoco, R., Correa, E. R. & Bastos, M. de A. Effects of Grain Refinement on Feeding mechanisms in A356 Aluminum Alloy. *AFS Trans.* **106,** 401–409 (1998).

14. Groteke, D. E. Influence of SNIF Treatment on Characteristics of Aluminium Foundry Alloys. *AFS Trans.* **93,** 953–960 (1985).

15. Di Sabatino, M., Rørvik, S. & Prestmo, A. The influence of oxide inclusions on the fluidity of Al–7wt.%Si alloy. *Mater. Sci. Eng. A* **413,** 272–276 (2005).

16. Liu, L., Samuel, M., Samuel, F. H., Doty, H. W. & Valtierra, S. The role of Sr oxide on porosity. *AFS Trans.* **110,** 449–462 (2002).

17. Iwahori, H., Yonekura, K., Yamamoto, Y. & Nakamura, M. Occurring Behavior of Porosity and Feeding Capability of Sodium- and Strontium-Modified Al-Si Alloys. *AFS Trans.* **98,** 167–173 (1990).

18. Liu, L., Samuel, A. M., Samuel, F. H., Doty, H. W. & Valtierra, S. Influence of oxides on porosity formation in Sr-treated Al-Si casting alloys. *J. Mater. Sci.* **38,** 1255–1267 (2003).

19. Yi, J. Z., Gao, Y. X., Lee, P. D., Flower, H. M. & Lindley, T. C. Scatter in fatigue life due to effects of porosity in cast A356-T6 aluminum-silicon alloys. *Metall. Mater. Trans. A* **34,** 1879–1890 (2003).

20. Yi, J. Z., Lee, P. D., Lindley, T. C. & Fukui, T. Statistical modeling of microstructure and defect population effects on the fatigue performance of cast A356-T6 automotive components. *Mater. Sci. Eng. A* **432,** 59–68 (2006).

21. Mo, D.-F., He, G.-Q., Hu, Z.-F., Liu, X.-S. & Zhang, W.-H. Effect of microstructural features on fatigue behavior in A319-T6 aluminum alloy. *Mater. Sci. Eng. A* **527,** 3420–3426 (2010).
22. Wang, Q. G., Apelian, D. & Lados, D. A. Fatigue behavior of A356-T6 aluminum cast alloys. Part I. Effect of casting defects. *J. Light Met.* **1,** 73–84 (2001).
23. Jordon, J. B. *et al.* Microstructural Inclusion Influence on Fatigue of a Cast A356 Aluminum Alloy. *Metall. Mater. Trans. A* **41,** 356–363 (2010).
24. Ulbin, M. *et al.* Internal structure characterization of AlSi7 and AlSi10 advanced pore morphology (APM) foam elements. *Mater. Lett.* **136,** 416–419 (2014).
25. Terzi, S. *et al.* In situ study of nucleation and growth of the irregular α-Al/β-Al5FeSi eutectic by 3-D synchrotron X-ray microtomography. *Acta Mater.* **58,** 5370–5380 (2010).
26. Chaijaruwanich, A., Lee, P. D., Dashwood, R. J., Youssef, Y. M. & Nagaumi, H. Evolution of pore morphology and distribution during the homogenization of direct chill cast Al-Mg alloys. *Acta Mater.* **55,** 285–293 (2007).
27. Stephenson, R. S. *et al.* Contrast Enhanced Micro-Computed Tomography Resolves the 3-Dimensional Morphology of the Cardiac Conduction System in Mammalian Hearts. *PLoS One* **7,** e35299 (2012).
28. Kyle, J. R. & Ketcham, R. A. Application of high resolution X-ray computed tomography to mineral deposit origin, evaluation, and processing. *Ore Geol. Rev.* **65,** 821–839 (2015).
29. Dewanckele, J. *et al.* Neutron radiography and X-ray computed tomography for quantifying weathering and water uptake processes inside porous limestone used as building material. *Mater. Charact.* **88,** 86–99 (2014).
30. Li, P. *et al.* X-ray Microtomographic Characterisation of Porosity and its Influence on Fatigue Crack Growth. *Adv. Eng. Mater.* **8,** 476–479 (2006).
31. Lashkari, O., Yao, L., Cockcroft, S. & Maijer, D. X-Ray Microtomographic Characterization of Porosity in Aluminum Alloy A356. *Metall. Mater. Trans. A* **40,** 991–999 (2009).
32. Vanderesse, N., Maire, É., Chabod, A. & Buffière, J.-Y. Microtomographic study and finite element analysis of the porosity harmfulness in a cast aluminium alloy. *Int. J. Fatigue* **33,** 1514–1525 (2011).

33. Nicoletto, G., Konečná, R. & Fintova, S. Characterization of microshrinkage casting defects of Al–Si alloys by X-ray computed tomography and metallography. *Int. J. Fatigue* **41,** 39–46 (2012).
34. Tijani, Y., Heinrietz, A., Stets, W. & Voigt, P. Detection and Influence of Shrinkage Pores and Nonmetallic Inclusions on Fatigue Life of Cast Aluminum Alloys. *Metall. Mater. Trans. A* **44,** 5408–5415 (2013).
35. Sikandar, M., Khiyal, H., Khan, A. & Bibi, A. Modified Watershed Algorithm for Segmentation of 2D Images. **6,** (2009).
36. De Giovanni, M., Warnett, J. M., Williams, M. A., Haribabu, N. & Srirangam, P. X-ray tomography investigation of intensive sheared Al–SiC metal matrix composites. *Mater. Charact.* **110,** 258–263 (2015).
37. Denton, J. R. & Spittle, J. A. Solidification and susceptibility to hydrogen absorption of Al–Si alloys containing strontium. *Mater. Sci. Technol.* **1,** 305–311 (1985).
38. Chuang, C. *et al.* 3D quantitative analysis of graphite morphology in high strength cast iron by high-energy X-ray tomography. *Scr. Mater.* **106,** 5–8 (2015).
39. Fuoco, R., Correa, E. R. & Bastos, M. de A. Microporosity morphology in A356 aluminum alloy in unmodified and modified condition. *AFS Trans.* **109,** 659–677 (2001).
40. Miresmaeili, S. M., Campbell, J., Shabestari, S. G. & Boutorabi, S. M. A. Precipitation of Sr-rich intermetallic particles and their influence on pore formation in Sr-modified A356 alloy. *Metall. Mater. Trans. A* **36,** 2341–2349 (2005).
41. Sigworth, G. K. The Modification of Al-Si Casting Alloys: Important Practical and Theoretical Aspects. *Int. J. Met.* **2,** 19–40 (2008).
42. Oxford Instruments. TruMap: Real time - real results. (2011).
43. Sato, E., Kono, N., Sato, I. & Watanabe, H. Study on the phase diagram of Al-Si-Sr ternary alloy system. *J. Japan Inst. Light Met.* **35,** 71–78 (1985).
44. Samuel, A. M., Doty, H. W., Valtierra, S. & Samuel, F. H. Influence of Oxides on Porosity Formation in Sr-Treated Alloys. *Int. J. Met.* 1–14 (2016). doi:10.1007/s40962-016-0118-3
45. Felberbaum, M., Landry-Désy, E., Weber, L. & Rappaz, M. Effective hydrogen diffusion coefficient for solidifying aluminium alloys. *Acta Mater.*

**59,** 2302–2308 (2011).

46. Campbell, J. *Castings.* (Butterworth-Heinemann, 2003).

# Chapter 7:

# Effect of cerium or yttrium on porosity and intermetallic particles in strontium modified Al-Si alloys: 3D X-Ray tomography study

## Summary

This chapter targets the second objective of this thesis, that is whether porosity in modified alloys can be reduced by adding rare earth elements. In this chapter, 2D optical and 3D X-ray techniques were used to characterise the porosity in fully modified, partly modified and unmodified hypoeutectic. The results from chapter 6 for Sr-modified and unmodified Al-Si alloys are also discussed herein. A comparison of the techniques was undertaken in order to evaluate the suitability of each at carrying out such analysis. An analysis of the shape and size of intermetallics in these alloys was also undertaken.

This work has been partly presented at a conference whilst another section is in preparation for publication. The same people who contributed to the publication presented in chapter 6 have contributed to the work presented in this chapter in almost the same roles. In addition, the author has also contributed to this chapter by analysing the 3D XCT data for the samples presented in this chapter.

*Conference presentation:*
*Effect of Y addition on porosity in Al-Si alloys at the 2018 National Student Conference in Metallic Materials at the University of Sheffield*

*Publication in preparation:*
*Effect of Ce on porosity and intermetallic particles in Strontium modified Al-Si alloys: 3D X-Ray tomography study*

## 7.1. Abstract

Porosity formation in cast alloys is considered to be a major defect in the aluminium casting industry. Al-Si alloys are widely used in the automotive and aerospace industries. In this study the effect of cerium (Ce) or yttrium (Y) modification on porosity and intermetallic formation in Al-Si and Sr-modified Al-Si alloys is investigated using optical microscopy and x-ray tomography techniques. Quantitative information such as average pore size, shape, pore size distribution and intermetallic particle size distribution were evaluated. Optical microscopy results show that the addition of 400 ppm of Sr increases the porosity by 2% in comparison to the unmodified Al-Si alloy. The addition of 1% Ce or Y results in an increase in porosity of approximately 1.25% when compared to the unmodified alloy, which however does not increase significantly with the addition of 400 ppm Sr. XCT has shown that porosity in Al-Si-Ce and Al-Si-Ce-Sr is dominated by shrinkage porosity. In Al-Si-Y-Sr a large gas pore was observed together with smaller shrinkage pores. The relationship between less spherical and larger pores also becomes evident in both alloys. The addition of 1% of Ce or Y results in the formation of intermetallics which occupy approximately 3% of the volume of the alloy.

**Keywords:** Al-Si alloys, Sr modification, Ce modification, Y modification, micro porosity, x-ray tomography.

## 7.2. Introduction

Aluminium-Silicon (Al-Si) alloys are widely used in the automotive, aerospace and casting industries due to their excellent strength to weight ratio, high corrosion resistance, good weldability, excellent mechanical and performance properties[1]. In Al-Si, eutectic silicon appears in the form of needles or platelets which results in poor mechanical properties of these alloys. To reduce this effect these alloys are usually treated with trace level additions of modifying elements such as sodium or strontium[1,2]. Strontium is typically used due to its high retention and low over-modification issues in cast Al-Si alloys. Although strontium modification improves microstructure and mechanical properties[1–3], it also results in a significant increase in porosity that negatively impacts the fatigue properties of cast alloy[4–8].

Emadi et al.[9] list several factors that could lead to an increase in porosity due to strontium modification in Al-Si alloys. These include increase in hydrogen content of the melt, absorption of hydrogen to oxides, decrease in solubility of hydrogen during solidification, depression in eutectic temperature, increase in inclusion content, decrease in surface tension of molten metal and increased volumetric shrinkage of the alloy. Campbell noted that the modification treatment promotes the early formation of pores and depresses the eutectic growth temperature, thus allowing more time for pores to grow further[9,10]. Extensive work by Fuoco et al. indicated that in an unmodified alloy the eutectic liquid flows between interdendritic regions, while in modified alloys the movement of the residual liquid into interdendritic regions is restricted thereby increasing porosity content in the alloys[11–13]. A number of studies have shown that the presence of oxides increases porosity by decreasing the fluidity of the melt[14–18].

Being cast alloys, porosity formation is a great concern as it effects the mechanical and performance properties of these alloys[9]. Understanding the porosity formation can help improve the melt quality, the mechanical properties and reduce hot tearing and wastage of castings. Porosity is partly responsible for initiation of fatigue cracks in castings[19–22]. Previous research has also indicated a direct relationship between pore size and shape to fatigue life of cast components[19,23]. These studies were carried out using conventional microscopy techniques providing 2D microstructural images of pores, which data is used to model and predict the mechanical properties of Al-Si alloys. Since pores will have different shapes and morphologies in different orientations it is essential to visualise and quantify them in 3D to better predict the mechanical properties of these alloys.

Though much research has been carried out to understand the porosity formation in modified alloys, the mechanism is still unclear. It has been previously demonstrated, based on the hydrogen binding energies and the diffusion activation energies of hydrogen atoms in Al and Al-RE phases, that the addition of small amounts of rare-earths can help suppress the porosity in cast Al alloys[24].

X-Ray Computed Tomography (XCT) is a powerful non-destructive technique which provides a three-dimensional (3D) visualisation of internal structure inhomogeneities representative of bulk sample[25–27]. XCT has been applied in numerous fields of research such as medicine[28], geology[29] and civil engineering[30]. In the past several XCT studies were carried out on characterising porosity in Al alloys using XCT and using this data in predicting fatigue properties of these alloys. However, the resolutions obtained in these studies varied between 1.7 – 30 µm[31–35].

In this study a series of Al-Si alloys are investigated by optical microscopy and XCT. The alloys under investigation are unmodified Al-Si, Sr-modified Al-Si, Ce-modified Al-Si, Y-modified Al-Si and Al-Si modified with a combination of either Ce or Y and Sr. Optical microscopy is used to assess the macroporosity in the alloys. Lab-based submicron XCT is employed to assess the shape and size of smaller pores within the casting and this also allows the analysis of the intermetallics within the alloy. The XCT analysis presented in this paper compares the porosity and intermetallics within Al-Si-Ce, Al-SI-Y, Al-Si-Ce-Sr and Al-Si-Y-Sr. A comparison of the porosity in Al-Si and Al-Si-Sr analysed by XCT has already been presented[36]. The results from this article are also discussed in relation of the results presented here.

## 7.3. Experimental Methods

### 7.3.1. Alloy preparation

Al-Si alloy was prepared by melting 99.999% purity aluminium (NewMet, UK) in a clay graphite crucible using a Carbolite RHF1500 high temperature chamber furnace. High purity (99.999%) silicon (Alfa Aeser, UK) was added to the molten aluminium and stirred to ensure mixing of silicon in the melt. Once the silicon dissolved in the melt, the mixture was poured into a graphite cylindrical mould (12 mm diameter, 85 mm deep). A portion of the Al-Si alloy was then used to prepare Al-Si-Sr, Al-Si-Ce, Al-Si-Y, Al-Si-Ce-Sr and Al-Si-Y-Sr alloys. When the Al-Si alloy was in a molten state, the Al-10Sr (wt%) and/or the Al-10Ce (wt%) or the Al-

10Y (wt%) master alloy were added to the melt, and returned to the same mould. The cooling rate was approximately 75 °C/s. For XCT measurements, samples with a diameter of 1 mm were machined from the centre of the castings using wire electric discharge machining (EDM). Table 7.1 below presents the composition analysis performed by inductively coupled plasma optical emission spectroscopy (ICP-OES).

Table 7.1: ICP-OES chemical composition analysis performed on the six alloys in weight percentage (wt%).

| | **Al** | **Si** | **Ce** | **Sr** | **Fe** | **Cu** | **Mn** |
|---|---|---|---|---|---|---|---|
| **Al-Si** | Balance | 8.82 | - | <0.01 | <0.01 | <0.01 | <0.01 |
| **Al-Si-Sr** | Balance | 8.78 | - | 0.02 | <0.01 | <0.01 | <0.01 |
| **Al-Si-Ce** | Balance | 7.62 | 1.17 | <0.01 | <0.01 | <0.01 | <0.01 |
| **Al-Si-Ce-Sr** | Balance | 7.40 | 1.07 | 0.03 | <0.01 | <0.01 | <0.01 |
| **Al-Si-Y** | Balance | 7.75 | 1.09 | <0.01 | <0.01 | <0.01 | <0.01 |
| **Al-Si-Y-Sr** | Balance | 7.39 | 0.83 | 0.03 | <0.01 | <0.01 | <0.01 |

### 7.3.2. Optical microscopy analysis

Cross-sections were taken from the castings and imaged using an Alicona InfiniteFocus optical microscope. The images acquired were then analysed by using ImageJ software.

### 7.3.3. X-Ray computed tomography

XCT measurements were performed using the Zeiss Versa 520 system. The cylindrical samples with 1 mm diameter were mounted on the rotating stage in the XCT machine. As the sample is exposed to x-rays, the x-rays are either attenuated or pass through the sample resulting in a grey-scale radiograph on the detector screen. Numerous radiographic projections obtained through a 360 degree rotation were then reconstructed into a 3D volume through the process of filtered back projection. The volume consisted of a number of 3D pixels called voxels with an associated grey value between 0 and 65535, proportional to the attenuation of the material.

Table 7.2: X-Ray tomography scanning parameters

| | |
|---|---|
| Voltage (kV) | 100 |
| Power (W) | 9 |
| Exposure (s) | 10 |
| Filter ($SiO_2$, mm) | 0.15 |
| Number of Projections | 3201 |
| Voxel size (nm) | 310 |

The XCT scan parameters are given in table 7.2. In the scans for this study, a 10x optic was used in combination with a 2000 * 2000 pixel detector. This resulted in a 310 nm voxel size in the reconstructed volume. The imaged volumes were segmented using a watershed based algorithm in Avizo 9.3 (FEI, USA)[37]. The principles of image segmentation and XCT operation can be found in an earlier publication[38].

## 7.4. Results and Discussion

Figure 7.1 shows the optical images (a, c, e, g, i, k) of Al-Si, Al-Si-Sr, Al-Si-Ce, Al-Si-Y, Al-Si-Ce-Sr and Al-Si-Y-Sr modified alloys and the corresponding size distribution analysis (b, d, f, h, j, l). It is clearly evident that there is significantly less porosity in the unmodified Al-Si in figure 7.1 (a) in comparison to the other five alloys figure 7.1 (c, e, g, i, k). The size distribution analysis confirms this observation as Al-Si (figure 7.1b) is shown to contain few pores, mostly with an equivalent diameter <100 µm. On the other hand much larger pore numbers can be observed in the other five alloys. In Al-Si-Sr (figure 7.1d) over 500 pores were measured with most measuring an equivalent diameter <150 µm, though 32 pores had an equivalent diameter >200 µm. Figure 7.1 (f) shows the size analysis performed on Al-Si-Ce. In this case over 700 pores were analysed, however most of these had an equivalent diameter <100 µm. Figure 7.1 (g) shows a similar size analysis done on Al-Si-Y, where a large number of pores, over 1600, was observed, though most of these had an equivalent diameter <50 µm. Alloys Al-Si-Ce-Sr (figure

7.1i) and Al-Si-Y-Sr (figure 7.1l) showed very similar results, both presenting over 1000 pores, and a similar distribution in which most of the pores had an equivalent diameter <50 µm.

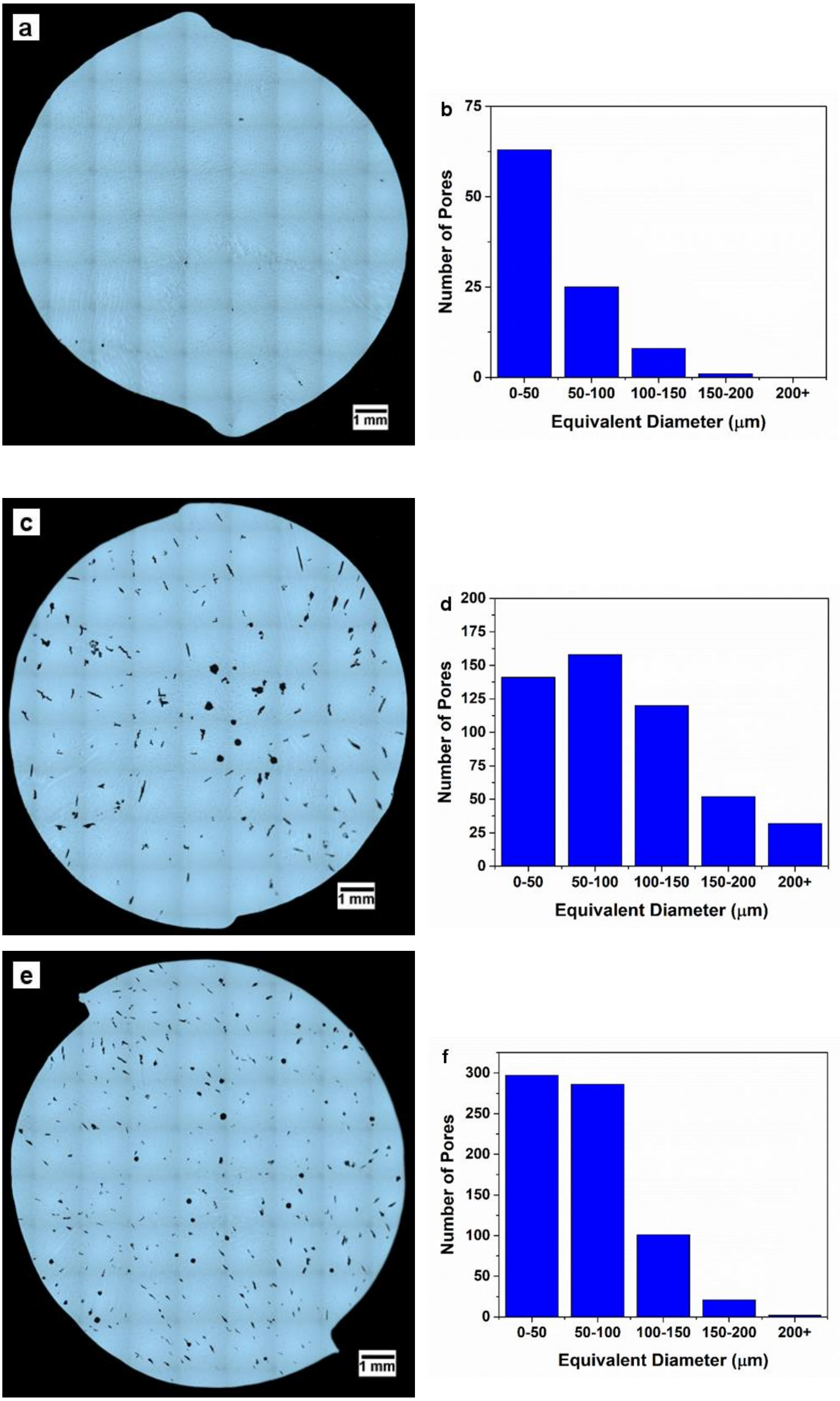
a
1 mm
b
75
50
25
0
Number of Pores
0-50
50-100
100-150
150-200
200+
Equivalent Diameter (μm)
c
1 mm
d
200
175
150
125
100
75
50
25
0
Number of Pores
0-50
50-100
100-150
150-200
200+
Equivalent Diameter (μm)
e
1 mm
f
300
250
200
150
100
50
0
Number of Pores
0-50
50-100
100-150
150-200
200+
Equivalent Diameter (μm)

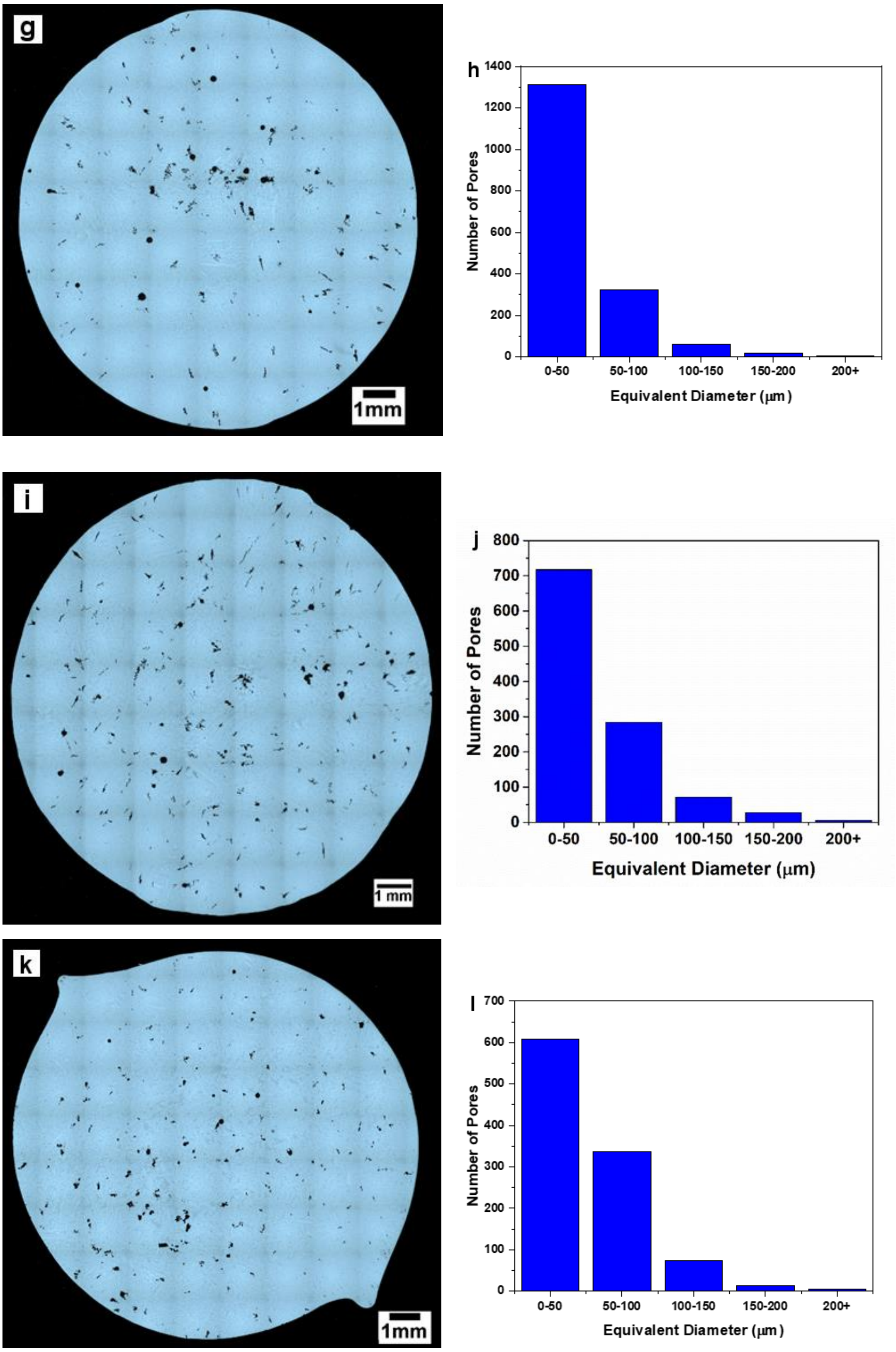

Figure 7.1: Optical microscopy images and size distribution analysis of (a,b) Al-Si, (c,d) Al-Si-0.04Sr, (e,f) Al-Si-Ce, (g,h) Al-Si-Y, (i,j) Al-Si-Ce-Sr and (k,l) Al-Si-Y-Sr.

Table 7.3 highlights the quantified size analysis on macro porosity due to the addition of Ce or Y and/or Sr modification elements. It can be immediately noted how the largest increase in percentage porosity is in the Sr-modified alloy, whilst the Ce-containing and Y-containing samples seem to have significantly lower percentage porosity even in the presence of Sr, in comparison to Al-Si-Sr.

Table 7.3: Quantitative information of porosity in Al-Si, Al-Si-Sr, Al-Si-Ce, Al-Si-Ce-Sr, Al-Si-Y and Al-Si-Y-Sr alloys obtained from examining optical microscopy images.

| | **Al-Si** | **Al-Si-Sr** | **Al-Si-Ce** | **Al-Si-Y** | **Al-Si-Ce-Sr** | **Al-Si-Y-Sr** |
|---|---|---|---|---|---|---|
| Percentage porosity (%) | 0.1 | 2.11 | 1.29 | 1.22 | 1.32 | 1.22 |
| Average pore equivalent diameter (µm) | 40.76 | 91.03 | 60.22 | 35.05 | 44.13 | 46.81 |
| Largest pore equivalent diameter (µm) | 167.37 | 380.98 | 309.02 | 254.82 | 439.92 | 259.77 |
| Number of pores | 98 | 507 | 708 | 1717 | 1101 | 1039 |

Figure 7.2 (a, b, c, d) show XY ortho slices in Al-Si-Ce, Al-Si-Y, Al-Si-Ce-Sr and Al-Si-Y-Sr alloy samples respectively from XCT measurements. The scanned samples were taken from the centre of the alloy castings where it is known that porosity is higher[39]. A similar XCT analysis to that being presented here, on Al-Si and Al-Si-Sr has already been published[36]. From these slices it can be noted that in Al-Si-Ce a section of a large pore is present on the edge of the sample. This was probably a much larger pore which had been cut through during the machining of the sample. In Al-Si-Y no pores can be seen. In Al-Si-Ce-Sr some shrinkage porosity can be noted towards the edge of the slice, whilst in Al-Si-Y-Sr a large circular pore can be observed. Intermetallics can be seen spread out throughout all samples. It can also be observed that in Al-Si-Ce and Al-Si-Y-Sr, the intermetallics seem to be

agglomerated, whereas in Al-Si-Y and in Al-Si-Ce-Sr these seem to be more evenly distributed. Figure 7.2 (e, f, g, h) represents the complete three-dimensional reconstructions of porosity and intermetallic particles in Al-Si-Ce, Al-Si-Y, Al-Si-Ce-Sr and Al-Si-Y-Sr respectively. The green, blue and red colours in figure 7.2 (e, f, g, h) represents the Al matrix, porosity and intermetallic particles in the cast alloys respectively.

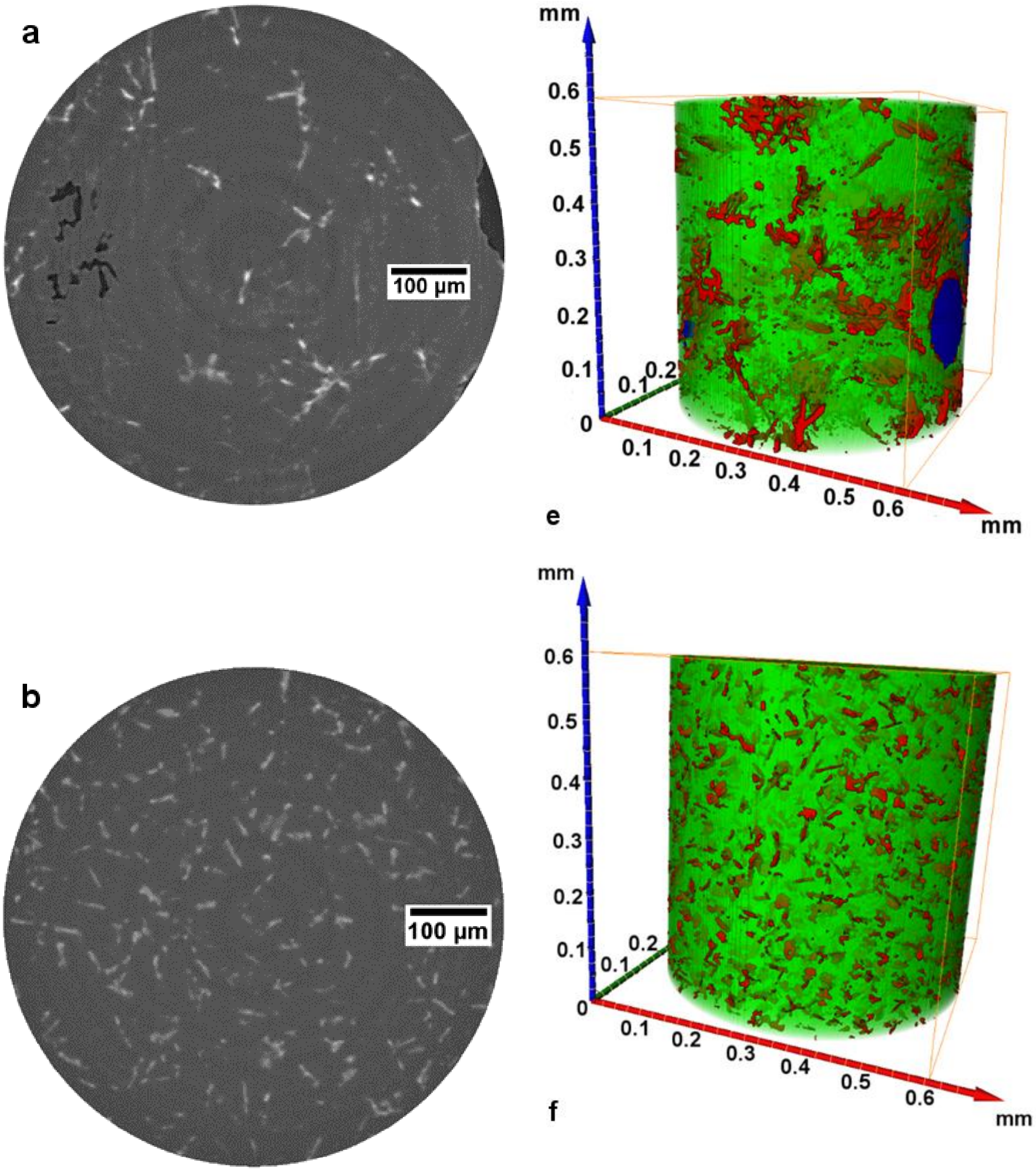

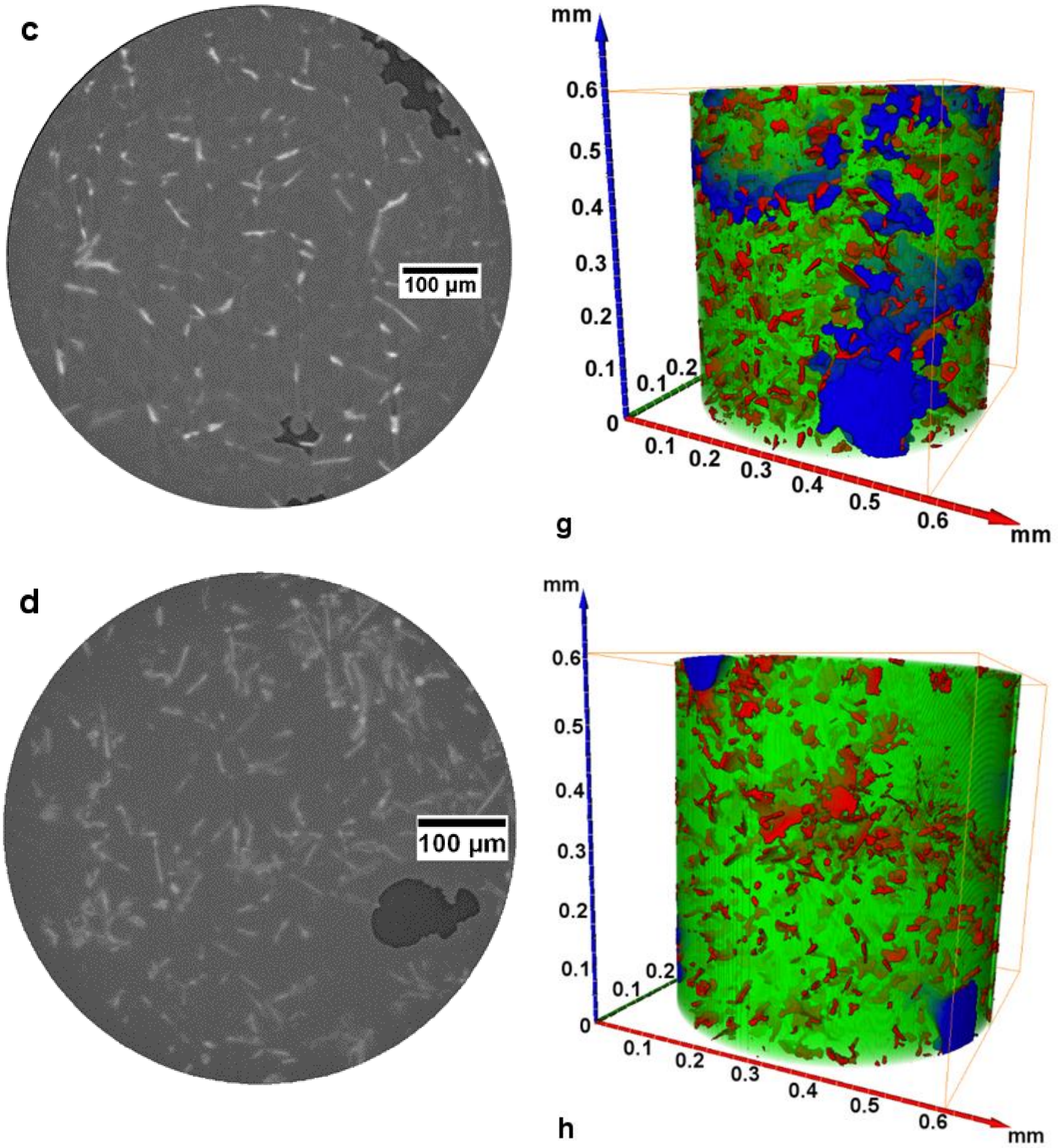

Figure 7.2: XY ortho slices (a-d) and full 3D reconstructed images (e-h) of (a,e) Al-Si-Ce, (b,f) Al-Si-Y, (c,g) Al-Si-Ce-Sr and (d,h) Al-Si-Y-Sr. In the 3D reconstructed images the matrix is shown in green, pores in blue and particles in red.

In figure 7.3 and figure 7.4 the Al matrix and intermetallic particles are removed from the image for easier visualisation of the pores. Figure 7.3 (a, b) compares the porosity in Al-Si-Ce and Al-Si-Y alloys whilst figure 7.4 (a, b) compares these two alloys after a further Sr addition. It can be noted that Al-Si-Ce (figure 7.3a) contains two large pores on the edge of the sample. Some smaller shrinkage porosity is also observed towards the centre of the sample, with smaller pores scattered around. On the other hand the Al-Si-Y (figure 7.3b) presents only one small pore at the top of the analysed volume. This could either be a small section of a larger pore that has been cut out by the machining process or a machining defect. This result indicates the importance of combining the two techniques, 2D and 3D, to evaluate the porosity in such alloys. This also shows that the porosity is not homogenous in the alloy. Figure 7.3 (c and d) also shows the largest pore present in these two samples. In the Al-Si-Ce (figure 7.3 c), the largest pore happens to be on the boundary of the sample. The shape of the pore seems to indicate that the original pore would have been a large spherical pore indicative of gas porosity. However, this might not necessarily be the case as the weakened structure of a shrinkage pore might have fallen out leaving behind what seems to be a part of a sphere. Not much information can be gathered from the largest pore in the Al-Si-Y alloy (figure 7.3 d).

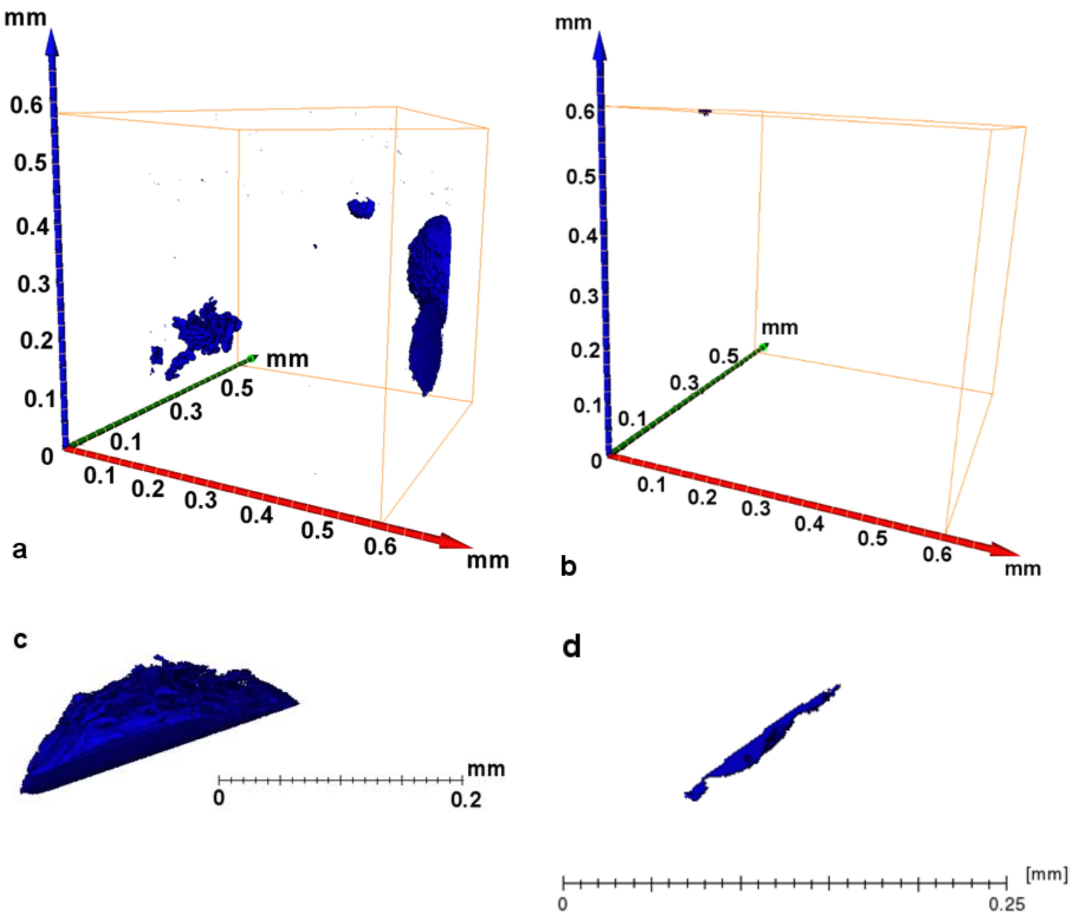

Figure 7.3: 3D reconstruction of pores from XCT data in (a) Al-Si-Ce and (b) Al-Si-Y. Largest pore in (c) Al-Si-Ce and (d) Al-Si-Y.

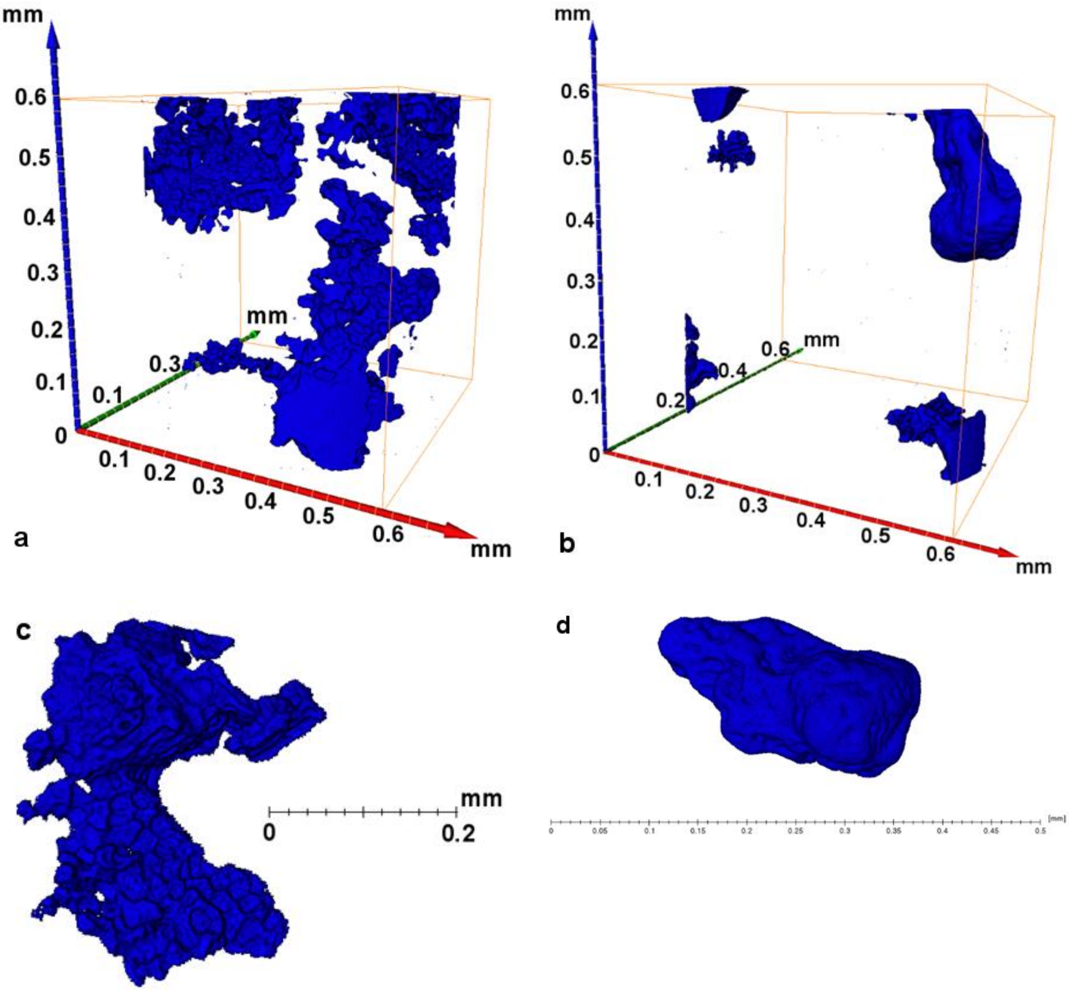

Figure 7.4: 3D reconstruction of pores frm XCT data in (a) Al-Si-Ce-Sr and (b) Al-Si-Y-Sr. Largest pore in (c) Al-Si-Ce-Sr and (d) Al-Si-Y-Sr.

Figure 7.4 shows the 3D XCT reconstruction in Al-Si-Ce-Sr (a) and Al-Si-Y-Sr (b) alloys. In Al-Si-Ce-Sr the porosity is dominated by large shrinkage pores, whilst in Al-Si-Y-Sr the reconstruction is dominated by a large gas pore and some shrinkage porosity. The largest pore in the Al-Si-Ce-Sr (figure 7.4 c) has a complex geometry and has a shape typical of shrinkage porosity as it shows the inter-dendritic shape resulting from lack of mass feeding. This kind of dendritic arm impingement on the pore has previously been reported in Al-Si alloys with Si content (<10%) in the alloys[40].

In all four alloys imaged it can be noted that some of the pores are in contact with the edge of the boundary box. This suggests that these pores extend beyond the boundary box and thus it is likely that the sizes of these pores is underestimated.

To assess the porosity shape and size distribution in unmodified and modified alloys, XCT data was analysed using Avizo and is presented in figure 7.5, comparing Al-Si-Ce, Al-Si-Ce-Sr and Al-Si-Y-Sr. Al-Si-Y is not included in this analysis as only one pore (equivalent diameter 9.87 µm; sphericity 0.36) was detected. Figure 7.5 (a, b, c) shows clearly that the size distribution in Al-Si-Ce and Al-Si-Ce-Sr alloys is similar, with the exception of the large pores (> 5 µm) which seem to be more frequent in the Al-Si-Ce-Sr. The number of pores in Al-Si-Y-Sr is significantly lower than the other two alloys. These observations are supported by the fact that the average pore equivalent diameter is approximately 3 times higher in the Al-Si-Ce-Sr than it is in the Al-Si-Ce. In order to understand the shape change of pores due to Sr addition, sphericity calculations were performed using equation 2. Sphericity is a measure of how spherical a feature is. A sphericity value of 1 represents a perfect spherical shape of the pore[41].

$$\Psi = \frac{\pi^{\frac{1}{3}}(6V_p)^{\frac{2}{3}}}{A_p} \qquad (2)$$

In equation 2, $\Psi$ represents the sphericity, Vp represents the volume of a pore, $A_p$ represents the area of a pore. Figure 7.5 (d, e, f) shows the variation of sphericity with the volume of the porosity. In all cases a clear observation can be made that larger pores become less spherical.

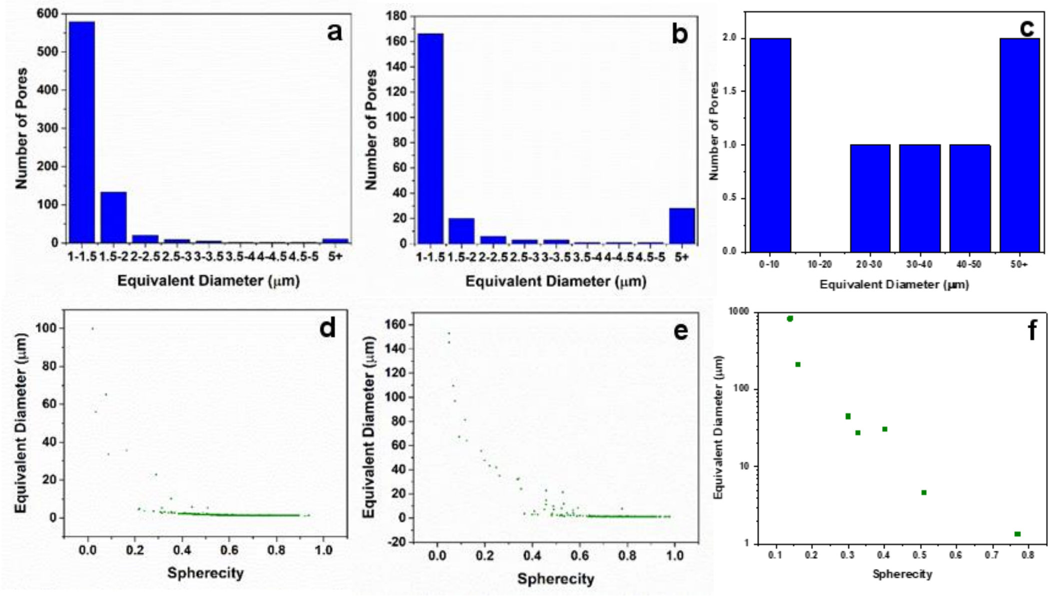

Figure 7.5: Data obtained from XCT for (a, d) Al-Si-Ce, (b, e) Al-Si-Ce-Sr alloy and (c, f) Al-Si-Y-Sr. (a, b, c) Size distribution of porosity, (d, e, f) relationship of sphericity to the size of the pores.

A numerical comparison of the porosity is given in table 7.4. For easy reference the values from the previous publication investigating the effect of Sr on the porosity in Sr-modified Al-Si are presented in this table as well[36]. It is clear from table 7.4 that the XCT has detected much lower porosity in Al-Si-Ce compared to Al-Si-Ce-Sr. However, one must be aware of the difficulty to assess the overall porosity of a sample by looking at such a small volume within a casting. The average pore equivalent diameter and maximum pore diameter are also higher in Al-Si-Ce-Sr. Both Al-Si-Ce and Al-Si-Ce-Sr values sit in between Al-Si and Al-Si-Sr, except for the average pore equivalent diameter of Al-Si-Ce, which was calculated to be lower than in Al-Si. However, a population of extremely small pores was noted in this sample, thus shifting the average to lower values. The maximum pore equivalent diameter is still much higher compared to Al-Si. On the other hand no small sized pores were detected in either Al-Si-Y or Al-Si-Y-Sr. This resulted in the average size of pores in Al-Si-Y-Sr being very large compared to the other samples. Furthermore one of the pores detected was an extremely large gas pore which skewed the results further to higher values. Only one small sized pore was detected at the edge of the Al-Si-Y sample which does not allow for comparison with the rest of the samples. It must be specified that the Al-Si-Y and Al-Si-Y-Sr samples were analysed together and the lack of detection of the smaller pores is probably due to instrument error.

Table 7.4: Quantitative information of porosity in Al-Si-Ce, Al-Si-Y and Al-Si-Ce-Sr alloys compared with Al-Si and Al-Si-Sr taken from [36].

| | **Al-Si** | **Al-Si-Sr** | **Al-Si-Ce** | **Al-Si-Y** | **Al-Si-Ce-Sr** | **Al-Si-Y-Sr** |
|---|---|---|---|---|---|---|
| Total volume analysed ($mm^3$) | 0.290 | 0.336 | 0.209 | 0.228 | 0.212 | 0.234 |
| Pore percentage (%) | 0.00006 | 11.10 | 0.39 | 0.00002 | 2.61 | 1.98 |
| Average pore equivalent diameter (µm) | 2.03 | 18.30 | 1.82 | 9.87 | 6.35 | 163.67 |
| Maximum pore equivalent diameter (µm) | 3.94 | 381 | 99.96 | 9.87 | 152.90 | 825.47 |

Figure 7.6 and figure 7.7 show the presence and quantification of intermetallic particles in Al-Si-Ce, Al-Si-Y, Al-Si-Ce-Sr and Al-Si-Y-Sr. The 3D reconstructions of these particles within the alloys is shown in figure 7.6 and figure 7.7 (a and b). It can be noted that these intermetallics are spread throughout the sample. Figure 7.6 and figure 7.7 (c and d) show the largest intermetallic particle in the different alloys. These show the presence of large agglomerates in Al-Si-Ce and Al-Si-Y-Sr. Figure 7.6 and figure 7.7 (e and f) show the size distribution of the intermetallic particles. It can be noted that the smallest intermetallics measured were in Al-Si-Y, whilst the largest ones were found in Al-Si-Ce and Al-Si-Y-Sr, due to the large agglomerates that were measured.

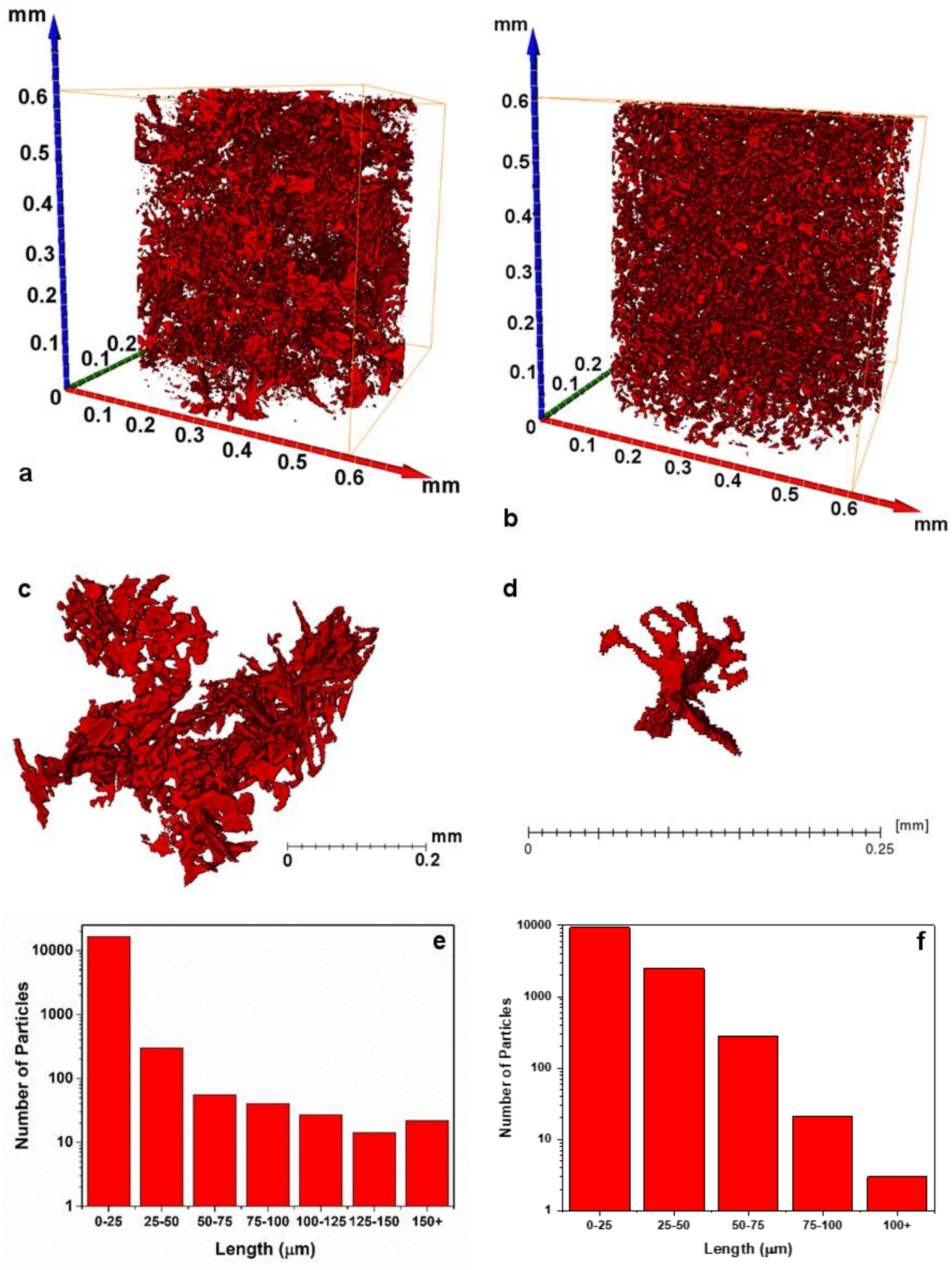

Figure 7.6: 3D reconstruction of particles from XCT data in (a) Al-Si-Ce and (b) Al-Si-Y, the largest particle in (c) Al-Si-Ce and (d) Al-Si-Y, and the size distribution of the intermetallics in (e) Al-Si-Ce and (f) Al-Si-Y.

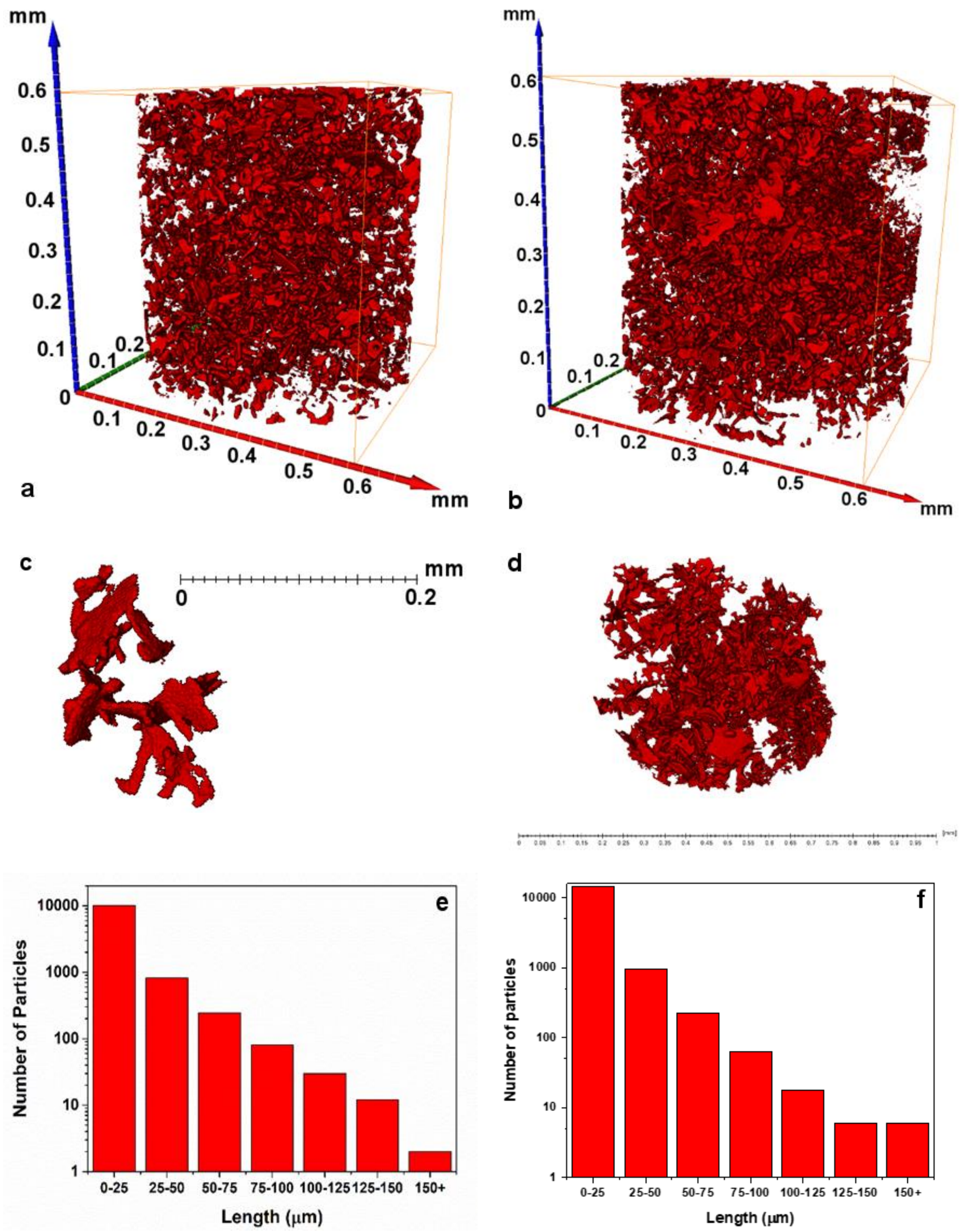

Figure 7.7: 3D reconstruction of particles from XCT data in (a) Al-Si-Ce-Sr and (b) Al-Si-Y-Sr, the largest particle in (c) Al-Si-Ce-Sr and (d) Al-Si-Y-Sr, and the size distribution of the intermetallics in (e) Al-Si-Ce-Sr and (f) Al-Si-Y-Sr.

Table 7.5 summarizes the information extracted from the particle analysis. The difference in the dimensions of the intermetallics between the different samples is more evident. The maximum intermetallic length in Al-Si-Y and Al-Si-Ce-Sr is relatively similar, whilst much larger particles were measured in Al-Si-Ce and Al-Si-Y-Sr.

Table 7.5: Quantitative information of intermetallic particles in Al-Si-Ce, Al-Si-Y, Al-Si-Ce-Sr and Al-Si-Y-Sr alloys.

| | **Al-Si-Ce** | **Al-Si-Y** | **Al-Si-Ce-Sr** | **Al-Si-Y-Sr** |
|---|---|---|---|---|
| Particle percentage (%) | 3.12 | 2.36 | 2.78 | 4.08 |
| Average intermetallic length (µm) | 6.91 | 14.20 | 9.64 | 7.44 |
| Maximum intermetallic length (µm) | 494.98 | 120.4 | 188.22 | 678.53 |

XRD spectra were previously presented in chapters 2 and 3 and show that the intermetallic composition is $Al_2Si_2Ce$ or $Al_2Si_2Y$. There was no indication that the addition of Sr changed the chemical composition of the intermetallics or introduced new ones, such as $Al_2Si_2Sr$ which was presented earlier for Sr-modified Al-Si[36]. However, this could be due to the Al-Si-Ce or Al-Si-Y intermetallics overshadowing the presence of the much smaller Al-Si-Sr intermetallics.

In this study XCT has been combined with optical microscopy in order to fully assess the porosity within a casting. This could also be done by analysing a number of samples for each casting or analyse larger samples in an XCT, however due to the way XCT acquires data a larger sample would result in a lower resolution, and a larger number of samples would increase the time required for a full analysis. From the optical microscopy investigation it is evident that the addition of Sr to Al-Si results in increased porosity compared to unmodified alloys. The addition of Ce or Y also increases the porosity albeit to a lesser extent, and this happens also when Sr was added with Ce or Y in Al-Si. The XCT gives further information about the porosity shape and features. XCT has also allowed the analysis of the intermetallic particles. This analysis has shown that following 1% addition of a rare earth element, a volume fraction of approximately 3% forms within the alloy. It has been previously hypothesized that the presence of oxides and intermetallic particles could act as heterogeneous nucleation sites for pore formation and depending on the availability of hydrogen present in the melt, the pores grow and form large size pores in the castings[36]. However, in this case, due to the relatively large size of and the high volume percentage occupied by intermetallic particles, this hypothesis could not be addressed.

## 7.5. Conclusions

- Optical microscopy and x-ray tomography were used to quantify porosity and intermetallic particles in Al-Si alloys which were modified by Ce or Y and/or Sr. The visualisation of pores and intermetallic particles in these alloys was carried out using a high resolution XCT with a voxel size of 310 nm.
- Optical microscopy results have shown that Sr drastically increases the presence of porosity in Al-Si alloys. The addition of Ce or Y also increases the porosity, albeit to a lesser extent. The combination of Ce or Y and Sr results in a porosity percentage which is approximately the same as the one where only Ce was added. This indicates that the presence of Ce or Y could potentially reduce the porosity in Sr-modified Al-Si castings.
- XCT results show that the alloys investigated are all characterised by shrinkage porosity, though a large gas pore was observed in Al-Si-Y-Sr alloy. Furthermore, by comparing the quantification results from XCT and optical microscopy, the importance of exercising caution when evaluating the results from such small samples is highlighted.
- The XCT analysis also allowed for the analysis of the intermetallic particles. These intermetallic particles occupy a volume fraction of around 3% in all alloys.

## 7.6. References

1. Polmear, I. J. in *Light Alloys* 205–235 (Elsevier, 2005). doi:10.1016/B978-075066371-7/50008-6
2. Bartley, R. *British and European Aluminium Casting Alloys*. (Association of Light Alloy Refiners, 1996).

3. Hatch, J. E. *Aluminium: Properties and Physical Metallurgy*. (American Society of Metals, 1984).
4. Liao, H. C. *et al.* Effect of Sr addition on porosity formation in directionally solidified A356 alloy. *Int. J. Cast Met. Res.* **26,** 201–208 (2013).
5. Atwood, R. C., Sridhar, S. & Lee, P. D. Equations for nucleation of hydrogen gas pores during solidification of aluminium seven weight percent silicon alloy. *Scr. Mater.* **41,** 1255–1259 (1999).
6. Byczynski, G. E. & Cusinato, D. A. The effects of strontium and grain refiner additions on the fatigue and tensile properties of industrial Al-Si-Cu-Mg alloy castings produced using the Ford Motor Company - Cosworth precision sand process. *Int. J. Cast Met. Res.* **15,** 315–324 (2002).
7. Hetke, A. & Grundlach, R. B. Aluminum casting quality in alloy 356 engine components. *AFS Trans.* **102,** 367–380 (1994).
8. Brosnan, M. & Shivkumar, S. Elevated Temperature Tensile Properties and Fracture Behavior of A356 Castings. *AFS Trans.* **103,** 727–737 (1995).
9. Emadi, D., Gruzleski, J. E. & Toguri, J. M. The effect of Na and Sr modification on surface tension and volumetric shrinkage of A356 alloy and their influence on porosity formation. *Metall. Trans. B* **24,** 1055–1063 (1993).
10. Campbell, J. & Tiryakioğlu, M. Review of effect of P and Sr on modification and porosity development in Al–Si alloys. *Mater. Sci. Technol.* **26,** 262–268 (2010).
11. Fuoco, R., Correa, E. R. & Correa, A. V. O. Effect of modification treatment on microporosity formation in 356 Al alloy. *AFS Trans.* **103,** 379–387 (1995).
12. Fuoco, R., Correa, E. R. & Goldenstein, H. The effect of modification treatment on microporosity formation in 356 Al Alloy, part I: Interdendritic Feeding Evaluation. *AFS Trans.* **104,** 1151–1158 (1996).
13. Fuoco, R., Correa, E. R. & Bastos, M. de A. Effects of Grain Refinement on Feeding mechanisms in A356 Aluminum Alloy. *AFS Trans.* **106,** 401–409 (1998).
14. Groteke, D. E. Influence of SNIF Treatment on Characteristics of Aluminium Foundry Alloys. *AFS Trans.* **93,** 953–960 (1985).
15. Di Sabatino, M., Rørvik, S. & Prestmo, A. The influence of oxide inclusions on the fluidity of Al–7wt.%Si alloy. *Mater. Sci. Eng. A* **413,** 272–276 (2005).

16. Liu, L., Samuel, M., Samuel, F. H., Doty, H. W. & Valtierra, S. The role of Sr oxide on porosity. *AFS Trans.* **110,** 449–462 (2002).
17. Iwahori, H., Yonekura, K., Yamamoto, Y. & Nakamura, M. Occurring Behavior of Porosity and Feeding Capability of Sodium- and Strontium-Modified Al-Si Alloys. *AFS Trans.* **98,** 167–173 (1990).
18. Liu, L., Samuel, A. M., Samuel, F. H., Doty, H. W. & Valtierra, S. Influence of oxides on porosity formation in Sr-treated Al-Si casting alloys. *J. Mater. Sci.* **38,** 1255–1267 (2003).
19. Yi, J. Z., Gao, Y. X., Lee, P. D., Flower, H. M. & Lindley, T. C. Scatter in fatigue life due to effects of porosity in cast A356-T6 aluminum-silicon alloys. *Metall. Mater. Trans. A* **34,** 1879–1890 (2003).
20. Yi, J. Z., Lee, P. D., Lindley, T. C. & Fukui, T. Statistical modeling of microstructure and defect population effects on the fatigue performance of cast A356-T6 automotive components. *Mater. Sci. Eng. A* **432,** 59–68 (2006).
21. Mo, D.-F., He, G.-Q., Hu, Z.-F., Liu, X.-S. & Zhang, W.-H. Effect of microstructural features on fatigue behavior in A319-T6 aluminum alloy. *Mater. Sci. Eng. A* **527,** 3420–3426 (2010).
22. Wang, Q. G., Apelian, D. & Lados, D. A. Fatigue behavior of A356-T6 aluminum cast alloys. Part I. Effect of casting defects. *J. Light Met.* **1,** 73–84 (2001).
23. Jordon, J. B. *et al.* Microstructural Inclusion Influence on Fatigue of a Cast A356 Aluminum Alloy. *Metall. Mater. Trans. A* **41,** 356–363 (2010).
24. Hua, G., Ahmadi, H., Nouri, M. & Li, D. Positive effect of yttrium on the reduction of pores in cast Al alloy. *Mater. Chem. Phys.* **149–150,** 140–144 (2015).
25. Ulbin, M. *et al.* Internal structure characterization of AlSi7 and AlSi10 advanced pore morphology (APM) foam elements. *Mater. Lett.* **136,** 416–419 (2014).
26. Terzi, S. *et al.* In situ study of nucleation and growth of the irregular α-Al/β-Al5FeSi eutectic by 3-D synchrotron X-ray microtomography. *Acta Mater.* **58,** 5370–5380 (2010).
27. Chaijaruwanich, A., Lee, P. D., Dashwood, R. J., Youssef, Y. M. & Nagaumi, H. Evolution of pore morphology and distribution during the homogenization of direct chill cast Al-Mg alloys. *Acta Mater.* **55,** 285–293 (2007).

28. Stephenson, R. S. *et al.* Contrast Enhanced Micro-Computed Tomography Resolves the 3-Dimensional Morphology of the Cardiac Conduction System in Mammalian Hearts. *PLoS One* **7,** e35299 (2012).
29. Kyle, J. R. & Ketcham, R. A. Application of high resolution X-ray computed tomography to mineral deposit origin, evaluation, and processing. *Ore Geol. Rev.* **65,** 821–839 (2015).
30. Dewanckele, J. *et al.* Neutron radiography and X-ray computed tomography for quantifying weathering and water uptake processes inside porous limestone used as building material. *Mater. Charact.* **88,** 86–99 (2014).
31. Li, P. *et al.* X-ray Microtomographic Characterisation of Porosity and its Influence on Fatigue Crack Growth. *Adv. Eng. Mater.* **8,** 476–479 (2006).
32. Lashkari, O., Yao, L., Cockcroft, S. & Maijer, D. X-Ray Microtomographic Characterization of Porosity in Aluminum Alloy A356. *Metall. Mater. Trans. A* **40,** 991–999 (2009).
33. Vanderesse, N., Maire, É., Chabod, A. & Buffière, J.-Y. Microtomographic study and finite element analysis of the porosity harmfulness in a cast aluminium alloy. *Int. J. Fatigue* **33,** 1514–1525 (2011).
34. Nicoletto, G., Konečná, R. & Fintova, S. Characterization of microshrinkage casting defects of Al–Si alloys by X-ray computed tomography and metallography. *Int. J. Fatigue* **41,** 39–46 (2012).
35. Tijani, Y., Heinrietz, A., Stets, W. & Voigt, P. Detection and Influence of Shrinkage Pores and Nonmetallic Inclusions on Fatigue Life of Cast Aluminum Alloys. *Metall. Mater. Trans. A* **44,** 5408–5415 (2013).
36. De Giovanni, M., Warnett, J. M., Williams, M. A. & Srirangam, P. 3D imaging and quantification of porosity and intermetallic particles in strontium modified Al-Si alloys. *J. Alloys Compd.* **727,** 353–361 (2017).
37. Sikandar, M., Khiyal, H., Khan, A. & Bibi, A. Modified Watershed Algorithm for Segmentation of 2D Images. **6,** (2009).
38. De Giovanni, M., Warnett, J. M., Williams, M. A., Haribabu, N. & Srirangam, P. X-ray tomography investigation of intensive sheared Al–SiC metal matrix composites. *Mater. Charact.* **110,** 258–263 (2015).
39. Denton, J. R. & Spittle, J. A. Solidification and susceptibility to hydrogen absorption of Al–Si alloys containing strontium. *Mater. Sci. Technol.* **1,** 305–311 (1985).

40. Fuoco, R., Correa, E. R. & Bastos, M. de A. Microporosity morphology in A356 aluminum alloy in unmodified and modified condition. *AFS Trans.* **109,** 659–677 (2001).

41. Chuang, C. *et al.* 3D quantitative analysis of graphite morphology in high strength cast iron by high-energy X-ray tomography. *Scr. Mater.* **106,** 5–8 (2015).

# Chapter 8:

# Conclusions and Further Work

## 8.1. Conclusions

In this thesis the potential of using rare earth elements, namely Y or Ce, as a substitute to or in combination with Sr as modification elements in Al-Si hypoeutectic alloys has been explored in terms of solidification behaviour and microstructure achieved. The effect of these elements on the porosity within the cast alloys has also been investigated. A comparison with unmodified Al-Si and Sr-modified Al-Si has been carried out throughout as a comparison to the current industrial practices while following the same casting procedures as those for the alloys containing Y or Ce. Below are the conclusions that can be drawn from this thesis and how these meet the initial objectives set out.

### 8.1.1. Objective 1: To provide an understanding of the modification of the eutectic Si in hypoeutectic Al-Si alloys by comparing the differences between full modification and partial modification, as obtained by Sr and partial modification or refinement as obtained by Ce and Y. The synergistic effect of combining Ce or Y with Sr will also be investigated.

This objective was addressed in chapters 3 – 5.

The addition of 1% rare earth metal (Ce or Y) to hypoeutectic Al-Si caused a partial modification. The solidification studies that were carried out to understand the influence of the rare earth addition showed that upon addition of the rare earth element the eutectic nucleation and growth temperatures are reduced to lower temperatures than Sr-modified Al-Si, whilst intermetallic phases similar to those formed in full modification were identified. Furthermore, it was noted that in the presence of Ce the solidification of the eutectic Al is completely independent from the primary Al. On the other hand, when only Y was added it was noted the eutectic and primary Al solidify together. The fact that Ce and Sr, a partial and a full modifier respectively, showed the same behaviour indicates that the solidification of the eutectic Al in relation to the primary Al is not a contributing factor to the modification of the Si eutectic phase.

It was also noted that complete modification was achieved upon adding a further 0.04% Sr to an alloy containing 1% rare earth additions. This indicates that the rare earth elements do not interfere with the modification mechanism as carried out by Sr.

Finally, the main finding in chapter 4 was that yttrium, which did not achieve full modification, segregated preferentially in the eutectic silicon phase. Literature has shown that Sr behaves similarly and achieves full modification. This finding shows that the segregation, at this scale, of the additional element does not define its modification potential. Rather the modification potential could be due to co-segregations within the eutectic Si, as observed in the literature.

### 8.1.2. Objective 2: To investigate whether rare earth additions such as Ce or Y have the potential to reduce the porosity within Sr-modified cast Al-Si alloys.

This objective was addressed in chapters 6 and 7.

In these chapters it was noted that the porosity within cast Al-Si alloys is significantly increased following modification by Sr. A smaller, but nonetheless significant increase, was observed following addition of rare earth metals. This finding indicates that rare earth elements could potentially be used to reduce porosity in Sr-modified Al-Si alloys. The earlier observation that these additions do not impair the modification potential of Sr is particularly significant in this context as well. The intermetallics formed in these alloys were also analysed.

## 8.2. Further Work

The work undertaken throughout this thesis lays down the foundation to further studies exploring the use of rare earth elements in combination with or as a substitute to Sr. Further research can be directed either towards more fundamental studies or more industrially relevant investigations.

A few examples were a more fundamental approach can be undertaken are:

- TEM studies looking at the twinning in these alloys to understand their growth and whether these can be explained by the IIT modification mechanism
- APT studies investigating any co-segregations of the rare-earth elements within the eutectic Si and how these effect the growth of eutectic Si.
- Research work applying EXAFS looking into the local coordination chemistry within the alloys.
- Preparing alloys by melt-spinning technique and analysis by DSC to understand the solidification of the intermetallics in relation to the eutectic Si.
- Computer simulations such as density functional theory (DFT) can be used to understand the theoretical interactions between Si, Al, Sr and the rare earth component.

In terms of more industrially relevant research the following could potentially be looked into:

- Repeating the same experiments but using larger castings and industrial alloys rather than high purity alloys. This would give information about the interaction of the rare earths with other intermetallics that are commonly found in such alloys.
- Using a sand casting technique as this is a typical industrial casting technique with slow cooling rates which accentuates the growth of the eutectic Si.
- The relatively high content of rare earth elements used and the intermetallics formed are expected to somewhat effect the fluidity of the molten alloy. A series of experiments to identify the minimum addition in order to retain the porosity reduction can be performed. In this respect casting simulation software can be used to predict the flow of the molten alloys in complex castings.
- It is also expected that the intermetallic particles will adversely affect the mechanical properties of the alloy. A definition of the mechanical properties would be required, such tensile and fatigue testing. Casting techniques, such as intensive shearing, can be applied when casting these alloys. This could

potentially result in the intermetallics forming a cast microstructure that could be considered similar to a metal matrix composite and thus improve the mechanical properties.

# Bibliography

Abdollahi, A. & Gruzleski, J. E. An evaluation of calcium as a eutectic modifier in A357 alloy. *Int. J. Cast Met. Res.* **11,** 145–155 (1998).

Atasoy, O. A., Yilmaz, F. & Elliott, R. Growth structures in aluminium-silicon alloys I. The coupled zone. *J. Cryst. Growth* **66,** 137–146 (1984).

Atwood, R. C., Sridhar, S. & Lee, P. D. Equations for nucleation of hydrogen gas pores during solidification of aluminium seven weight percent silicon alloy. *Scr. Mater.* **41,** 1255–1259 (1999).

Barrirero, J. *et al.* Cluster formation at the Si/liquid interface in Sr and Na modified Al–Si alloys. *Scr. Mater.* **117,** 16–19 (2016).

Barrirero, J. *et al.* Comparison of segregations formed in unmodified and Sr-modified Al–Si alloys studied by atom probe tomography and transmission electron microscopy. *J. Alloys Compd.* **611,** 410–421 (2014).

Bartley, R. *British and European Aluminium Casting Alloys*. (Association of Light Alloy Refiners, 1996).

Bell, J. A. E. & Winegard, W. C. Interconnexion of Silicon in Modified Aluminium-Silicon Eutectic. *Nature* **208,** 177 (1965).

Bian, X. F., Wang, W. M. & Qin, J. Y. Structures of Liquid Al-Si Alloy Modified by Sr. *Mater. Sci. Forum* **331–337,** 349–354 (2000).

Brosnan, M. & Shivkumar, S. Elevated Temperature Tensile Properties and Fracture Behavior of A356 Castings. *AFS Trans.* **103,** 727–737 (1995).

Byczynski, G. E. & Cusinato, D. A. The effects of strontium and grain refiner additions on the fatigue and tensile properties of industrial Al-Si-Cu-Mg alloy castings produced using the Ford Motor Company - Cosworth precision sand process. *Int. J. Cast Met. Res.* **15,** 315–324 (2002).

Campbell, J. & Tiryakioğlu, M. Review of effect of P and Sr on modification and porosity development in Al–Si alloys. *Mater. Sci. Technol.* **26,** 262–268 (2010).

Campbell, J. *Castings.* (Butterworth-Heinemann, 2003).

Chaijaruwanich, A., Lee, P. D., Dashwood, R. J., Youssef, Y. M. & Nagaumi, H. Evolution of pore morphology and distribution during the homogenization of direct chill cast Al-Mg alloys. *Acta Mater.* **55,** 285–293 (2007).

Cho, Y. H., Lee, H.-C., Oh, K. H. & Dahle, A. K. Effect of Strontium and

Phosphorus on Eutectic Al-Si Nucleation and Formation of β-Al5FeSi in Hypoeutectic Al-Si Foundry Alloys. *Metall. Mater. Trans. A* **39,** 2435–2448 (2008).

Chuang, C. *et al.* 3D quantitative analysis of graphite morphology in high strength cast iron by high-energy X-ray tomography. *Scr. Mater.* **106,** 5–8 (2015).

Clapham, L. & Smith, R. W. Segregation behaviour of strontium in modified and unmodified Al-Si alloys. *J. Cryst. Growth* **92,** 263–270 (1988).

Crosley, P. B. & Mondolfo, L. F. The modification of aluminum-silicon alloys. *Trans. Am. foundrymen's Soc.* **74,** 53–64 (1966).

Dahle, A. K. & Arnberg, L. Investigation of the dendrite coherency point in solidifying Al-Si foundry alloys. in *Proceedings 4th international conference on aluminum alloys* 91–98 (1994).

Dahle, A. K., Nogita, K., McDonald, S. D., Dinnis, C. & Lu, L. Eutectic modification and microstructure development in Al–Si Alloys. *Mater. Sci. Eng. A* **413–414,** 243–248 (2005).

Dahle, A. K., Nogita, K., McDonald, S. D., Zindel, J. W. & Hogan, L. M. Eutectic nucleation and growth in hypoeutectic Al-Si alloys at different strontium levels. *Metall. Mater. Trans. A* **32,** 949–960 (2001).

Davies, V. L. & West, J. M. Factors affecting the modification of Al-Si eutectic. *J. Inst. Met.* **92,** 175–180 (1964).

Davies, V. L. & West, J. M. Influence of small additions of sodium on the surface tension of Al and Al-Si alloys. *J. Inst. Met.* **92,** 208–210 (1964).

Davis, J. R. *ASM Speciality Handbook: Aluminum and Aluminum Alloys*. (ASM International, 1993).

Day, M. G. & Hellawell, A. The Microstructure and Crystallography of Aluminium-Silicon Eutectic Alloys. *Proc. R. Soc. London A Math. Phys. Eng. Sci.* **305,** 473–491 (1968).

Day, M. G. & Hellawell, A. The structure of modified aluminium-silicon eutectic alloy. *J. Inst. Met.* **95,** 377 (1967).

De Giovanni, M., Kaduk, J. A. & Srirangam, P. Modification of Al-Si Alloys by Ce or Ce with Sr. *JOM* 1–9 (2018). doi:10.1007/s11837-018-3192-6

De Giovanni, M., Warnett, J. M., Williams, M. A. & Srirangam, P. 3D imaging and quantification of porosity and intermetallic particles in strontium modified Al-Si alloys. *J. Alloys Compd.* **727,** 353–361 (2017).

De Giovanni, M., Warnett, J. M., Williams, M. A., Haribabu, N. & Srirangam, P. X-ray tomography investigation of intensive sheared Al–SiC metal matrix composites. *Mater. Charact.* **110,** 258–263 (2015).

De-Giovanni, M., Alam, T., Banerjee, R. & Srirangam, P. 3D Atom Probe Tomography Study on Segregation of Yttrium in Modified Al-Si Alloys. *JOM* **70,** 1765–1770 (2018).

Denton, J. R. & Spittle, J. A. Solidification and susceptibility to hydrogen absorption of Al–Si alloys containing strontium. *Mater. Sci. Technol.* **1,** 305–311 (1985).

Dewanckele, J. *et al.* Neutron radiography and X-ray computed tomography for quantifying weathering and water uptake processes inside porous limestone used as building material. *Mater. Charact.* **88,** 86–99 (2014).

Di Sabatino, M., Rørvik, S. & Prestmo, A. The influence of oxide inclusions on the fluidity of Al–7wt.%Si alloy. *Mater. Sci. Eng. A* **413,** 272–276 (2005).

Elliott, R. in *Eutectic Solidification Processing: Crystalline and Glassy Alloys* 157–231 (Butterworths, 1983).

Emadi, D., Gruzleski, J. E. & Toguri, J. M. The effect of Na and Sr modification on surface tension and volumetric shrinkage of A356 alloy and their influence on porosity formation. *Metall. Trans. B* **24,** 1055–1063 (1993).

Felberbaum, M., Landry-Désy, E., Weber, L. & Rappaz, M. Effective hydrogen diffusion coefficient for solidifying aluminium alloys. *Acta Mater.* **59,** 2302–2308 (2011).

Felfer, P. J., Alam, T., Ringer, S. P. & Cairney, J. M. A reproducible method for damage-free site-specific preparation of atom probe tips from interfaces. *Microsc. Res. Tech.* **75,** 484–491 (2012).

Flood, S. C. & Hunt, J. D. Modification of Al-Si eutectic alloys with Na. *Met. Sci.* **15,** 287–294 (1981).

Fuoco, R., Correa, E. R. & Bastos, M. de A. Effects of Grain Refinement on Feeding mechanisms in A356 Aluminum Alloy. *AFS Trans.* **106,** 401–409 (1998).

Fuoco, R., Correa, E. R. & Bastos, M. de A. Microporosity morphology in A356 aluminum alloy in unmodified and modified condition. *AFS Trans.* **109,** 659–677 (2001).

Fuoco, R., Correa, E. R. & Correa, A. V. O. Effect of modification treatment on microporosity formation in 356 Al alloy. *AFS Trans.* **103,** 379–387 (1995).

Fuoco, R., Correa, E. R. & Goldenstein, H. The effect of modification treatment on microporosity formation in 356 Al Alloy, part I: Interdendritic Feeding Evaluation.

*AFS Trans.* **104,** 1151–1158 (1996).

Gigliotti, M. F. X. & Colligan, G. A. The effects of sodium on the growth velocity and growth morphology of silicon in Al-Si alloys. *Metall. Trans.* **3,** 933–940 (1972).

Gröbner, J., Mirković, D. & Schmid-Fetzer, R. Thermodynamic aspects of the constitution, grain refining, and solidification enthalpies of Al-Ce-Si alloys. *Metall. Mater. Trans. A* **35,** 3349–3362 (2004).

Groteke, D. E. Influence of SNIF Treatment on Characteristics of Aluminium Foundry Alloys. *AFS Trans.* **93,** 953–960 (1985).

Guthy, H. V. Evolution of the Eutectic Microstructure in Chemically Modified and Unmodified Aluminum Silicon Alloys. (Worcester Polytechnic Institute, 2002).

Hamilton, D. . & Seidensticker, R. G. Propagation Mechanism of Germanium Dendrites. *J. Appl. Phys.* **31,** 1165–1168 (1960).

Hanna, M. D., Lu, S. & Hellawell, A. Modification in the aluminum silicon system. *Metall. Trans. A* **15,** 459–469 (1984).

Hatch, J. E. *Aluminium: Properties and Physical Metallurgy*. (American Society of Metals, 1984).

Heiberg, G. & Arnberg, L. Investigation of the microstructure of the Al–Si eutectic in binary aluminium–7 wt% silicon alloys by electron backscatter diffraction (EBSD). *J. Light Met.* **1,** 43–49 (2001).

Hetke, A. & Grundlach, R. B. Aluminum casting quality in alloy 356 engine components. *AFS Trans.* **102,** 367–380 (1994).

Ho, C. R. & Cantor, B. Modification of hypoeutectic Al-Si alloys. *J. Mater. Sci.* **30,** 1912–1920 (1995).

Hua, G., Ahmadi, H., Nouri, M. & Li, D. Positive effect of yttrium on the reduction of pores in cast Al alloy. *Mater. Chem. Phys.* **149–150,** 140–144 (2015).

Iwahori, H., Yonekura, K., Yamamoto, Y. & Nakamura, M. Occurring Behavior of Porosity and Feeding Capability of Sodium- and Strontium- Modified Al-Si Alloys. *AFS Trans.* **98,** 167–173 (1990).

Jacob, M. *et al.* État Actuel de l'Utilisation du Sodium, du Strontium et de l'Antimonie dans les Alliages Aluminium-Silicium Moulés. *Hommes et Fonderie* **258,** 45–54 (1995).

Jenkinson, D. C. & Hogan, L. M. The modification of aluminium-silicon alloys with strontium. *J. Cryst. Growth* **28,** 171–187 (1975).

Jordon, J. B. *et al.* Microstructural Inclusion Influence on Fatigue of a Cast A356

Aluminum Alloy. *Metall. Mater. Trans. A* **41,** 356–363 (2010).

Kim, C. B. & Heine, R. W. Fundamentals of modification in the aluminium-silicon system. *J. Inst. Met.* **92,** 367–376

Knuutinen, A., Nogita, K., McDonald, S. D. & Dahle, A. K. Modification of Al–Si alloys with Ba, Ca, Y and Yb. *J. Light Met.* **1,** 229–240 (2001).

Knuutinen, A., Nogita, K., McDonald, S. D. & Dahle, A. K. Porosity formation in aluminium alloy A356 modified with Ba, Ca, Y and Yb. *J. Light Met.* **1,** 241–249 (2001).

Kobayashi, K. F. & Hogan, L. M. The crystal growth of silicon in Al-Si alloys. *J. Mater. Sci.* **20,** 1961–1975 (1985).

Kyle, J. R. & Ketcham, R. A. Application of high resolution X-ray computed tomography to mineral deposit origin, evaluation, and processing. *Ore Geol. Rev.* **65,** 821–839 (2015).

Lashkari, O., Yao, L., Cockcroft, S. & Maijer, D. X-Ray Microtomographic Characterization of Porosity in Aluminum Alloy A356. *Metall. Mater. Trans. A* **40,** 991–999 (2009).

Lee, S.-L., Cheng, Y.-C., Chen, W.-C., Lee, C.-K. & Tan, A.-H. Effects of strontium and heat treatment on the wear-corrosion property of Al–7Si–0.3Mg alloy. *Mater. Chem. Phys.* **135,** 503–509 (2012).

Li, B., Wang, H., Jie, J. & Wei, Z. Effects of yttrium and heat treatment on the microstructure and tensile properties of Al–7.5Si–0.5Mg alloy. *Mater. Des.* **32,** 1617–1622 (2011).

Li, J. *et al.* The roles of Eu during the growth of eutectic Si in Al-Si alloys. *Sci. Rep.* **5,** 13802 (2015).

Li, J. H. & Schumacher, P. Effect of Y addition and cooling rate on refinement of eutectic Si in Al–5 wt-%Si alloys. *Int. J. Cast Met. Res.* **25,** 347–357 (2012).

Li, J. H. *et al.* Modification of eutectic Si in Al–Si alloys with Eu addition. *Acta Mater.* **84,** 153–163 (2015).

Li, J. H. *et al.* Nucleation and Growth of Eutectic Si in Al-Si Alloys with Na Addition. *Metall. Mater. Trans. A* **46,** 1300–1311 (2015).

Li, P. *et al.* X-ray Microtomographic Characterisation of Porosity and its Influence on Fatigue Crack Growth. *Adv. Eng. Mater.* **8,** 476–479 (2006).

Liao, C., Chen, J., Li, Y., Tu, R. & Pan, C. Morphologies of Al4Sr Intermetallic Phase and Its Modification Property upon A356 Alloys. *J. Mater. Sci. Technol.* **28,** 524–530 (2012).

Liao, H. C. *et al.* Effect of Sr addition on porosity formation in directionally solidified A356 alloy. *Int. J. Cast Met. Res.* **26,** 201–208 (2013).

Liu, L., Samuel, A. M., Samuel, F. H., Doty, H. W. & Valtierra, S. Influence of oxides on porosity formation in Sr-treated Al-Si casting alloys. *J. Mater. Sci.* **38,** 1255–1267 (2003).

Liu, L., Samuel, M., Samuel, F. H., Doty, H. W. & Valtierra, S. The role of Sr oxide on porosity. *AFS Trans.* **110,** 449–462 (2002).

Lu, S. & Hellawell, A. Growth mechanisms of silicon in Al-Si alloys. *J. Cryst. Growth* **73,** 316–328 (1985).

Lu, S.-Z. S. & Hellawell, A. The mechanism of silicon modification in aluminum-silicon alloys: Impurity induced twinning. *Metall. Trans. A* **18,** 1721–1733 (1987).

Mahmoud, M. G., Elgallad, E. M., Ibrahim, M. F. & Samuel, F. H. Effect of Rare Earth Metals on Porosity Formation in A356 Alloy. *Int. J. Met.* **12,** 251–265 (2018).

Makhlouf, M. M. & Guthy, H. V. The aluminum–silicon eutectic reaction: mechanisms and crystallography. *J. Light Met.* **1,** 199–218 (2001).

McLeod, A. J., Hogan, L. M., Adam, C. M. & Jenkinson, D. C. Growth mode of the aluminum phase in Al-Si and Al-Al3Fe eutectics. *J. Cryst. Growth* **19,** 301–309 (1973).

Miresmaeili, S. M., Campbell, J., Shabestari, S. G. & Boutorabi, S. M. A. Precipitation of Sr-rich intermetallic particles and their influence on pore formation in Sr-modified A356 alloy. *Metall. Mater. Trans. A* **36,** 2341–2349 (2005).

Mo, D.-F., He, G.-Q., Hu, Z.-F., Liu, X.-S. & Zhang, W.-H. Effect of microstructural features on fatigue behavior in A319-T6 aluminum alloy. *Mater. Sci. Eng. A* **527,** 3420–3426 (2010).

Mondolfo, L. F. Nucleation in eutectic alloys. *J. Aust. Inst. Met.* **10,** 169–177 (1965).

Murray, J. L. & McAlister, A. J. The Al-Si (Aluminum-Silicon) system. *Bull. Alloy Phase Diagrams* **5,** 74–84 (1984).

Nicoletto, G., Konečná, R. & Fintova, S. Characterization of microshrinkage casting defects of Al–Si alloys by X-ray computed tomography and metallography. *Int. J. Fatigue* **41,** 39–46 (2012).

Nogita, K. & Dahle, A. . Eutectic solidification in hypoeutectic Al–Si alloys: electron backscatter diffraction analysis. *Mater. Charact.* **46,** 305–310 (2001).

Nogita, K. *et al.* Determination of strontium segregation in modified hypoeutectic

Al–Si alloy by micro X-ray fluorescence analysis. *Scr. Mater.* **55,** 787–790 (2006).

Nogita, K., Knuutinen, A., McDonald, S. D. & Dahle, A. K. Mechanisms of eutectic solidification in Al–Si alloys modified with Ba, Ca, Y and Yb. *J. Light Met.* **1,** 219–228 (2001).

Nogita, K., McDonald, S. D. & Dahle, A. K. Eutectic Modification of Al-Si Alloys with Rare Earth Metals. *Mater. Trans.* **45,** 323–326 (2004).

Oxford Instruments. TruMap: Real time - real results. (2011).

Pacz, A. Alloy. (1921). at <http://www.google.com/patents/US1387900>

Polmear, I. J. in *Light Alloys* 205–235 (Elsevier, 2005). doi:10.1016/B978-075066371-7/50008-6

Qiu, H., Yan, H. & Hu, Z. Effect of samarium (Sm) addition on the microstructures and mechanical properties of Al–7Si–0.7Mg alloys. *J. Alloys Compd.* **567,** 77–81 (2013).

Samuel, A. M., Doty, H. W., Valtierra, S. & Samuel, F. H. Influence of Oxides on Porosity Formation in Sr-Treated Alloys. *Int. J. Met.* 1–14 (2016). doi:10.1007/s40962-016-0118-3

Sato, E., Kono, N., Sato, I. & Watanabe, H. Study on the phase diagram of Al-Si-Sr ternary alloy system. *J. Japan Inst. Light Met.* **35,** 71–78 (1985).

Schulz, E. Mikroskopische Untersuchungen bei der Veredelung von Silumin. *Zeitschrift für Met.* **39,** 123–125 (1949).

Shamsuzzoha, M. & Hogan, L. M. Crystal morphology of unmodified aluminium-silicon eutectic microstructures. *J. Cryst. Growth* **76,** 429–439 (1986).

Shamsuzzoha, M. & Hogan, L. M. The crystal morphology of fibrous silicon in strontium-modified Al-Si eutectic. *Philos. Mag. A* **54,** 459–477 (1986).

Shamsuzzoha, M. & Hogan, L. M. Twinning in fibrous eutectic silicon in modified Al-Si Alloys. *J. Cryst. Growth* **72,** 735–737 (1985).

Shi, Z. M., Wang, Q., Zhao, G. & Zhang, R. Y. Effects of erbium modification on the microstructure and mechanical properties of A356 aluminum alloys. *Mater. Sci. Eng. A* **626,** 102–107 (2015).

Shi, Z., Wang, Q., Shi, Y., Zhao, G. & Zhang, R. Microstructure and mechanical properties of Gd-modified A356 aluminum alloys. *J. Rare Earths* **33,** 1004–1009 (2015).

Sigworth, G. K. The Modification of Al-Si Casting Alloys: Important Practical and Theoretical Aspects. *Int. J. Met.* **2,** 19–40 (2008).

Sikandar, M., Khiyal, H., Khan, A. & Bibi, A. Modified Watershed Algorithm for Segmentation of 2D Images. **6,** (2009).

Srirangam, P. *et al.* Probing the local atomic structure of Sr-modified Al–Si alloys. *Acta Mater.* **65,** 185–193 (2014).

Srirangam, V. S. P. *et al.* XAFS studies on a modified Al-Si hypoeutectic alloy. *J. Phys. Conf. Ser.* **190,** 012068 (2009).

Steen, H. A. . & Hellawell, A. The growth of eutectic silicon—contributions to undercooling. *Acta Metall.* **23,** 529–535 (1975).

Stephenson, R. S. *et al.* Contrast Enhanced Micro-Computed Tomography Resolves the 3-Dimensional Morphology of the Cardiac Conduction System in Mammalian Hearts. *PLoS One* **7,** e35299 (2012).

Sundquist, B. E., Bruscato, R. & Mondolfo, L. F. The surface energy of solid metals. *J. Inst. Met.* **91,** 204–208 (1963).

Ferreira, T. & Rasband, W. *ImageJ User Guide IJ 1.46r*. *IJ 1.46r* (2012). doi:10.1038/nmeth.2019

Terzi, S. *et al.* In situ study of nucleation and growth of the irregular α-Al/β-Al5FeSi eutectic by 3-D synchrotron X-ray microtomography. *Acta Mater.* **58,** 5370–5380 (2010).

Thall, B. M. & Chalmers, B. Modification in aluminum-silicon alloys. *J. Inst. Met.* **78,** 79 (1949).

Tijani, Y., Heinrietz, A., Stets, W. & Voigt, P. Detection and Influence of Shrinkage Pores and Nonmetallic Inclusions on Fatigue Life of Cast Aluminum Alloys. *Metall. Mater. Trans. A* **44,** 5408–5415 (2013).

Timpel, M. *et al.* Sr–Al–Si co-segregated regions in eutectic Si phase of Sr-modified Al–10Si alloy. *Ultramicroscopy* **132,** 216–221 (2013).

Timpel, M. *et al.* The role of strontium in modifying aluminium–silicon alloys. *Acta Mater.* **60,** 3920–3928 (2012).

Tsai, Y. C. *et al.* Effect of trace La addition on the microstructures and mechanical properties of A356 (Al–7Si–0.35Mg) aluminum alloys. *J. Alloys Compd.* **487,** 157–162 (2009).

Tsai, Y. C., Lee, S. L. & Lin, C. K. Effect of trace Ce addition on the microstructures and mechanical properties of A356 (Al–7SI–0.35 Mg) aluminum alloys. *J. Chinese Inst. Eng.* **34,** 609–616 (2011).

Tsumura, Y. On the Theory of Modification of Aluminium-Silicon Alloys. *J. Japan*

*Inst. Met.* **21,** 69–83 (1957).

Ulbin, M. *et al.* Internal structure characterization of AlSi7 and AlSi10 advanced pore morphology (APM) foam elements. *Mater. Lett.* **136,** 416–419 (2014).

Vanderesse, N., Maire, É., Chabod, A. & Buffière, J.-Y. Microtomographic study and finite element analysis of the porosity harmfulness in a cast aluminium alloy. *Int. J. Fatigue* **33,** 1514–1525 (2011).

Vijeesh, V. & Prabhu, K. N. in *Light Metals 2015* 403–407 (John Wiley & Sons, Inc., 2015). doi:10.1002/9781119093435.ch67

Wang, Q. G., Apelian, D. & Lados, D. A. Fatigue behavior of A356-T6 aluminum cast alloys. Part I. Effect of casting defects. *J. Light Met.* **1,** 73–84 (2001).

Xiufang, B., Weimin, W. & Jingyu, Q. Liquid structure of Al–12.5% Si alloy modified by antimony. *Mater. Charact.* **46,** 25–29 (2001).

Ye, B. J. An assessment of the role of rare earth in the eutectic modification of cast Al-Si. *Trans. Am. Foundrymen's Soc.* **93,** 533–544 (1985).

Yi, J. Z., Gao, Y. X., Lee, P. D., Flower, H. M. & Lindley, T. C. Scatter in fatigue life due to effects of porosity in cast A356-T6 aluminum-silicon alloys. *Metall. Mater. Trans. A* **34,** 1879–1890 (2003).

Yi, J. Z., Lee, P. D., Lindley, T. C. & Fukui, T. Statistical modeling of microstructure and defect population effects on the fatigue performance of cast A356-T6 automotive components. *Mater. Sci. Eng. A* **432,** 59–68 (2006).

Zaldívar-Cadena, A. A. & Flores-Valdés, A. Prediction and identification of calcium-rich phases in Al–Si alloys by electron backscatter diffraction EBSD/SEM. *Mater. Charact.* **58,** 834–841 (2007).

Zarif, M., Mckay, B. & Schumacher, P. Study of Heterogeneous Nucleation of Eutectic Si in High-Purity Al-Si Alloys with Sr Addition. *Metall. Mater. Trans. A* **42,** 1684–1691 (2010).